Forschungszentrum Karlsruhe
in der Helmholtz-Gemeinschaft

Wissenschaftliche Berichte
FZKA 7201

Three-Dimensional MHD Flow in Sudden Expansions

C. Mistrangelo

Institut für Kern- und Energietechnik
Programm Kernfusion

März 2006

Forschungszentrum Karlsruhe

in der Helmholtz-Gemeinschaft

Wissenschaftliche Berichte

FZKA 7201

Three-Dimensional MHD Flow in Sudden Expansions

C. Mistrangelo

Institut für Kern- und Energietechnik
Programm Kernfusion

Von der Fakultät für Maschinenbau der Universität Karlsruhe (TH)
genehmigte Dissertation

Forschungszentrum Karlsruhe GmbH, Karlsruhe
2006

Forschungszentrum Karlsruhe GmbH
Postfach 3640, 76021 Karlsruhe

Mitglied der Hermann von Helmholtz-Gemeinschaft
Deutscher Forschungszentren (HGF)

ISSN 0947-8620

urn:nbn:de:0005-072011

THREE-DIMENSIONAL MHD FLOW IN SUDDEN EXPANSIONS

Abstract

Magnetohydrodynamic (MHD) phenomena caused by the interaction of electrically conducting fluids with a magnetic field are exploited in many metallurgical processes to control and manipulate metals. The knowledge of MHD effects is also a key issue for the development of fusion reactors where a plasma is confined by a strong magnetic field and liquid metals are used to produce tritium that fuels the reactor.

A numerical tool, based on an extension of the commercial code CFX, has been developed to study MHD flows in arbitrary geometries and for any orientation of the imposed magnetic field. As an example of application a detailed analysis of the MHD flow in sudden expansions has been performed, focusing on the effects of the magnetic field and inertia forces on flow and current distribution and on pressure drops caused by induced three dimensional electric currents.

The results show that by increasing the applied magnetic field the recirculations that form behind the expansion reduce in size and the spiralling motion is progressively damped out. For sufficiently high magnetic fields the vortices are suppressed but a reverse flow is still observed close to the corners of the duct, near the side walls.

Complex current paths have been found and special emphasis has been placed on the analysis of the evolution of 3D current loops that form in the core region of the duct.

A parametric study has been performed for a constant applied magnetic field varying the relative strength of inertia effects compared to that of electromagnetic forces. When Lorentz forces are much larger than inertia forces, no vortices occur. By increasing inertial effects, vortical structures form behind the cross-section enlargement. The results show that both the pressure drop and the size of the recirculations are strongly affected by inertia forces.

The numerical results have been compared with experimental data for surface potential and pressure distribution. A very good agreement has been found, confirming the reliability of this computational approach.

DREIDIMENSIONALE MHD STRÖMUNGEN IN PLÖTZLICHEN EXPANSIONEN

Zusammenfassung

Magnetohydrodynamische (MHD) Effekte, hervorgerufen durch die Wechselwirkung elektrisch leitender Flüssigkeiten mit einem Magnetfeld, werden in vielen metallurgischen Prozessen benutzt, um Metallschmelzen zu kontrollieren und zu beeinflussen. Ein weiteres Feld für MHD Anwendungen ist die Energieerzeugung in Fusionsreaktoren, in denen ein Plasma durch ein starkes Magnetfeld eingeschlossen wird und Flüssigmetalle als Brutmaterial verwendet werden.

Durch die Erweiterung des Programmpakets CFX wurde ein numerisches Werkzeug entwickelt, mit dem MHD-Strömungen in beliebigen Geometrien und für jede Orientierung eines vorgegebenen Magnetfelds untersucht werden können. Als Anwendungsbeispiel wurde eine ausführliche Analyse der MHD-Strömung in einer plötzlichen Expansion durchgeführt. Im Mittelpunkt dieser Analyse standen die Einflüsse des Magnetfelds und der Trägheitskräfte auf die Strömung und auf die zusätzlichen Druckverluste, die von dreidimensionalen elektrischen Strömen im Magnetfeld verursacht werden.

Die Ergebnisse zeigen, dass mit zunehmendem Magnetfeld die Rückströmgebiete hinter der Querschnittserweiterung kleiner werden und die Wirbelströmung nach und nach abgedämpft wird. Bei einem ausreichend starken Magnetfeld verschwinden die Wirbel vollständig. Eine Rückströmung im Bereich der Ecken des Kanals, in der Nähe der magnetfeldparallelen Seitenwände bleibt jedoch erhalten.

In einer Parameterstudie wurde die MHD Strömung in einem homogenen Magnetfeld untersucht, bei der die relative Stärke der Trägheitskräfte gegenüber der Stärke der elektromagnetischen Kräfte geändert wurde. Falls die Lorentz-Kräfte wesentlich größer sind als die Trägheitskräfte, werden Wirbelströmungen unterdrückt. Mit zunehmenden Trägheitskräften bilden sich Wirbel hinter der Querschnittserweiterung. Nahe der Expansion findet man komplizierte dreidimensionale Strompfade, die sich im Kernbereich des Kanals ausbilden. Die Ergebnisse zeigen, dass sowohl der Druckverlust als auch das Ausmaß der Rückströmung, sowie die dreidimensionalen Strompfade durch die Trägheitskräfte beeinflusst werden.

Das elektrische Potenzial auf der Kanaloberfläche und die Druckverteilung, die als experimentelle Daten vorliegen, wurden mit den numerischen Ergebnissen verglichen. Die sehr gute Übereinstimmung der experimentellen Ergebnisse mit den Rechnungen bestätigt die Zuverlässigkeit des entwickelten Rechenprogramms.

Contents

Dimensional variables

Description	*Symbol*	*Dimensions*
Characteristic length (half channel width)	L	$[m]$
Characteristic velocity (average velocity)	v_0	$[ms^{-1}]$
Density of the fluid	ρ	$[kgm^{-3}]$
Electrical conductivity of the fluid	σ	$[\Omega^{-1}m^{-1}]$
Electrical conductivity of the wall	σ_w	$[\Omega^{-1}m^{-1}]$
Electric field	$\mathbf{E}$	$[Vm^{-1}]$
Kinematic viscosity	ν	$[m^2s^{-1}]$
Magnetic permeability	μ	$[NA^{-2}]$
Magnitude of the applied magnetic field	B_0	$[T]$
Source term of momentum equation	S_m	$[kgm^{-2}s^{-2}]$
Source term of energy equation	S_T	$[Wm^{-3}]$
Specific heat capacity	c_p	$[Jkg^{-1}K^{-1}]$
Temperature	T	$[K]$

Description	*Symbol*	*Dimensions*
Thermal conductivity of the fluid	λ	$[Wm^{-1}K^{-1}]$
Thermal conductivity of the wall	λ_w	$[Wm^{-1}K^{-1}]$
Thickness of duct walls	t_w	$[m]$
Time	t	$[s]$

Dimensionless variables

Description	*Symbol*
Axial coordinate	x
Vertical coordinate	y
Transverse coordinate	z
Electric potential in the fluid	ϕ
Electric potential in the wall	ϕ_w
Pressure in hydrodynamic scale	p
Pressure in MHD scale	$P = p/N$
Thickness of Hartmann layer	δ_{Ha}
Thickness of side layer	δ_{side}

Dimensionless vectors

Description	*Symbol* (bold)
Unit vectors	$\mathbf{x}$, $\mathbf{y}$, $\mathbf{z}$
Current density in the fluid	$\mathbf{j} = (j_x, j_y, j_z)$
Current density in the wall	$\mathbf{j}_w = (j_{wx}, j_{wy}, j_{wz})$
Lorentz force	$\mathbf{L} = (L_x, L_y, L_z)$
Magnetic field	$\mathbf{B} = (B_x, B_y, B_z)$
Velocity	$\mathbf{v} = (u, v, w)$

Dimensionless parameters

Description	*Symbol*
Conductance parameter	$c = \dfrac{\sigma_w t_w}{\sigma L}$
Hartmann number	$Ha = LB_0\sqrt{\dfrac{\sigma}{\rho\nu}}$
Interaction parameter	$N = \dfrac{\sigma L B_0^2}{\rho v_0}$
Magnetic Reynolds number	$R_m = \mu\sigma L v_0$
Reynolds number	$Re = \dfrac{v_0 L}{\nu}$

1 Introduction

The interaction of moving electrically conducting fluids with a magnetic field gives rise to a rich variety of magnetohydrodynamic (MHD) phenomena.

These effects are exploited both in technical devices, such as pumps and flowmeters, and in industrial processes to control and manipulate various materials (Davidson (1999)). Application of electromagnetic forces to material processing has been recognized as a promising technology and it is based on the fact that magnetic fields can influence the flow of electrically conducting fluids in different ways.

For example the application of a static magnetic field can damp down fluid motion and suppress unwanted turbulent fluctuations. This is due to the presence of induced currents that leads to Joule dissipation and the consequent conversion of kinetic energy into heat. This is used, for instance, in the continuous casting of large steel slabs to suppress the motion of the submerged jet that feeds the mould.

In order to homogenize the liquid part of partially solidified ingots to obtain products of high homogeneity and purity, rotating magnetic fields are employed. They can generate a swirling motion used to stir the melts.

Moreover, high frequency magnetic fields can repel adjacent conductors providing a method to treat metallic samples without contact to any wall. This phenomenon is known as electromagnetic levitation.

Electromagnetic processing of materials includes also stabilization of melts and free surfaces, laser welding and surface treatment, production of very fine powders, semiconductors, high performance superalloys and aluminum.

Concerning MHD devices, electromagnetic flowmeters are often used since they can work also with corrosive liquids and slurries. They measure the voltage induced by the motion of the conductor through the magnetic field. The potential produced is proportional to the flow rate of the fluid flowing in the duct. In chemical and metallurgical industry, MHD pumps are employed. They offer the advantage that they can be utilized even with aggressive, chemical reactive and very hot fluids. In addition, they do not have moving mechanical parts and this increases their reliability.

This brief description of some industrial processes and technical systems where MHD effects are utilized, shows that the magnetic field represents a versatile and non-intrusive mean to control and influence the flow of liquid metals. Therefore, it can be employed to develop new production methods and to improve existing processes to obtain for instance high quality materials.

The increasing interest in the study of MHD phenomena is also related to the development of fusion reactors where a plasma is confined by a strong magnetic field (Hunt and Holroyd (1977)). MHD effects are important in the so called blanket (Morley, Malang and Kirillov (2005)). This component is located between the plasma and the magnetic field coils (Fig.1). The blanket absorbs neutrons transforming their energy into heat, which is then carried away by a suitable coolant and it prevents neutrons from reaching the magnets avoiding in this way radiation damages. In addition it is responsible for the breeding of tritium necessary to fuel the reactor. In order to accomplish this task, the blanket should contain at least some fraction of Lithium. Liquid metal alloys, such as the eutectic PbLi, are attractive breeder materials due to their high tritium breeding

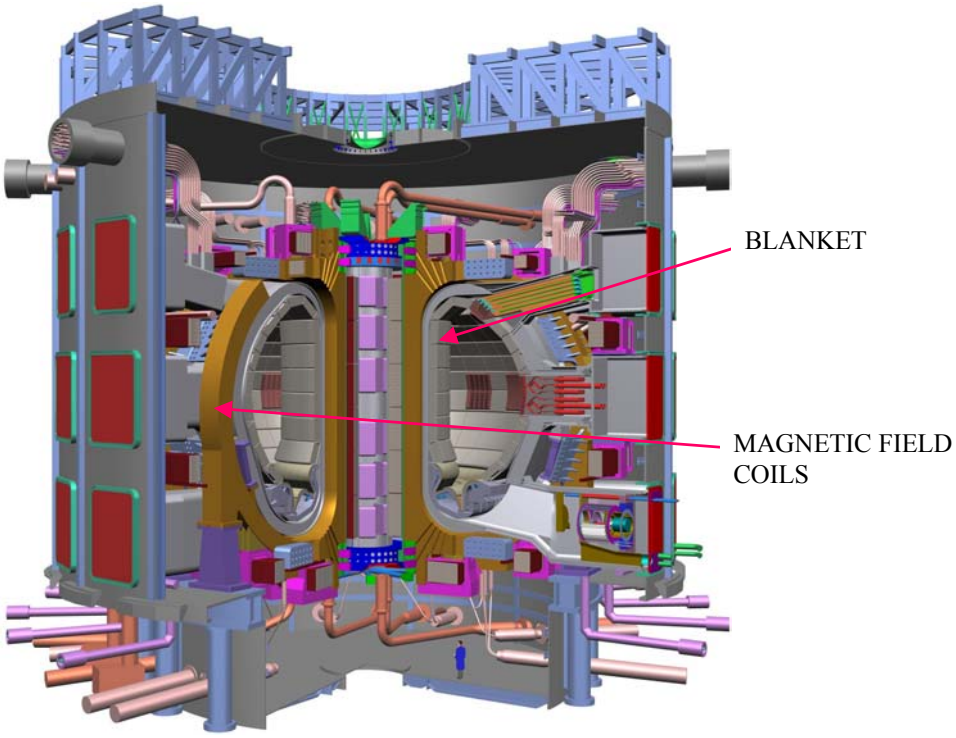

Figure 1: General view of the proposed international experimental fusion reactor (ITER).

capability and their large thermal conductivity. In some design concepts for the blankets, liquid metals are used only as breeder material and helium or water are considered as possible coolants. There are other concepts in which the liquid metal serves both as breeder material and as coolant. Important issues involved in the design of the so called self-cooled blanket are the high pressure drop caused by MHD interactions when the fluid has to flow at high velocity and the effects of flow redistribution on heat transport.

The electrically conducting fluid is distributed into the breeding zone through a piping system and manifolds, with smaller size compared with the large breeder units. As a consequence the liquid metal has to flow through expansions and contractions. Moreover, the liquid metal is circulated towards external facilities both to remove tritium and for the purification of the liquid metal itself. Therefore, the liquid metal moves in the strong magnetic field that confines the fusion plasma giving rise to MHD effects.

1.1 Motivations and problem specification

In order to ensure a successful and effective use of electromagnetic phenomena in industrial processes and technical systems, a very good understanding of the effects of the application of a magnetic field on the flow of electrically conducting fluids in channels and various geometric elements is required. Of special interest is the MHD flow in sudden expansions since these geometries are basic components of liquid metal devices and circuits as well as of fusion reactor blankets. The MHD phenomena that can

occur in ducts with sudden cross-section enlargements may strongly influence the distribution of the flow and affect for instance the thermal performance of the component under study. Moreover, large MHD pressure drops may occur that increase the power required to pump the liquid metal through channels and they can also give rise to strong mechanical stresses.

Flows in expansions can lead to the formation of stagnation zones and regions of reverse flow. In the case of fusion reactor blankets these stagnant and back flow areas can result in the appearance of hot spots or in the accumulation of tritium.

Numerical and experimental data are therefore needed to predict pressure drop, electric current distribution and flow structures that characterize MHD flows in such geometries. Accurate laboratory experiments are sometimes difficult and too expensive to perform and moreover, technical limitations can restrict the experiments to a defined range of parameters. Thus, numerical simulations are a very important tool for studying MHD flows and supplement the experimental results. A combination of experimental data, calculations and analytical solutions allows to cover a wide range of the parameters that describe the operating conditions of engineering systems.

The purpose of the present work is to develop a numerical tool that is able to simulate MHD flows in arbitrary geometries and for any orientation of the applied magnetic field. The equations describing MHD flows are implemented in the commercial code CFX. This latter is a flexible computational fluid dynamics code (CFD) based on the finite volume approach. It does not model MHD equations but it allows to modify the fundamental hydrodynamic equations by means of Fortran subroutines. Therefore CFX can be extended to model MHD phenomena by introducing the electromagnetic forces as a source term in the momentum equation and by solving an equation that describes the evolution of the electric potential.

As an example of possible applications, a detailed investigation of MHD flows in symmetric sudden expansions of rectangular ducts is carried out to analyze the effects of the magnetic field and inertia forces on flow and current distribution, and on the pressure drop. Emphasis is placed on the suppression of vortical structures and the modification of the size of the region where reverse flow occurs.

The electrically conducting fluid flows preferentially in the x direction and the externally applied magnetic field is uniform and aligned with the y axis, $\mathbf{B} = B_0\mathbf{y}$ (Fig.2). The geometry is chosen according to the features of the experimental test section used in the MEKKA laboratory of the Forschungszentrum Karlsruhe. The expansion ratio is equal to 4 and the wall conductance parameter c, which describes the ratio of the electrical conductance of the wall to the fluid material is 0.1.

This numerical approach is validated through the comparison of the results with the available analytical solution and with the experimental data. Moreover, the results of the study of the magnetic effects obtained for very small inertia forces confirm the outcomes of the asymptotic theory. Thus, this modified code can be regarded also as a starting point for further developments and for application to more complex geometries related for example to the blanket concepts that are under development.

In the following sections a short review of the basic equations describing the MHD flows and the used assumptions is given. A discussion of the main MHD phenomena is

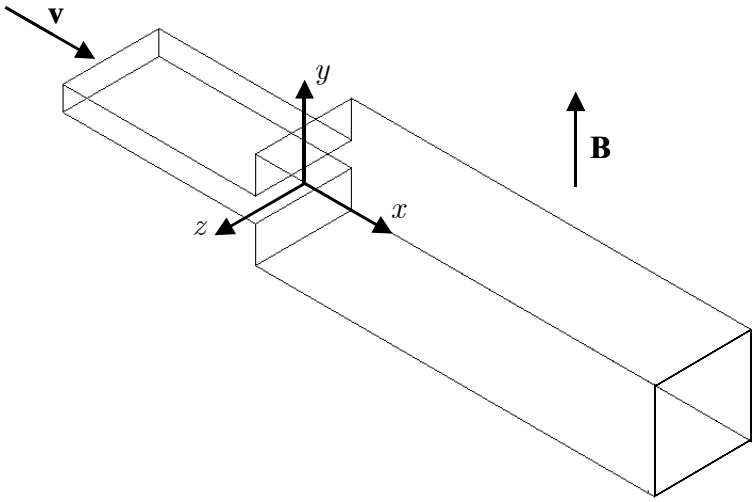

Figure 2: Sketch of the geometry used for the present study. The expansion ratio is 4.

included as well.

In Chapter 4.3 the main results of the analysis of the flow in sudden expansions are discussed. First the 3D hydrodynamic flow is investigated since no results have been found in the literature. This study is needed to understand how the magnetic field acts on the flow distribution and in particular on the dimension and the occurrence of separation regions that form behind the cross-section enlargement. Then the flow of electrically conducting fluids under a uniform magnetic field is analyzed. The study of magnetic effects is supplemented by a parametric study in which the magnetic field is kept constant and inertia forces are progressive reduced compared with Lorentz forces. Possibilities for further development and applications of the code are outlined.

1.2 State of art

1.2.1 Magnetohydrodynamic flow

A vast literature is available regarding the study of MHD flows. The early works concern fully developed, laminar MHD flows in ducts under a uniform magnetic field. This flow is characterized by the fact that all physical quantities, except the pressure, do not vary along the flow direction and the pressure gradient in the direction of motion is constant.

For two-dimensional MHD channel flows there are two classes of analytical solutions. The first comprises the exact solution, which may be represented by Fourier series and the second one may be obtained as an asymptotic approximation for large Hartmann numbers, Ha. This latter one is a characteristic dimensionless group whose square gives a measure for the ratio of electromagnetic to viscous forces.

Exact solutions have been developed by Hartmann (1937) for a one dimensional problem consisting of rectilinear, laminar MHD flow between two infinite parallel plates. The imposed magnetic field is uniform and normal to the two surfaces. For sufficiently high Hartmann numbers the flow is characterized by a core with uniform velocity and thin boundary layers along the plates. These layers are called Hartmann layers and they are present along walls on which the magnetic field has a normal component.

Shercliff (1953) found an exact solution for 2D MHD flows in ducts with insulating walls and pointed out the existence of a second type of boundary layers near walls parallel to the magnetic field, known as side or parallel layers. Chang and Lundgren (1961) and Uflyand (1961) obtained exact solutions for MHD flows in channels with perfectly conducting walls. Hunt (1965) analyzed the case of MHD flows in ducts with perfectly conducting Hartmann walls and thin conducting sides and the case with Hartmann walls of arbitrary conductivity and insulating lateral walls. He examined also the solution for large Hartmann numbers and found that a variation in the conductivity of the side walls has a strong effect on the velocity profile in the parallel boundary layers and on the volume flux carried by these layers. Hunt and Stewartson (1965) studied the MHD flow in rectangular channels with perfectly conducting side walls and insulating Hartmann walls for high Hartmann numbers using a boundary layer technique. In their work a description of the main flow regions can be found, consisting in a core associated with Hartmann layers along walls perpendicular to the magnetic field whose thickness scales as Ha^{-1} and thicker boundary layers on walls parallel to the field ($\delta_{side} = O(Ha^{-1/2})$). They also found that the current distribution in the corners of the duct affects the flow in the boundary layers. Approximate solutions for rectangular ducts with non-conducting walls have been developed by Shercliff (1953). He obtained a first approximation for the volumetric flow rate through the channel that was extended to the case of symmetric ducts with thin walls of arbitrary conductivity by Chang and Lundgren (1961). Temperley and Todd (1971) treated the fully developed MHD flow in ducts with thin conducting walls characterized by a conductance ratio c of the order of one, where c represents the ratio between the electrical conductance of the wall and fluid material. They applied a general expansion procedure valid for high Hartmann numbers. The MHD fully developed flow in channels with a small conductance ratio ($c < 0.1$) was investigated by Walker (1981) by means of asymptotic expansions. He analyzed various combinations of the conductivity of side walls and parallel layers, under

the assumption that Hartmann walls are better conducting than the adjacent boundary layers ($Ha^{-1} \ll c \ll 1$).

Another type of layers was identified by Ludford (1960) who investigated the MHD flow around obstacles in channels. It was observed that for high Hartmann numbers thin internal layers develop along magnetic field lines, tangent to the obstacle. Hunt and Leibovich (1967) analyzed the 2D flow over a body placed in a duct with diverging walls. They found that the structure of the internal layers depends on the relative size of the Hartmann number, Ha, and the interaction parameter, N. This latter one is a non-dimensional parameter, which describes the relative importance of electromagnetic forces compared to inertia. Depending on the combination of these two dimensionless groups, layers of different thickness occur. If $N \ll Ha^{3/2}$ their thickness is of the order of $N^{-1/3}$ and it corresponds to the case in which a balance between electromagnetic and inertia forces is established. If $N \gg Ha^{3/2}$ the thickness of the layers is proportional to $Ha^{-1/2}$ and electromagnetic and viscous forces balance each other. For finding the equations governing Ludford layers, the two authors studied the MHD flow in a single sided diverging duct.

Internal layers may occur also when a rectangular duct is turned by an angle in such a way that the magnetic filed is not parallel to a pair of walls any more. The shear layers spread from the corners into the fluid along magnetic field lines. Alty (1971) analyzed this kind of flow considering channels with one pair of walls insulating and the other perfectly conducting.

The shear layers described above may originate both from geometrical and electrical discontinuities. They occur for instance in 3D bends, in geometries with varying cross-section or with changes in wall conductivity or contact resistance along the flow path.

Two different approaches have been used to study general 3D MHD flows. One is the direct numerical simulation accounting for all the physical effects and the other one is the asymptotic method that focuses on the main phenomena and is valid for high Hartmann numbers and interaction parameters. The latter one has been proposed for application to 3D flows by Kulikovskii (1968). With this approach the flow region can be divided in a core where a balance between pressure and Lorentz forces is established, and thin viscous layers in which electromagnetic and viscous forces are dominant. By integrating the obtained simplified equations along magnetic field lines, the problem is reduced to a set of coupled 2D equations for pressure and electric potential at the fluid wall interface. From these variables the complete solution can be reconstructed.

The development of fusion reactors has led to a growing interest in the study of 3D MHD phenomena associated with the presence of these internal layers. Many of the works described in the following treat the MHD flow in geometries that are closely related to applications in fusion technology.

Stieglitz, Barleon, Bühler and Molokov (1996) investigated experimentally the flow in right-angle bends, which turn the flow from a direction perpendicular to the magnetic field into a direction parallel to the field. Here internal layers aligned with the magnetic field originate from the sharp corner. The pressure drop along the bend has been found theoretically by Molokov and Bühler (1994) by means of an asymptotic model. More significant are MHD flows in bends turned by an angle to form a forward or backward elbow. In the latter case three core regions are identified separated by internal layers

(Moon, Hua and Walker (1991)). These configurations create the highest pressure drop.

Weaker effects occur instead in the case of flows in bends in a plane perpendicular to the magnetic field.

Walker (1986b) studied the flow in a elbow in a plane normal to the magnetic field and found that the increase in pressure drop due to 3D effects was not significant. The same conclusion was reached by Bühler (1995) who employed an asymptotic model for studying the flow in U-bends of rectangular cross-section.

Molokov (1994) investigated MHD flows in ducts with a cross-section enlargement in the plane perpendicular to the imposed field, concluding that any changes of the geometry in this plane do not cause considerable 3D effects and the pressure drop is comparable to that in a duct in which the flow is locally fully developed.

The previous observations justify the investigations in the present analysis of 3D MHD flows in channels, which enlarge along the direction of the magnetic field.

Expansions and contractions are important geometric elements in liquid metal devices and the study of the flow in such geometries is a key issue for applications in fusion reactor blankets where the flow is distributed from small pipes to large boxes.

Walker, Ludford and Hunt (1972) analyzed MHD flows in smoothly expanding insulating channels using an inertialess approximation and Walker (1981), by using the same assumptions, namely high Hartmann number and interaction parameter, considered the case of ducts with thin conducting walls. This problem has been studied later by Bühler (2003) by asymptotic techniques. He considered MHD flows in a duct formed by two different channels of uniform cross-section connected by a smooth expansion. He performed a parametric study reducing progressively the length of the expansion. This analysis shows that, approaching the geometry of a sudden expansion, namely for an infinitesimally small expansion length, the pressure drop increases. In this limiting situation viscous internal layers become important and stronger 3D phenomena occur. Therefore ducts with a sudden enlargement give rise to the largest MHD interaction and for that reason this geometry has been selected for the study reported in this thesis.

All the previous investigations are based on the assumptions of strong applied magnetic fields ($Ha \gg 1$) and negligible inertial effects ($N \gg 1$). The study of a wider range of parameters, which allows for example the investigation of the effects of inertia forces, can be performed only by a fully numerical approach. Difficulties are related to the presence of shear layers in which inertia and friction may be dominant and whose thickness reduces by increasing the Hartmann number. For obtaining an accurate solution these thin layers must be properly resolved, which leads to problems of memory storage, execution time and convergence rate. For these reasons only few researchers performed 3D calculations and usually they restricted themselves to small Hartmann numbers. As an example we can cite the numerical analysis of 3D MHD flow in a single-sided sudden expansion with insulating walls performed by Aitov, Kalyutik and Tananaev (1983). Results are presented for Hartmann number equal to ten. A fully numerical approach has been used by Sterl (1990) who investigated flows in rectangular ducts with thin conducting walls exposed to a non uniform magnetic field. Hartmann numbers up to one hundred are reached for the 3D calculations. Numerical solutions are presented by Myasnikov and Kalyutik (1997) for flows in 3D sudden expansions either with insulating or perfectly conducting walls for Hartmann numbers lower than forty.

Kumamaru, Kodama, Hirano and Itoh (2004) performed 3D simulations for liquid metal flows through a rectangular duct with insulating walls in the inlet region of an imposed magnetic field for Hartmann number equal to one hundred.

This short overview of the available numerical analyses shows that, in order to get a complete understanding of 3D MHD phenomena, it is necessary to study further on flows in the range of high Hartmann numbers and moderate and small interaction parameters.

To conclude this literature review, it is worth stressing the importance of experiments as a necessary complement for the investigation of the physical phenomena involved in the process under study.

Experimental results for the flow in channels with a sudden enlargement of the cross-section are described by Branover, Vasil'ev and Gel'fgat (1967) who focused on the pressure distribution along the duct and by Gel'fgat and Kit (1971) who investigated the potential gradient distribution near sudden expansions and contractions. Picologlou, Reed, Hua, Barleon, Kreuzinger and Walker (1989) studied experimentally the flow in a geometry where smooth expansions and contractions are located periodically along the axis of the duct. As a further reference, the experimental studies performed by Evtushenko, Sidorenkov and Shishko (1992) can be considered, where the MHD flows in slotted channels and sudden expansions are analyzed.

Closely related to the present work are the experiments on MHD flows in a rectangular channel with sudden expansion conducted in the MEKKA laboratory of the Forschungszentrum Karlsruhe (Horanyi, Bühler and Arbogast (2005)). These experimental data are used to validate the numerical approach and to test the reliability of the computed results for high Hartmann numbers (Section 4.4).

1.2.2 Hydrodynamic flow

In this section a brief survey of work related to the hydrodynamic flow in sudden expansions is given, focusing on the main flow features and on fundamental issues concerning the stability of flow configurations. The phenomena of flow separation and reattachment caused by sudden changes in the cross-section of the duct have received significant attention because of their importance in many engineering applications. A short literature review is presented also for the flow over backward-facing steps reporting works that describe flow structures similar to the ones occurring in sudden expansions.

Rectangular sudden expansion

Two-dimensional incompressible flow in a symmetric sudden expansion has been the subject of several numerical and experimental investigations. According to experimental studies (Durst, Mellin and H.Whitelaw (1974), Cherdron, Durst and Whitelaw (1978), Sobey and Drazin (1986), Fearn, Mullin and Cliffe (1990), Durst, Pereira and Tropea (1993)) at sufficiently low Reynolds numbers a unique steady state solution is found and the resulting flow field is symmetric with respect to the channel centerline, with two recirculation zones of equal size whose length increases linearly with the Reynolds number. At a critical value of the Reynolds number that depends on the expansion ratio and the aspect ratio of the duct, the steady symmetric solution becomes unstable and two stable

asymmetric solutions appear. The experimental findings have been confirmed in extensive numerical investigations (Durst et al. (1993), Alleborn, Nandakumar, Raszillier and Durst (1997), Drikakis (1997)).

In mathematical terms, bifurcation occurs when multiple stable solutions to Navier Stokes equations exist (Sobey and Drazin (1986)). Bifurcation properties have been clarified by Fearn et al. (1990) by using experimental and numerical techniques. They showed that the asymmetry arises at a critical Reynolds number due to a pitchfork symmetry-breaking bifurcation where the symmetric state loses its stability. This behavior is called exchange of stability and the bifurcation is classified as supercritical. The dependence of the critical Reynolds number of the symmetry-breaking bifurcation on the expansion ratio was studied numerically by Alleborn et al. (1997), Battaglia, Tavener, Kulkarni and Merkle (1997), and Drikakis (1997). It was found that reducing the expansion ratio tends to stabilize the symmetric solution, i.e., the critical Reynolds number increases for lower expansion ratios.

With increasing the supercritical Reynolds number the asymmetry becomes stronger and at a higher Reynolds number a third separation region appears downstream of the smaller recirculation zone (Durst et al. (1993)). Hawa and Rusak (2001) pointed out that probably the appearance of this additional recirculation zone does not result from another bifurcation point of the channel flow problem.

As the Reynolds number is further increased, the experimental evidence indicates that the flow becomes time dependent, and the unsteadiness is associated with three-dimensional effects (Fearn et al. (1990), Durst et al. (1993)). Additional contributions regarding the symmetry-breaking pitchfork bifurcation include the investigation of Rusak and Hawa (1999), Hawa and Rusak (2001) who carried out a weakly nonlinear analysis of the bifurcation and explained the loss of stability of the symmetric state as a result of the interaction between the effects of viscous dissipation and convection of perturbations for increasing jet Reynolds number.

When further increasing the Reynolds number, the flow finally becomes turbulent. Studies by Abbot and Kline (1962) and Restivo and Whitelaw (1978) have shown that flow asymmetry and hence solution multiplicity remains a feature of flows also in the turbulent regime.

In contrast to the large number of two-dimensional investigations, only few studies of three-dimensional flows in sudden expansion have been performed (Baloch, Townsend and Webster (1995), Chiang, Sheu and Wang (2000), Schreck and Schäfer (2000)).

Chiang et al. (2000) studied the effects of the side walls on the flow structures showing that, for a fixed expansion ratio, a critical maximum aspect ratio exists beyond which an initially symmetric flow becomes asymmetric. This study confirmed the experimental observation that a decrease in the aspect ratio has a stabilizing effect. They investigated the vortical flow structures formed behind the expansion through a topological study of streamline patterns, showing the presence of particle motion screwing towards the plane of symmetry of the channel.

Backward-facing step

As pointed out in the previous section, only few studies of three-dimensional flows in

sudden expansions have been performed. Another particular case of flow in geometries with varying cross-section is represented by the flow over backward-facing steps.

A detailed experimental study of this flow was conducted by Armaly, Durst, Pereira and Schönung (1983). They found that, although the high aspect ratio of their experimental test section (1:36) ensured that the oncoming flow was fully developed and two-dimensional, the flow downstream of the step could become three-dimensional for intermediate Reynolds numbers. Shih and Ho (1994) studied experimentally the flow behind a backward-facing step with small aspect ratio showing that the flow in the separation region is highly three-dimensional due to the presence of side walls. Williams and Baker (1997) investigated numerically the laminar flow over the same backward-facing step geometry used by Armaly et al. (1983) and confirmed the three-dimensionality of the flow. They also found that the presence of side walls results in the formation of a vortex pointing from the wall to the channel midplane. The presence of a similar flow structure that develops near the side wall was shown by Nie and Armaly (2003), who presented the numerical results for three-dimensional laminar forced convection flow over a backward-facing step with aspect ratio 1:8.

The occurrence of a spiraling motion from the side wall to the symmetry plane of the channel was proved by the numerical results of Chiang and Sheu (1998) and by the experiments and the three-dimensional simulations of Tylli, Kaiktsis and Ineichen (2002). This flow structure presents similarities with the screwing motion found in sudden expansions.

The results obtained for the flow over backward-facing steps can enhance our comprehension of similar phenomena occurring in symmetric sudden expansions. Moreover, the investigations performed for the flow over a step show the strong effects of channel side walls and the presence of interesting three-dimensional flow configurations. Therefore, they justify the interest in three-dimensional flows in symmetric sudden expansions and point out the need of further three-dimensional numerical studies for such geometries.

A deep understanding of the structure of the three-dimensional hydrodynamic flow in sudden expansions is essential for studying the effects of an externally applied magnetic field on flows in such geometric configurations. Therefore, to allow a direct comparison between the results for the magnetohydrodynamic flow and the hydrodynamic flow, both types of flow have to be studied in the same geometry. That together with the limited number of results available in the literature motivates the numerical investigation of hydrodynamic flows described in Section 4.2.

2 Formulation of the problem

Let us consider the flow of an electrically conducting fluid in a duct exposed to an externally applied magnetic field $\mathbf{B}$.

The complete set of magnetohydrodynamic (MHD) equations governing the problem under study are obtained by combining the hydrodynamic equations, namely the Navier-Stokes equations and the mass conservation, with Maxwell's equations of electrodynamics.

2.1 Assumptions

The mathematical description of the problem is based on the following assumptions. The fluid is assumed to be incompressible and electrically conducting and the flow is laminar and isothermal. The latter assumption implies that buoyancy forces and thermoelectric effects can be neglected and the Navier-Stokes equations are decoupled from the energy equation.

As an additional assumption the problem is solved in the inductionless approximation, namely the induced magnetic field is negligible compared with the imposed one. Therefore the total magnetic field is simply given by the applied, steady magnetic field $\mathbf{B}_0$. This approximation is valid when the dimensionless parameter $R_m = \mu\sigma L v_0$, called magnetic Reynolds number, is small ($R_m << 1$). This non-dimensional group can be interpreted as the ratio of the induced to the applied magnetic field. Here μ is the magnetic permeability, σ is the electrical conductivity of the fluid and L and v_0 are a characteristic length and a reference velocity. Neglecting the induced magnetic field means that the magnetic induction field is dominated by diffusion and is not affected by the fluid motion.

Since the magnetic field $\mathbf{B}_0$ is steady, the electric field $\mathbf{E}$ is irrotational ($\nabla \times \mathbf{E} = 0$) and therefore can be represented as the negative gradient of an electric potential ϕ, i.e. $\mathbf{E} = -\nabla\phi$.

The displacement current ($\sim \partial\mathbf{E}/\partial t$) introduced by Maxwell in Ampère's law, which represents the influence of time-varying electric fields on the magnetic field is also neglected since its influence on MHD flows is many orders of magnitude smaller than the phenomena studied here (Shercliff (1965)).

2.2 Governing equations

Magnetohydrodynamic equations are often written in dimensionless form so that the relative strengths of the different terms can be inferred by the size of multiplying non-dimensional groups, whose magnitudes give an idea of the relative importance of the various forces acting on the flow. Under the assumptions described in the previous section, the flow of an electrically conducting fluid in a imposed magnetic field is governed by the following dimensionless equations accounting for the conservation of momentum, mass and charge and by Ohm's law (Shercliff (1965), Müller and Bühler (2001)):

$$\frac{\partial}{\partial t}\mathbf{v} + (\mathbf{v}\cdot\nabla)\,\mathbf{v} = -\nabla p + \frac{1}{Re}\nabla^2\mathbf{v} + N\,(\mathbf{j}\times\mathbf{B})\,, \tag{1}$$

$$\nabla\cdot\mathbf{v} = 0, \tag{2}$$

$$\nabla\cdot\mathbf{j} = 0, \tag{3}$$

$$\mathbf{j} = -\nabla\phi + \mathbf{v}\times\mathbf{B}. \tag{4}$$

By combining the equations (3) and (4) a Poisson equation for the electric potential is obtained:

$$\nabla^2\phi = \nabla\cdot(\mathbf{v}\times\mathbf{B})\,. \tag{5}$$

In these equations the variables $\mathbf{v}$, p, $\mathbf{j}$, $\mathbf{B}$ and ϕ denote the velocity, the pressure, the current density, the magnetic field and the electric potential scaled by the reference quantities v_0, ρv_0^2, $\sigma v_0 B_0$, B_0 and $v_0 B_0 L$, respectively. Here, the half width of the channel is chosen as characteristic length L and the average velocity in a particular cross-section of the duct is taken as velocity scale v_0. The quantity B_0 is the magnitude of the imposed magnetic field. The fluid properties, namely the density ρ, the electrical conductivity σ and the kinematic viscosity ν are assumed to be constant. By assuming a small magnetic Reynolds number ($Re_m << 1$), the main effect of the interaction between the electromagnetic field and the moving fluid is associated with the appearance of the electromagnetic force $\mathbf{j}\times\mathbf{B}$. Hydrodynamic equations and Maxwell's equations are therefore coupled by the Lorentz force and the induced electric field $\mathbf{v}\times\mathbf{B}$ present in Ohm's law.

The dimensionless groups governing the problem are the Reynolds number

$$Re = \frac{v_0 L}{\nu},$$

and the interaction parameter or Stuart number

$$N = \frac{\sigma L B_0^2}{\rho v_0}.$$

The Reynolds number, as in conventional fluid mechanics, represents the ratio of inertia to viscous forces and the interaction parameter gives a measure of the ratio of electromagnetic to inertial forces. In the following an additional non-dimensional group called Hartmann number is employed, whose square characterizes the ratio of electromagnetic to viscous forces

$$Ha = \sqrt{NRe} = LB_0\sqrt{\frac{\sigma}{\rho\nu}}.$$

The present study is concerned with channels with walls of finite thickness t_w and finite conductivity σ_w. Therefore part of the current flowing in the fluid may close its path in the walls and the equations

$$\mathbf{j}_w = -\frac{\sigma_w}{\sigma}\nabla\phi_w, \qquad \nabla \cdot \mathbf{j}_w = 0 \tag{6}$$

have to be solved in the solid domain.

Henceforth the ratio of the electric conductance of the wall to the fluid one will be indicated by the conductance parameter

$$c = \frac{\sigma_w t_w}{\sigma L}.$$

As boundary condition at the fluid-wall interface the no-slip condition is applied

$$\mathbf{v} = 0.$$

The electric boundary conditions at the fluid-solid interface state the continuity of wall-normal component of current density and electric potential

$$j_n = j_{nw}, \qquad \phi = \phi_w.$$

The normal component of the electric current vanishes at the external surface of the wall because the surrounding medium is assumed to be insulating.

2.3 Basic MHD flow characteristics

In this section the main features of the fully developed MHD flow in a duct with square cross-section are described. The term fully developed denotes a condition where the velocity profile is no longer changing in the main flow direction, i.e. a flow that has reached a steady state driven by a constant pressure gradient. The study of fully developed flow under a uniform applied magnetic field is useful because the equations can be solved analytically for different cases, and the solutions can be used as benchmarks for numerical algorithms. In addition, fully developed solutions predict some phenomena of general interest, especially the existence of different types of boundary layers, which are important for the understanding of MHD flows.

In the present case the coordinate system is chosen in such a way that x, y and z are the streamwise, the vertical and the spanwise direction respectively. The origin of the system is placed at the centre of the channel cross-section. The fluid flows in the x direction with velocity $\mathbf{v} = u\mathbf{x}$ under the influence of an external uniform magnetic field with a constant component in the y direction, $\mathbf{B} = B_0\mathbf{y}$. Walls perpendicular to the magnetic field are called *Hartmann walls* and the walls tangential to the magnetic field are named *side walls* (Fig.3).

For sufficiently high Hartmann numbers the flow forms an inviscid core where Lorentz forces balance pressure forces and thin boundary layers of different type (Shercliff (1953)).

Close to the Hartmann walls boundary layers with high velocity gradients are present to satisfy the no-slip boundary condition. These layers are called *Hartmann layers* and their thickness δ_{Ha} is proportional to Ha^{-1}. In these boundary layers, the velocity profile is basically determined from a balance between Lorentz and viscous forces and the electric currents induced in the core can close their path through these layers. The electric conductivity of the duct walls influences the distribution of the current and determines the flow pattern in the core.

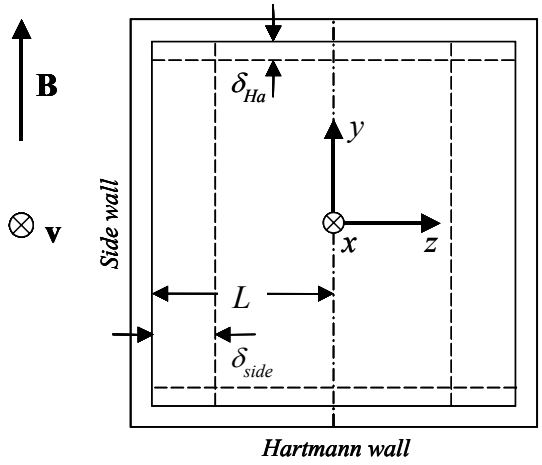

Figure 3: Sketch of the duct cross-section; δ_{Ha} and δ_{Side} denote the thickness of the Hartmann and side layers and L is the characteristic length scale.

Fig.4 shows the velocity distribution along the y direction for a range of Hartmann numbers. For high Hartmann numbers a flat velocity profile exists in the core region with exponential decay to zero within thin viscous boundary layers.

Near the side walls a different kind of boundary layer occurs, whose thickness δ_{Side} scales as $Ha^{-1/2}$. In these boundary layers the velocity is considerably higher than that in the core and for large Hartmann numbers a local minimum is present when approaching the core (Fig.5).

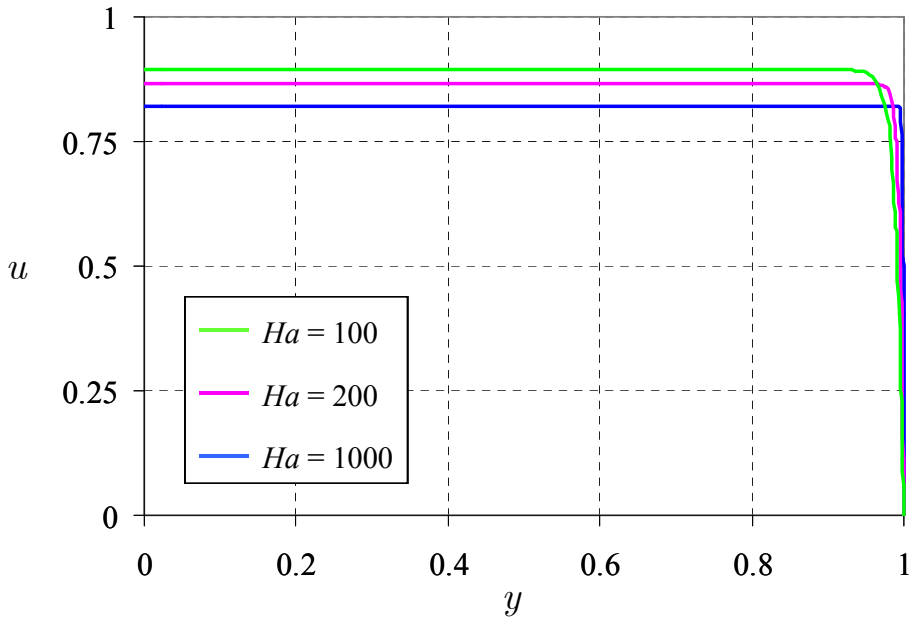

Figure 4: Velocity distribution along the y direction at $z = 0$ for $c = 0.1$ and different Hartmann numbers Ha.

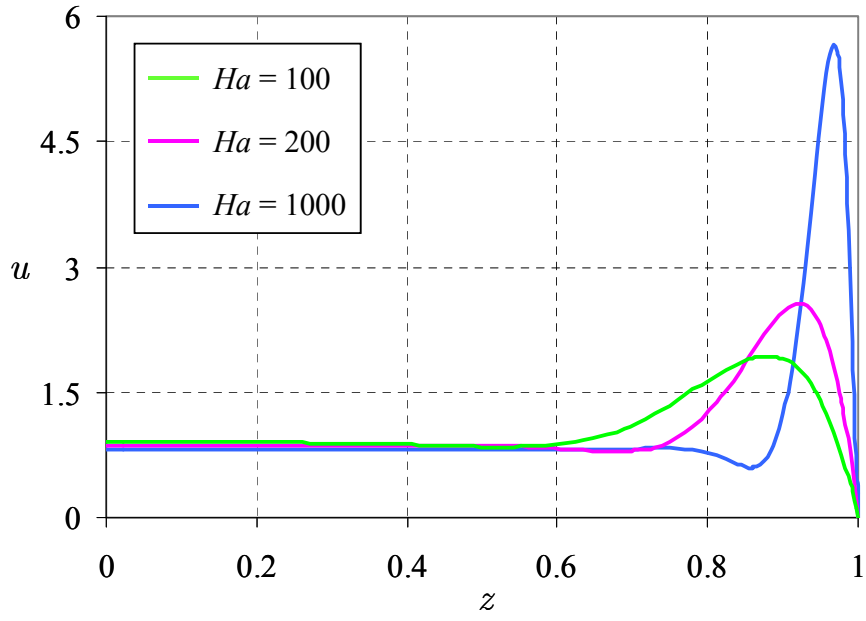

Figure 5: Velocity distribution along the transverse direction z at $y = 0$ for $c = 0.1$ and various Hartmann numbers Ha.

2.4 MHD flow modelling using CFX

The present investigation is carried out using the commercial package CFX 5.6, which is based on the finite volume method and on a modified form of the SIMPLE algorithm for pressure-velocity coupling to ensure mass conservation (Patankar (1980)). The discrete system of linearized equations is solved by an iterative procedure. The solution is obtained by using a multigrid process that consists in performing the iterations at the beginning of the run on a fine mesh and then on progressively coarser virtual grids. Afterwards the results are transferred back to the fine mesh. This technique improves the performance of the solver and the convergence rate.

Since magnetohydrodynamic equations are not available as an option in CFX-5, these equations have to be implemented in the code by means of suitable Fortran subroutines. In order to describe MHD flows it is necessary to introduce the Lorentz force as a body force in the momentum equation and to solve a Poisson equation for the electric potential.

Incompressible hydrodynamic flows in CFX are described by the following set of equations for conservation of momentum, mass and energy:

$$\frac{\partial \rho \mathbf{v}}{\partial t} + \rho \left(\mathbf{v} \cdot \nabla \right) \mathbf{v} = -\nabla p + \nabla \rho \nu \nabla \mathbf{v} + S_m, \tag{7}$$

$$\nabla \cdot \mathbf{v} = 0, \tag{8}$$

$$\frac{\partial \rho c_p T}{\partial t} + \nabla \cdot \left(\rho c_p T \mathbf{v} \right) = \nabla \lambda \nabla T + S_T, \tag{9}$$

where ρ, ν, c_p and λ are the density, the kinematic viscosity, the specific heat capacity at constant pressure and the thermal conductivity, respectively. The source terms in the momentum and in the energy equations are denoted by S_m and S_T.

Starting from a former implementation of MHD equations in CFX, used for instance to simulate metal arc welding processes (Spille-Kohoff (2004)), modifications and improvements are made to get a reliable tool for investigating numerically MHD flows in various geometries exposed to a magnetic field of arbitrary orientation. In the previous implementation a transport equation was solved for the electric potential, which was described by an additional variable. This equation cannot be solved in a solid domain and therefore it cannot be employed to describe the MHD flow in channels with electrically conducting walls of finite thickness and to analyze the current and potential distribution in the walls. To overcome this problem, the CFX-temperature is used to represent the electric potential. By comparing equations (5) and (9) it is evident that a purely diffusive equation is required to describe the electric potential evolution. With this approach the subroutines used to calculate the current density have to be changed considering that the currents driven by the static electric field can be interpreted as CFX-heat fluxes. As will be described in the following, also the form of the Lorentz force introduced as a source term in the momentum equation has been modified.

In order to implement the MHD equations in dimensionless form, since CFX deals with dimensional quantities, CFX fluid and solid properties have to be selected in a

proper way. Comparing the equations (7)-(9) solved in CFX with those governing the problem under study (1)-(5) the following relations for the density and the kinematic viscosity are obtained:

$$\rho = 1,\ \nu = Re^{-1}.$$

Regarding the energy equation the specific heat capacity is arbitrary both for the fluid and the solid material whereas the thermal conductivity assumes different values in the fluid and in the wall related to the electrical conductivity of the two materials:

$$\lambda = 1,\ \lambda_w = \frac{\sigma_w}{\sigma}.$$

Here σ_w and σ are the electrical conductivity of the wall and the fluid respectively.

The source term S_m in the momentum equation (7) is given by the product of the interaction parameter N and the Lorentz force $\mathbf{L}$ expressed by

$$\mathbf{L} = \mathbf{j} \times \mathbf{B} = -\nabla\phi \times \mathbf{B} + (\mathbf{v} \times \mathbf{B}) \times \mathbf{B}. \tag{10}$$

Using vector identities the second term of the electromagnetic force can be written as $(\mathbf{B} \cdot \mathbf{v})\mathbf{B} - B^2\mathbf{v}$. This latter behaves as a drag force in a plane perpendicular to the magnetic field. Through simple mathematical transformations the Lorentz force can be expressed as the sum of a specified source of momentum and a fluid resistance:

$$\begin{aligned} L_x &= \partial_z\phi B_y - \partial_y\phi B_z + aB_x - B^2u = S_{spec,x} - C_{R1}u \\ L_y &= \partial_x\phi B_z - \partial_z\phi B_x + aB_y - B^2v = S_{spec,y} - C_{R1}v \\ L_z &= \partial_y\phi B_x - \partial_x\phi B_y + aB_z - B^2w = S_{spec,z} - C_{R1}w \end{aligned} \tag{11}$$

where C_{R1} is a linear resistance coefficient equal to B^2, $S_{spec,i}$ is the i-component of a certain source term and a is given by $B_xu + B_yv + B_zw$.

The proposed implementation applies to arbitrary geometries and orientation of the external magnetic field and forms an efficient tool for MHD analyses.

The default boundary condition for the velocity at the fluid-wall interface is the no-slip condition $\mathbf{v} = 0$. On the external surface of the walls a zero flux condition is applied for the current density. The distribution of velocity and electric potential imposed as inlet boundary conditions is obtained from calculations in which periodic boundary conditions are used along the streamwise direction to simulate fully developed flows.

Another aspect that has to be carefully considered in CFD simulations is the mesh used to discretize the computational domain. It is important to resolve properly the geometric features that affect the flow and the regions where the largest gradients of the variables occur, such as, in the present study, the zone near the expansion and the boundary layers that develop along the walls. By increasing the Hartmann number, since the thickness of the boundary layers decreases, the need of resolving adequately these layers, while preserving the mesh quality by avoiding elements with high aspect ratio and ensuring a smooth transition between adjacent grids, leads to a progressive rise in the total number of nodes. As a consequence, restrictions on the accuracy of the solution at high Hartmann number are related to limitations in the memory storage and computer capabilities.

The mesh employed changes depending on the Hartmann number. In the flow direction a biased grid is used to resolve suitably the zone around the expansion in which high gradients are present. Further upstream and downstream where the flow approaches the fully developed conditions the number of nodes per unit length is reduced. In the cross-section of the channel the points are clustered close to the walls. More detailed issues concerning the resolution of boundary layers and the fundamental requirements that a grid has to fulfil will be discussed in the next chapter.

Convergence of the solution is judged both considering the value of the residuals of velocity and mass conservation and by monitoring the solution variables in fixed points in the computational domain during the run. Values of interest are the maximum velocity in the side layers both close to the expansion and in the downstream flow region where fully developed conditions are expected to establish, and the potential difference between the side walls at given axial positions. The calculations of 3D MHD flows are stopped when all the root mean square residuals are equal or less than 10^{-5} and the variables at the monitored locations remain constant.

3 Validation of the code

3.1 Introduction

The validation process is a fundamental step required when a code is modified and new features are implemented. It allows to proof the reliability of the implementation and to find possible mistakes.

The selected validation cases have been chosen because they permit to draw interesting conclusions that can be applied to the following study. Moreover, they show the ability of this numerical approach to predict flow features like high velocity jets and three dimensional currents that are present also in MHD flows through sudden expansions.

3.2 Fully developed channel flow

As a first validation case the fully developed MHD flow in a duct with rectangular cross section is analyzed. It is characterized by the fact that all the physical variables are independent of the coordinate in the direction of motion except for the pressure whose axial gradient is constant. The fluid flows in the x direction driven by this pressure gradient and a uniform magnetic field is imposed parallel to the y axis (Fig.6). The channel has same dimensions as the entrance duct of the expansion that will be analyzed later. The non-dimensional half width is one and the half size along magnetic field lines is 0.25. All the walls have the same electric conductivity and the conductance parameter c, which gives the ratio of the conductance of the wall to the fluid material, is assumed equal to $c = 0.1$. This quantity together with the Hartmann number Ha are the only parameters governing the fully developed MHD flow.

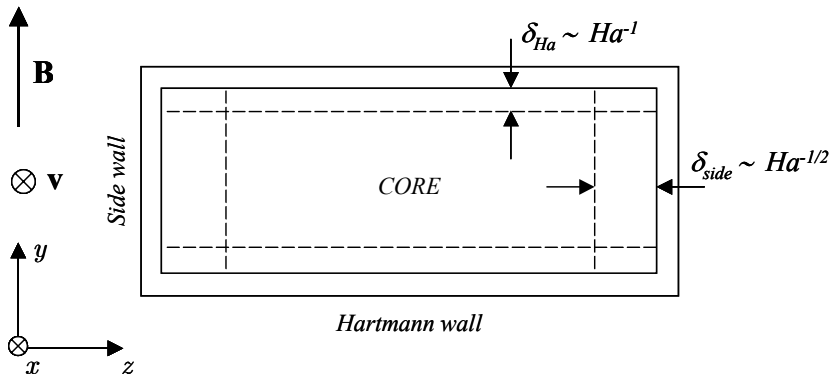

Figure 6: Rectangular duct in a uniform magnetic field. δ_{side} and δ_{Ha} denote the thickness of the side and the Hartmann layers, respectively.

The computed results are compared with the analytical solution obtained following the approach of Walker (1981), which is valid for high Hartmann numbers ($Ha \gg 1$) and for conductance parameters such that $cHa \gg 1$. The latter assumption states that the walls perpendicular to the magnetic field are better conducting than the adjacent boundary layers. Therefore currents flow preferentially in the walls rather than in the

Hartmann layers. For large enough Hartmann numbers, Walker divides the cross section of the duct in an inviscid core, where electromagnetic and pressure forces balance each other, and thin boundary layers in which viscous effects are confined. The solution in the core region shows that the velocity is uniform and does not change along magnetic field lines and the potential varies linearly in the transverse direction z.

In the side layers the solution is found by eliminating currents and velocity from the governing equations, deriving in this way a separable equation for the electric potential, which is solved in terms of Fourier series.

The study of the effect of the mesh on the accuracy of the solution has been performed for various Hartmann numbers (Ha = 100, 300, 500, 1000). From the analysis of the results and the comparison with the analytical solution it is possible to obtain some basic guide lines for creating an appropriate grid to resolve characteristic MHD flow features.

The velocity profile in the side layer is characterized by a strong gradient close to the wall, a high velocity jet and, for sufficiently large Hartmann numbers, by a local minimum that appears near the interface between the core region and the layer. These flow features become stronger with increasing Hartmann number and determine the structure of the mesh needed to get an accurate solution.

Four meshes have been selected, which resolve one after the other the regions of interest in the side layer.

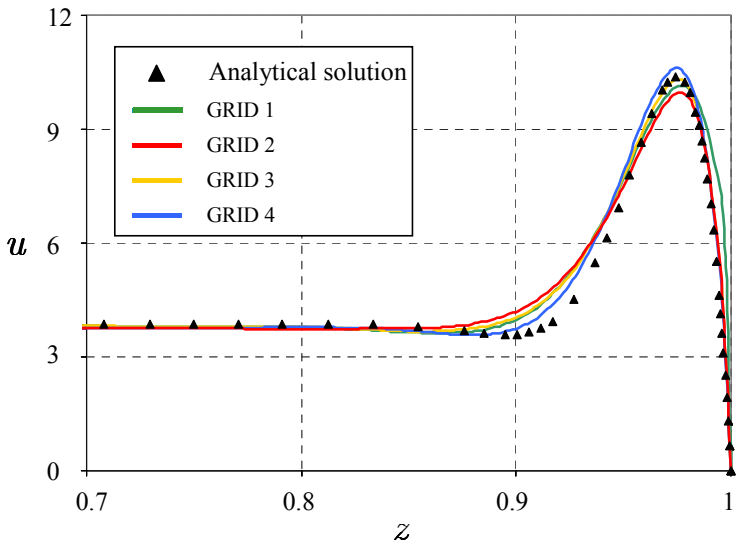

Figure 7: Numerical results for axial velocity at $y = 0$ for $c = 0.1$ and $Ha = 500$ calculated by using four different meshes. The solid symbols indicate the analytical solution.

Fig.7 shows the velocity profile along the z direction for the flow at $Ha = 500$. Starting from the results obtained using *grid* 1, first the mesh is refined near the side wall to predict with precision the high velocity gradients (*grid* 2). The same number of nodes is used in the side layer for both the grids. As a consequence by narrowing the first cell at the fluid-wall interface the resultant mesh in the rest of the layer is coarser

than *grid* 1. It leads to a reduction of the maximum velocity and a larger deviation from the analytical solution at the border of the layer.

The next step consists of increasing the number of nodes in the zone where the highest velocities are present in order to reach the maximum jet velocity (*grid* 3). The results show that it is still necessary to refine the grid where the local minimum of velocity occurs (*grid* 4). The resultant mesh consists of 150 nodes in the z direction, of which 27 are contained in a region of thickness $\Delta z = 0.1$ close to the wall. By comparing with the analytical solution the velocity distribution along the z coordinate calculated by using *grid* 4 the maximum relative error is about 2%. The results can be further improved by increasing the number of nodes in the duct cross-section proving that the numerical approach is able to predict thoroughly the fully developed flow profile in a rectangular duct.

However, since these results are used as inlet boundary conditions for the 3D calculations for which a fine grid is required not only near the walls but also across the expansion, a restriction on the total number of nodes used to discretize the cross-section of the inlet duct is imposed due to limitations of the memory storage.

For the flow at $Ha = 1000$ the boundary layers are very thin and next to the walls there are strong velocity gradients. It has been verified that, in order to predict with high accuracy the velocity profile in the side layers, a large number of nodes is required, which is beyond the above mentioned limit.

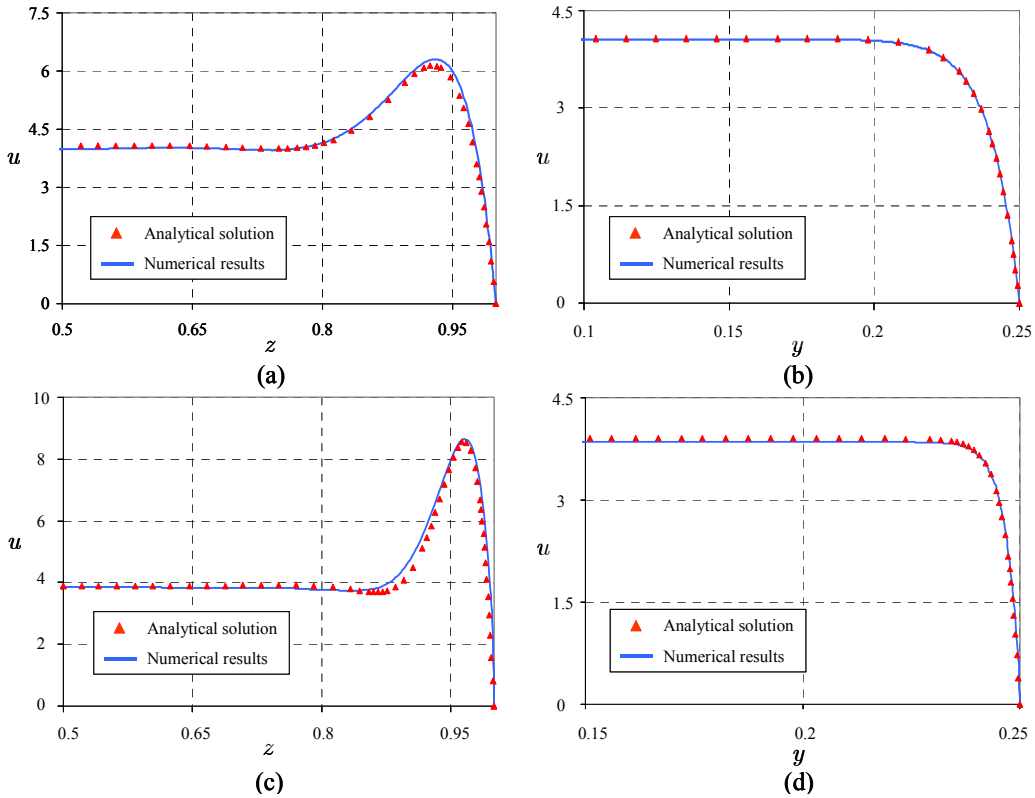

Figure 8: Numerical and analytical solution for axial velocity for $c = 0.1$, $Ha = 100$ (a)-(b) and $Ha = 300$ (c)-(d).

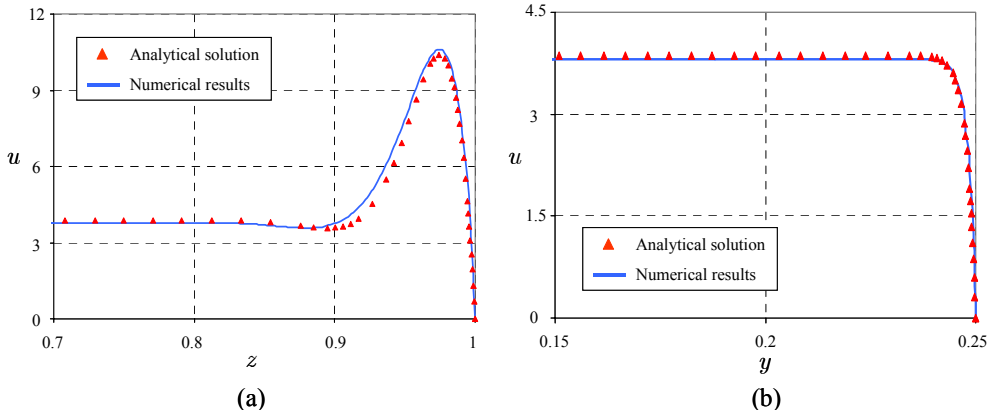

Figure 9: Calculated velocity profiles are compared with the analytical solution for $c = 0.1$ and $Ha = 500$.

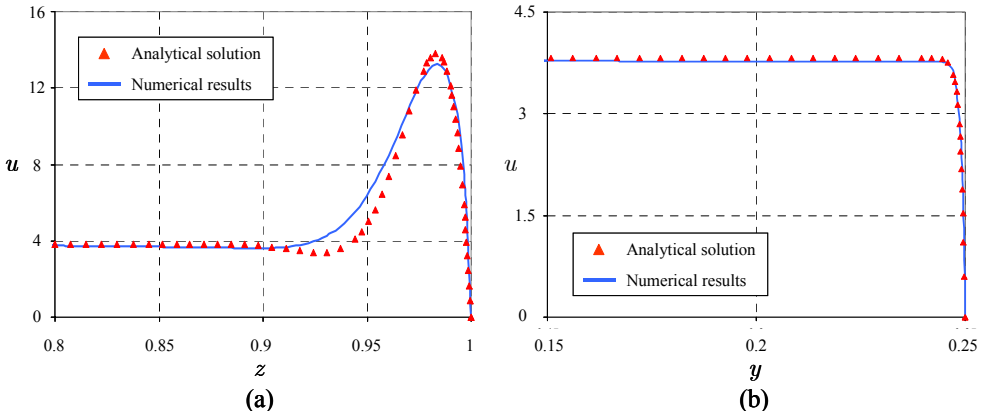

Figure 10: Comparison between the computed velocity profiles and the analytical solution for $c = 0.1$ and $Ha = 1000$.

The results obtained by employing a grid valid also in the three dimensional calculations are shown in Fig.8, 9 and 10. The axial velocity is plotted versus the directions y and z and it is compared with the analytical solution. For $Ha = 1000$ the used mesh allows to reach a maximum velocity in the side layer within an accuracy of about 4% of the analytical solution but overestimates the velocities near the core-side layer interface.

Concerning the resolution of the Hartmann layers the investigation shows that it is a critical point due to the presence of high velocity gradients. Without a sufficiently fine grid, which consists in the presence of at least 4 nodes inside the layer, the fast decreasing of the core velocity to zero at the wall cannot be properly represented and also a reduction of the core velocity is observed. Since the thickness of the Hartmann layer decreases with raising the Hartmann number ($\delta_{Ha} \sim Ha^{-1}$), the total number of nodes required along magnetic field direction to discretize the channel cross section increases with the Hartmann number. For the flow at $Ha = 500$ about 35 points have to be used. In Fig.8(b), (d), 9(b) and 10(b) the computed velocity is plotted along the vertical direction y and it is compared with the analytical solution for $Ha = 100$, 300, 500 and 1000, respectively. A fairly good agreement is found between the solutions.

3.3 MHD flow in plane sudden expansion

The two-dimensional MHD flow in symmetric sudden expansions with expansion ratio of four and perfectly conducting walls is investigated. The fluid flows along the x direction and the imposed magnetic field is uniform and parallel to the y axis (Fig.11). The parameters governing the problem, namely the Hartmann number Ha and the interaction parameter N, are chosen according to the ones reported by Aleksandrova, Molokov and Bühler (2003) and this permits a direct comparison with the numerical results in the literature so that the present computational approach can be further validated. Moreover some useful information about grid properties required to get an accurate numerical solution can be inferred.

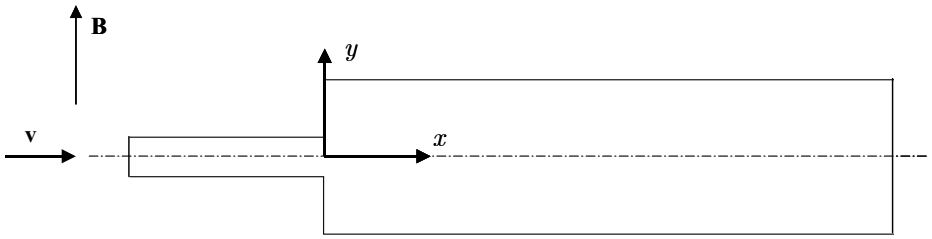

Figure 11: Sketch of the plane symmetric sudden expansion.

Three cases are analyzed and the corresponding dimensionless groups are reported in Table 1.

	Ha	N	$Re = Ha^2/N$
case 1	40	1.6	1000
case 2	400	15.7	10189
case 3	1000	1000	1000

Table 1: Governing parameters for the three cases investigated.

To ensure that the computed solutions predict correctly the flow configuration, a grid sensitivity study has been performed to investigate the effects of mesh resolution in the region across the expansion and around the corners. Details of the grid-independent tests are presented for the highest Hartmann number ($Ha = 1000$). For this study, non-uniform mesh distributions have been used with a finer grid near the expansion and in the vicinity of the Hartmann walls. Fig.12 shows an example of the grid used for the calculations. Four meshes have been selected whose main characteristics are summarized in Table 2. In the table Δx_1 indicates the length of the first cell immediately behind the enlargement of the channel and the cell located symmetrically with respect to the y axis has the same size, Δy_1 is the height of the first control volume close to the wall of the small duct and the height of the cell in the large duct immediately adjacent to this control volume is called $\Delta y_{1\,exp}$.

By comparing the calculated solution for $Ha = 1000$ with that in the literature, the maximum difference occurs in the region close to the expansion corner located at the

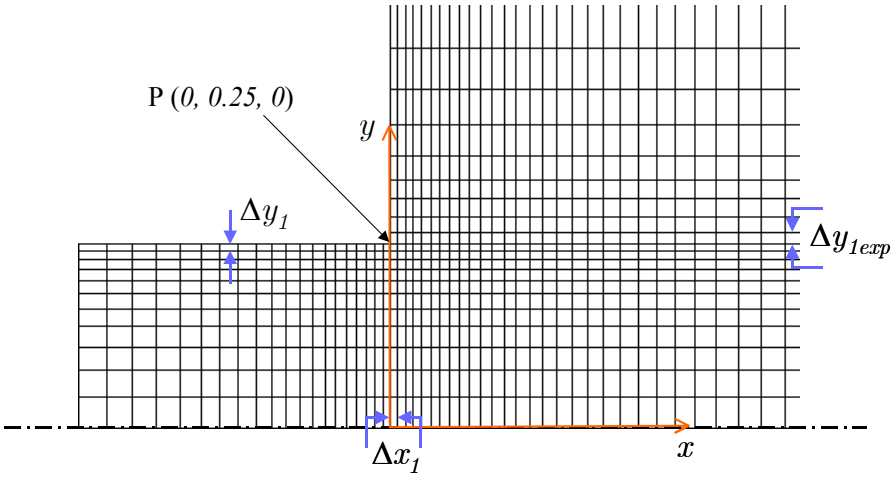

Figure 12: Sample of the grid used for the calculations.

point P $(0, 0.25, 0)$ in which a high velocity jet is present. Therefore the deviation ε from the reference value of the maximum u velocity at $x = 0$ is taken as a sensitive measure of the accuracy of the solution.

The grid independent study has been performed starting from the results obtained using *grid A*. For this mesh the difference ε is larger than 13 %. As shown in Table 2, a first improvement in the solution is obtained by increasing the grid density close to the expansion (*grid B*), namely by narrowing the length Δx_1. The results are further improved by raising the number of nodes near the external wall of the small duct (*grid C*), corresponding to a reduction in the height Δy_1. A perfect agreement is reached by decreasing the height $\Delta y_{1\ exp}$, that is by smoothing the transition between the fine grid close to the wall of the small channel and the mesh in the core region of the large duct (*grid D*). In this way the refinement of the grid across the expansion and around the corner (point P) is completed. It is worthwhile noticing that in this case with perfectly conducting walls the refinement of Hartmann layers does not affect the solution in the core as all the currents close through the wall. The resolution of this boundary layer has only local effects since it allows to calculate properly the large velocity gradients that take place to satisfy the no-slip condition at the wall.

The numerical results, obtained employing *grid D*, are compared with the solution given by Aleksandrova et al. (2003). In Fig.13 the streamwise velocity component is

GRID	Nodes in the *Ha*-layer	Δx_1	Δy_1	$\Delta y_{1\ exp}$	ε (%)
A	1	0.008	0.0005	0.002	13.7
B	1	0.004	0.0005	0.002	4.5
C	3	0.004	0.0002	0.002	3.4
D	3	0.004	0.0002	0.0003	1.1

Table 2: Main features of meshes used for the grid independent study for $Ha = 1000$. ε is the deviation from the value in the literature (Aleksandrova et al. (2003)) of the maximum velocity calculated along y at $x = 0$.

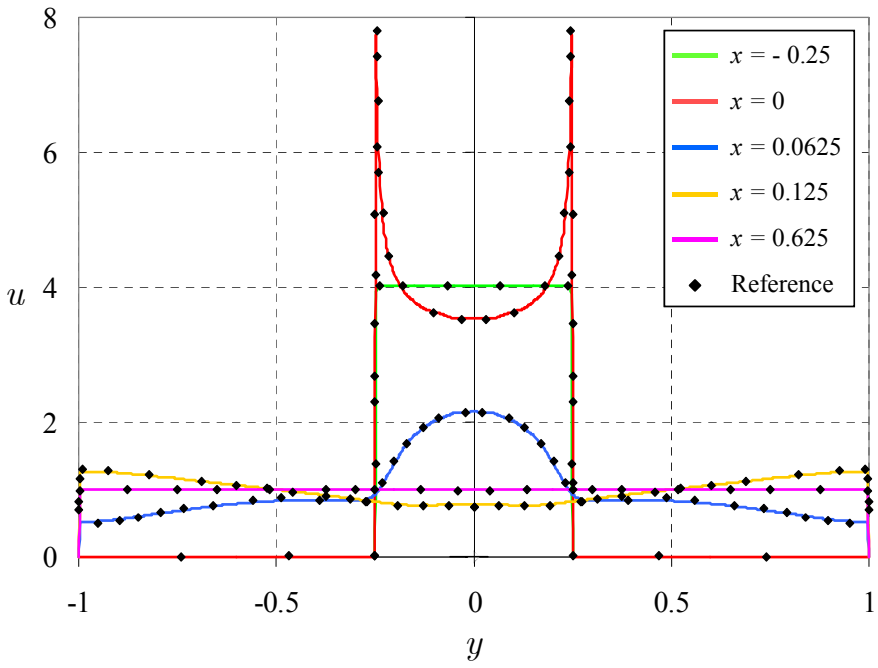

Figure 13: Velocity component u versus the vertical direction y, parallel to the magnetic field, at different axial positions. The results are calculated using *grid D*. The symbols correspond to the solution reported by Aleksandrova et al. (2003).

plotted along the vertical coordinate y at various axial positions for $Ha = 1000$. At the inlet of the channel the flow is fully developed. Approaching the expansion there is a reduction of the velocity in the core and an increase close to the Hartmann walls leading to the formation of a characteristic M-shaped profile along the field direction. The velocity of the jets rises and reaches the maximum value at the junction between the small and the wide duct ($x = 0$). This is due to the fact that the flow redistributes quickly in the large channel following the wall profile (Fig.14). This comparison shows that the employed numerical tool is able to predict accurately the presence of high velocity jets.

In Fig.15 the velocity component u is plotted along the axial coordinate at $y = 0$. The flow is fully developed both upstream and downstream and the strongest modifications in the velocity distribution take place near the expansion in a thin layer parallel to the applied magnetic field.

As mentioned at the beginning of this section, two other cases have been studied (Table 1). The results show similarly a very good agreement with the reference solution.

This analysis not only increases our confidence in the numerical approach but highlights the importance of gathering nodes in the region around the expansion and the corners of the duct. In the following investigations, channels with walls of finite conductivity are considered where the current can flow also through the boundary layers and along the walls. As a consequence, the resolution of these layers becomes fundamental for a correct prediction of the flow pattern in the entire computational domain. This

observation sheds light on the problems related to memory storage and computational time, which arise simulating three dimensional MHD flows at high Hartmann numbers while preserving the accuracy of the solution. This is due to the fact that the thickness of the boundary layers decreases with increasing the Hartmann number and a minimum number of nodes is always required inside these layers.

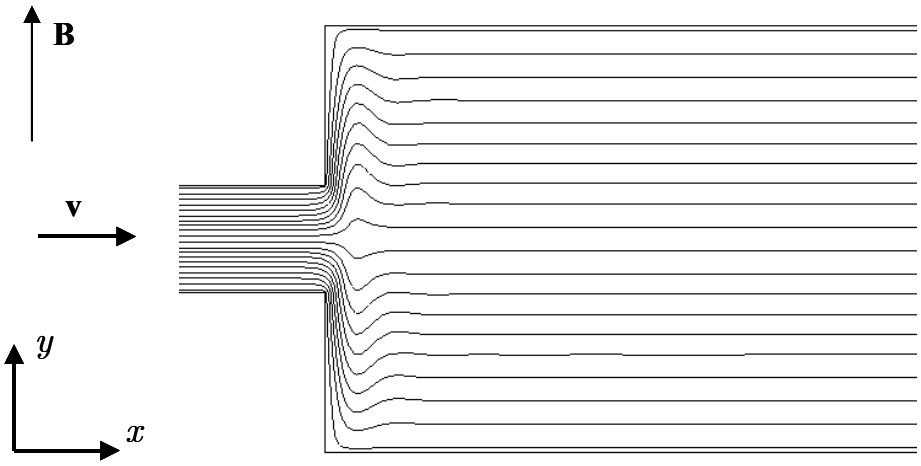

Figure 14: Velocity streamlines for the flow at $Ha = 1000$ and $N = 1000$.

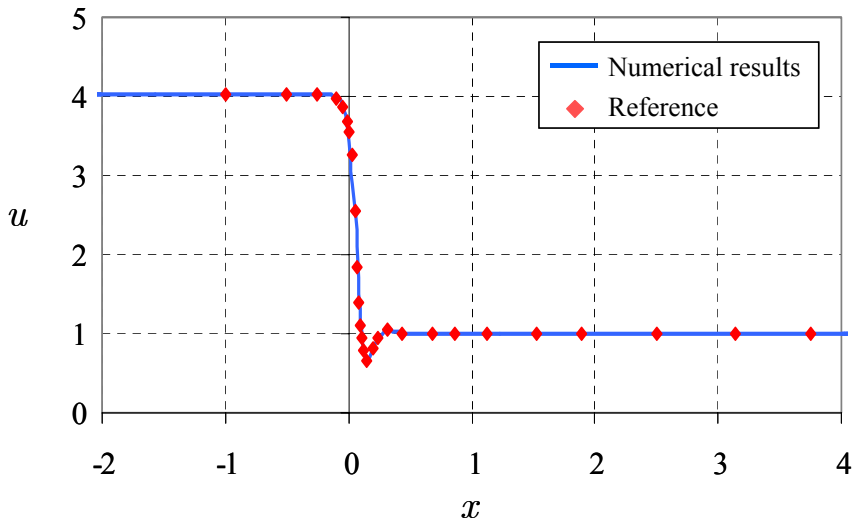

Figure 15: Velocity component u along the channel midline $y = 0$ for $Ha = 1000$ and $N = 1000$. The solution is computed on *grid D*. The symbols indicate results from the literature (Aleksandrova et al. (2003)).

3.4 3D MHD flow under a non-uniform magnetic field

Let us consider the flow of an electrically conducting fluid in a rectangular duct with constant cross-section exposed to an externally applied non-uniform magnetic field aligned with the y-axis (Fig.16).

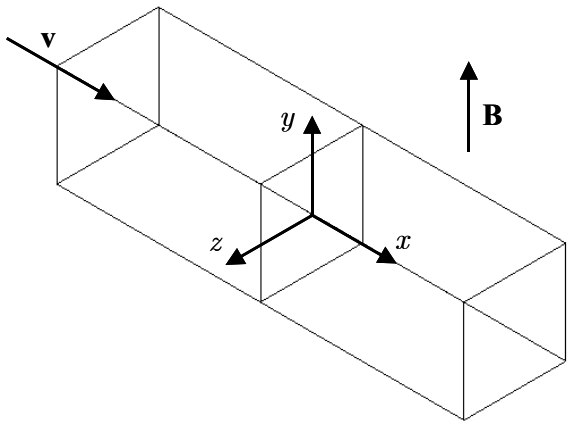

Figure 16: Sketch of the geometry. The cross section marked inside the duct is located at $x = 0$ and corresponds to the region with the largest magnetic field gradient.

In accordance to the formulation of Sterl (1990) the imposed magnetic field, which varies in the streamwise direction, has the following form:

$$B_y(x) = \frac{1}{1 + e^{-x/x_0}}. \tag{12}$$

If x_0 is positive B_y increases from zero to one with a steep gradient, if x_0 is negative the magnetic field has the opposite profile. This shape of the applied field can model the entrance or the exit of a magnet.

The magnetic field is assumed to have only one component in the y direction since, as verified by Sterl (1990), applying an additional component B_x in the axial direction does not affect significantly the solution. It implies only a small reduction of the pressure drop and of the amount of fluid driven into the side layers. This accords with the arguments discussed by Talmage and Walker (1987) and Walker (1986a).

The numerical results for the flow at $Ha = 50$, $N = 1000$, $c = 0.1$ and $x_0 = 0.15$ are described and compared with the ones in the literature (Sterl (1990)). A non equally spaced grid is used clustered in the region of large magnetic field gradient and in the boundary layers that develop along the duct walls.

Fig.17 shows the comparison between the computed solution and the reference results for characteristic quantities that vary along the x-direction, namely the pressure along the centerline of the duct ($z = 0$) and at the side wall ($z = 1$), the axial pressure gradient and the transverse potential difference. In the figure the strength of the applied magnetic field is also indicated. A very good agreement is found between the two solutions. Some deviation occurs in the transverse potential difference in the downstream region. It can be explained considering that the actual results are obtained using a much higher

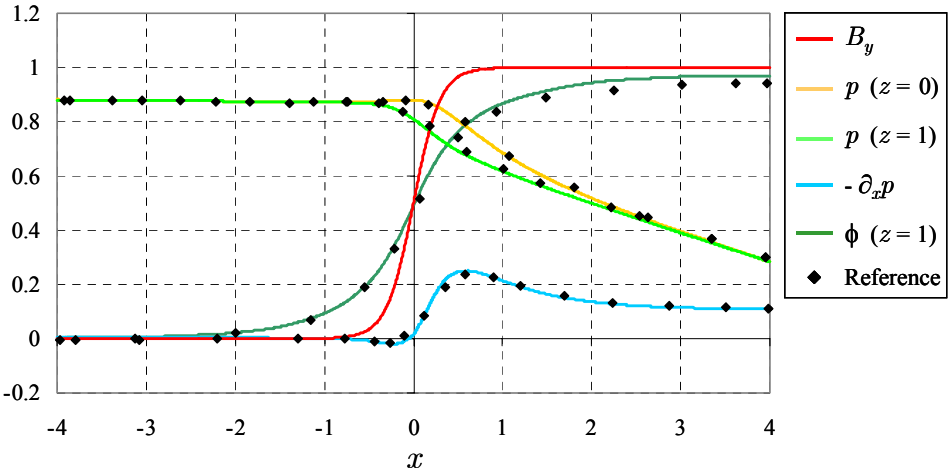

Figure 17: Characteristic quantities plotted along the axial direction for the flow in a non-uniform magnetic field at $Ha = 50$, $N = 1000$, $c = 0.1$. The symbols indicate the reference results (Sterl (1990)).

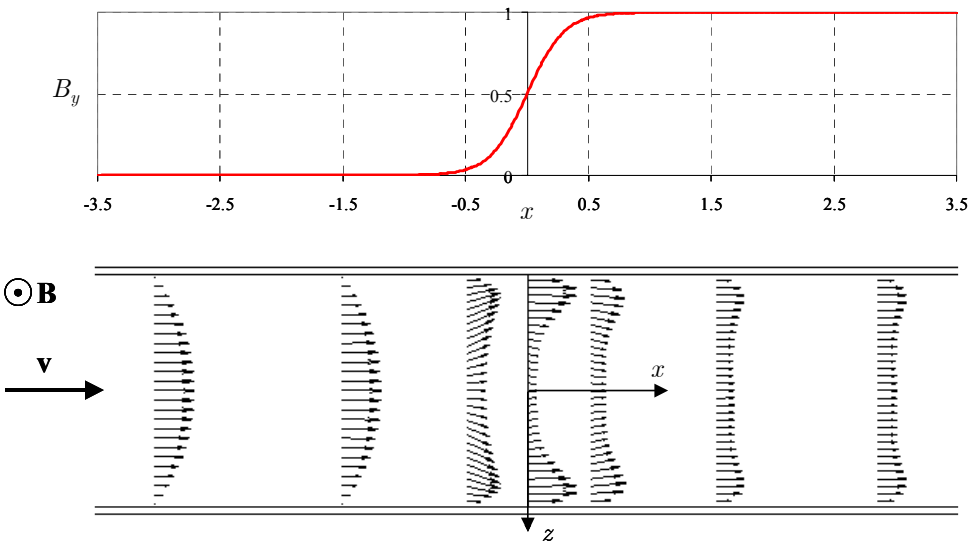

Figure 18: The upper curve is the imposed magnetic field. The vector plots illustrate the redistribution of the velocity in the plane $y = 0$ perpendicular to the B-field for the flow at $Ha = 50$, $N = 1000$, $c = 0.1$.

numerical resolution than what was possible in the past. This argument may explain the observed difference at the exit of the geometry.

In Fig.18 the velocity distribution is shown on the symmetry plane $y = 0$ perpendicular to the magnetic field. The velocity vectors across the channel are plotted at various axial locations. At the entrance the velocity profile is purely hydrodynamic. Approaching the zone of inhomogeneous magnetic field the velocity profile begins flattening in the core region and velocity jets start arising close to the side walls.

The main typical phenomena occurring in the duct can be explained considering that, due to the variation of the magnetic field in the streamwise direction, an axial potential difference is generated, which drives currents in flow and counter flow direction. The resulting Lorentz force acting in the z direction towards the centre of the channel have to be balanced by a pressure gradient. Hence the pressure is higher in the middle than on the side walls (Fig.17). The induced axial currents close their path throughout the width of the duct and these transverse currents are responsible for a negative net Lorentz force that opposes the flow. The fluid try to bypass this braking region by flowing close to the lateral walls where the retarding electromagnetic force is weaker. As a result, the velocity is strongly reduced in the core and increased near the walls.

This study introduces some of the 3D MHD phenomena, which arise if the induced potential difference varies in the axial direction. Such variation can be caused by a non-uniform magnetic field as in the present case, by a reduction of the x-component of the velocity observed in expansions or bends, or because of varying conductance properties of the channel walls. In the following chapter the additional and new features characterizing 3D MHD flows in ducts with an abrupt change in the cross-section are described focusing on flow pattern, current distribution and the important role of the magnetic field in damping separation effects.

4 Results and discussion

As an application of the developed computational tool, the MHD flow in sudden expansion of rectangular ducts is investigated. The geometry features and the coordinate system are in accordance with the ones described in Chapter 1.

4.1 Introduction

The study of flow separation and the determination of the resultant changes in the flow field are fundamental problems of fluid dynamics. Considering the flow in sudden expansions, a pressure increase occurs behind the cross-section enlargement and, due to this adverse pressure gradient, a reverse flow can take place and the flow in the boundary layers can separate. This phenomenon is associated with the formation of vortices.

In two dimensional flows separation and reattachment points are defined by Prandtl's criterion, which states that the wall shear stress τ_w is zero at these points. This criterion is not appropriate for three dimensional separated flows for which another method has to be found.

The use of the *Theory of Critical Points* introduced by Legendre (1956) was suggested to describe the separation of three dimensional boundary layers (Lighthill (1963)).

Critical points are singularities in the flow field where the velocity vanishes and the direction of the vector quantity under consideration is undetermined. These singular points can be classified into two main categories: nodes and saddle points.

Nodes include nodal points and foci. A nodal point is a point common to an infinite number of streamlines. At this point all streamlines except one are tangential to a single line. Degenerated nodal points exist where every streamline has a distinct tangent and they act as sources or sinks. A focus is characterized by the fact that all the trajectories spiral around it and no common tangent is present.

At a saddle point only two lines pass through the critical point whereas the other streamlines avoid the singular point and take on hyperbolic shape.

The three dimensional features of the flow can be deduced and interpreted by studying limiting streamlines' pattern and analyzing the flow topology, namely the distribution, the type and the relations of critical points (Délery (2001), Tobak and Peake (1982)). Limiting streamlines are so called because they are streamlines on a surface whose distance from a no-slip wall tends to zero. The wall streamlines permit to identify separation and reattachment lines in three dimensional flows. In separation processes the limiting streamlines tend to converge towards a common line named separation line. The inverse of a line of separation is a line of reattachment characterized by the fact that the streamlines diverge from it. Therefore, Prandtl's separation criterion ($\tau_w = 0$) valid for two dimensional flows is replaced by a criterion of convergence and divergence of wall streamlines to and from a critical line.

In the following, the basic concepts of the theory of critical points and limiting streamlines' pattern are employed to describe the three dimensional separated flow oc-

curring behind symmetric sudden expansions. All the results are obtained for a fixed expansion ratio of 4.

First the evolution of the topology of the hydrodynamic flow with increasing the Reynolds number is analyzed together with the main 3D flow structures. Afterwards, details of the flow at $Re = 100$ are given since it is chosen as the reference case for the study of the effects of a magnetic field on the configuration of the flow in sudden expansions. In Section 4.3 the answer of the reference asymmetric hydrodynamic flow to the application of a uniform magnetic field is studied by raising progressively the imposed field while the Reynolds number remains constant. The last part of the chapter consists of a parametric study in which the strength of inertia forces with respect to electromagnetic forces is varied by choosing various interaction parameters N in the case of flow under a constant magnetic field ($Ha = const$).

4.2 3D hydrodynamic flow

In order to generate grid-independent solutions for the three dimensional flow, initially a scan of a range of Reynolds number ($5 \leqslant Re \leqslant 150$) has been performed using a relatively coarse grid and successively the grid has been refined. Calculations on the fine grid have been performed for Reynolds numbers around some noticeable values, namely the critical Reynolds number corresponding to the symmetry-breaking bifurcation and the Reynolds number defining the appearance of the secondary separated flow downstream of the small bubble.

Considering that in the case in which the flow is not normal to the faces of the grid elements, for instance in recirculation regions, numerical diffusion can limit the accuracy of the solution, two different advection schemes have been used and compared. The effect of numerical diffusion consists in damping the flow features owing to the presence of a numerical viscosity that arises from the discrete approximation to the advection term in the momentum equation.

First the first order upwind scheme has been employed together with a progressive mesh refinement and then a second order scheme has been selected to find out the importance of the numerical diffusion on the accuracy of the solution.

Let us consider as samples a coarse and a fine grid. By comparing the results on the two grids for a constant Reynolds number using the upwind scheme, the difference in the reattachment length is about 10 %. This deviation is reduced to $1 \div 2$ % by using the second order accurate discretisation.

The comparison between the solutions on the fine grid obtained by using the two advection schemes shows a difference in the recirculation length of 20 % for the flow at Reynolds number equal to 100. This deviation reduces for smaller Reynolds number (4 % for $Re = 10$).

The results described in the following are obtained by employing the second order advection scheme and the fine grid.

To achieve a good understanding of the three dimensional flow features, a topological study of limiting streamlines is performed. The data used for drawing the wall streamlines are those at the first interior plane of nodes adjacent to the corresponding no-slip

boundary. The locations of the critical points are found as the positions where the two velocity components on the plane of interest are zero simultaneously.

The analysis shows that at low Reynolds number the flow is symmetric with respect to the plane $y = 0$ and the recirculations increase in size with raising the Reynolds number. It is worth noticing that the flow remains symmetric with respect to the plane $z = 0$ for all the Reynolds numbers investigated. Beyond a critical value of the governing dimensionless group ($Re_c \simeq 27$) the flow becomes asymmetric. A further increase of the Reynolds number ($Re > 36$) leads to the appearance of secondary flow. Differences are observed between the development of the recirculations on the side wall and on the middle plane of the duct as described in the following.

Fig.19 shows the limiting streamlines on the side wall of the channel for the symmetric flow at $Re = 10$ and $Re = 20$. The red lines indicate the points on the wall where the axial velocity component changes its sign or becomes zero. They pass through the critical points and they give a good indication of the reattachment length of the separation region.

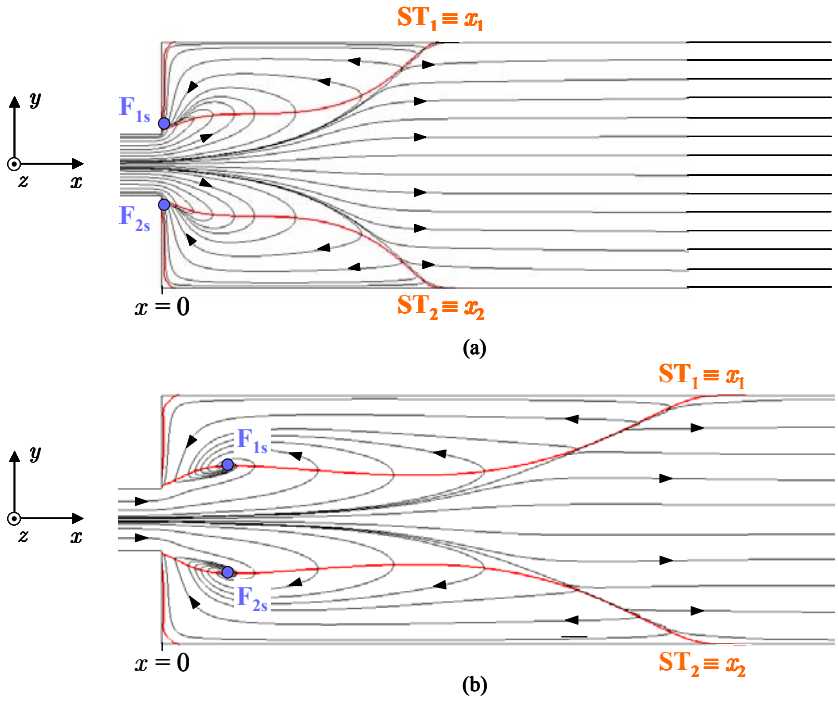

Figure 19: Limiting streamlines on the lateral wall of the duct for the flow at $Re = 10$ (a) and $Re = 20$ (b). The red lines indicate the locations where the u-velocity component is zero. ST designates the stagnation points and F_s the foci on the side wall.

The topology of these flows on the lateral wall of the channel is characterized by two half saddle points (stagnation points, ST_1 and ST_2), which correspond to the reattachment locations of the primary recirculation zone on the upper and lower wall of the duct and by two foci (F_{1s}, F_{2s}), which the streamlines spiral on. A wall reattachment line can be identified as the line, which the limiting streamlines diverge from. It is the trace on the wall of a surface that separates the back flow region from the rest of the flow. With rising the Reynolds number, the foci move downstream and the recirculations become

longer as shown in Fig.19(b).

The foci are the traces on the side wall of a 3D spiralling path that transports the fluid from the lateral walls to the middle plane ($z = 0$) of the duct. They are associated with an isolated line originating from the foci themselves, which the other streamlines spiral around taking on helical shape. This line will be referred to as vortex core line. Owing to the symmetry of the flow with respect to the planes $y = 0$ and $z = 0$, in the following the 3D flow structures are shown only in a quarter of the channel.

A comprehensive picture of the three dimensionality of the flow at $Re = 10$ is given in Fig.20. Here particles are released at the inlet plane at various distances from the side wall. The red line indicates the vortex core line defined above. The top view (Fig.20(b)) shows that the flow coming from points very close to the side wall, marked by the blue and the black lines, enter the recirculation and swirl around the vortex core line reaching the middle plane of the duct. Particles injected further from the lateral wall (green line) turn only few times around the vortex line and they only approach the symmetry plane $z = 0$. At a certain distance from the side walls the fluid flows directly downstream and it is no longer trapped into the vortex. More in details, all the particles inserted in the range $-0.65 < z < 0.65$ do not contribute to the recirculation.

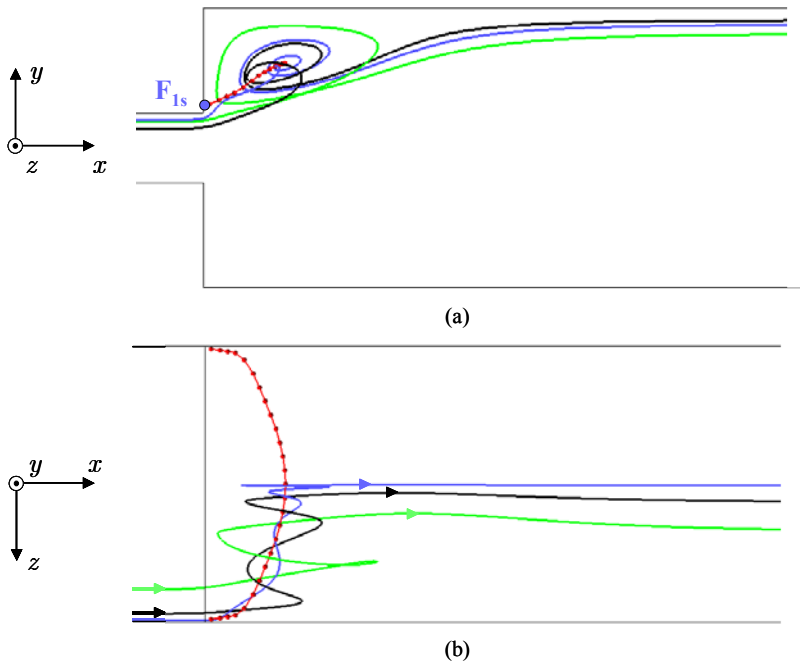

Figure 20: Lateral (a) and top (b) view of 3D streamlines for the flow at $Re = 10$. The red line is the vortex core line whose starting point on the side wall is the focus F_{1s}.

By increasing the Reynolds number ($Re > 27$) the flow becomes asymmetric and the flow topology on the side wall changes as shown in Fig.21(a).

As for the symmetric flow, two foci (F_{1s}, F_{2s}), trace on the lateral wall of the vortical structures, and two reattachment points (ST_1, ST_2) are present. Two additional critical points appear on the side wall: a node N_{3s} that feeds the recirculations and a saddle point SD_{1s} that separates the two bubbles. These new points disappear at some distance

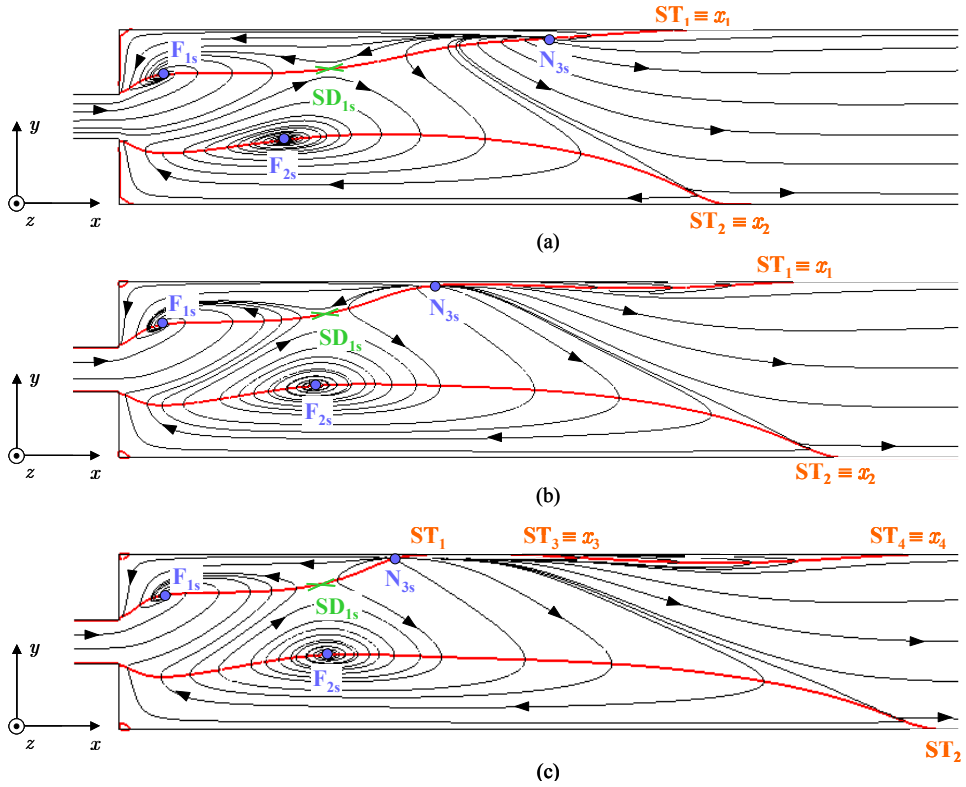

Figure 21: Limiting streamlines on the side wall for the flow at $Re = 30$ (a), $Re = 35$ (b) and $Re = 40$ (c).

from the side walls where the flow pattern resembles the 2D flow. As a result of this configuration, the reattachment lengths on the lateral wall of the recirculations forming the primary separation zone remain comparable by increasing the Reynolds number ($x_1 \simeq x_2$).

This can be explained considering that by raising further the Reynolds number the longitudinal distance between the node N_{3s} and the stagnation point ST_1 increases since the two singularities move in opposite direction as shown in Fig.21(b) for the flow at $Re = 35$.

When the secondary flow occurs ($Re > 36$), the streamlines touch the upper wall in a point very close to the node N_{3s} giving rise to two singularities indicated by ST_1 and ST_3 in Fig.21(c). One of these points is the reattachment position of the small bubble (ST_1) and the other one is the separation point of the additional recirculation (ST_3). Therefore a jump in the reattachment length on the side wall (ST_1) is observed and it is associated with the appearance of the secondary flow. This can be seen in Fig.22 where reattachment and separation points both on the side wall and on the symmetry plane $z = 0$ are plotted as a function of Reynolds number. In the range $25 < Re < 36$ the reattachment points x_1 and x_2 on the lateral wall remain very close till the secondary flow appears. Scanning the axial location of the node N_{3s} in this range of Reynolds number, it is found that its position changes following well the black dashed curve drawn in Fig.22(a). By replacing the previously identified values of x_1 with this new curve a bifurcation diagram similar to that for the points on the middle plane is

obtained.

The additional separation zone included between x_3 and x_4 is present only in a limited spanwise range close to the side walls and does not extend to the duct midplane. With increasing Reynolds number it moves downstream as suggested by the rising of the distance between the end of the small recirculation (x_1) and the separation point of the secondary flow (x_3).

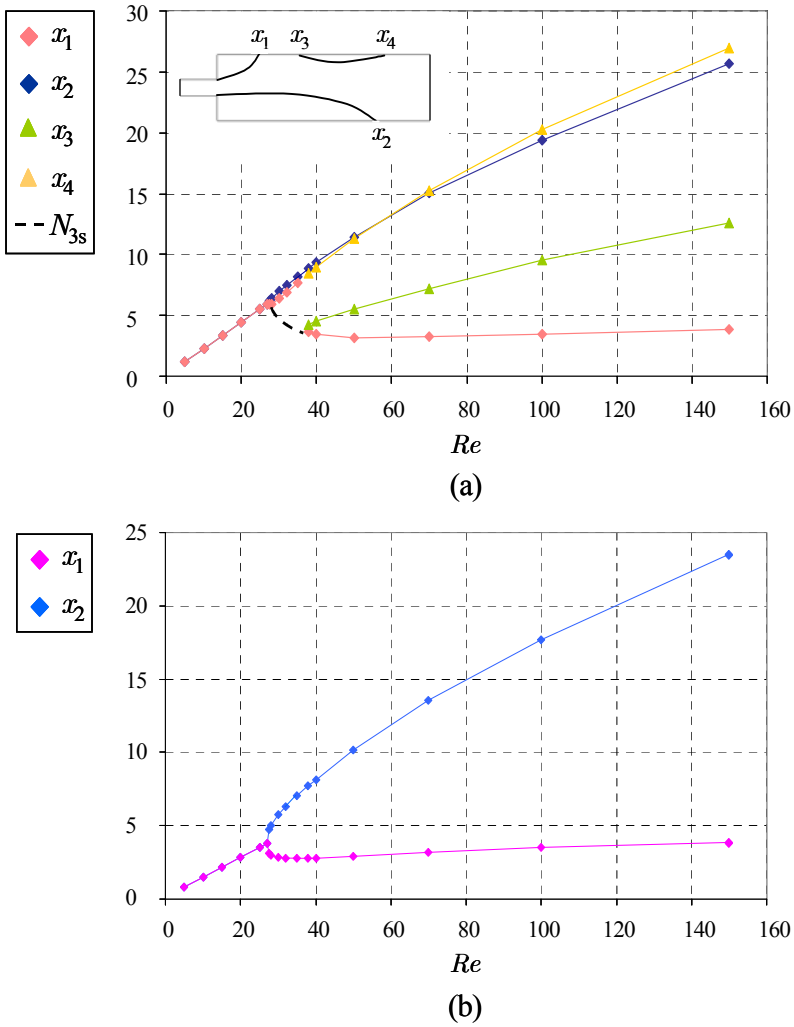

Figure 22: Locations of reattachment and separation points of recirculations on the side wall (a) and on the symmetry plane $z = 0$ (b) as a function of Reynolds number. The black dashed line (a) indicates the axial position of the node N_{3s}.

The previous observations are summarized in Fig.23 where the lines along which the axial velocity component u vanishes are plotted on the top wall of the duct and compared for various Reynolds numbers. Here the modifications leading to the appearance of the secondary recirculation are clearly displayed starting from the symmetric flow at $Re = 25$.

Regarding the evolution of the recirculation lengths on the symmetry plane $z = 0$ (Fig.22(b)), when the flow is symmetric with respect to the plane $y = 0$, the extent of

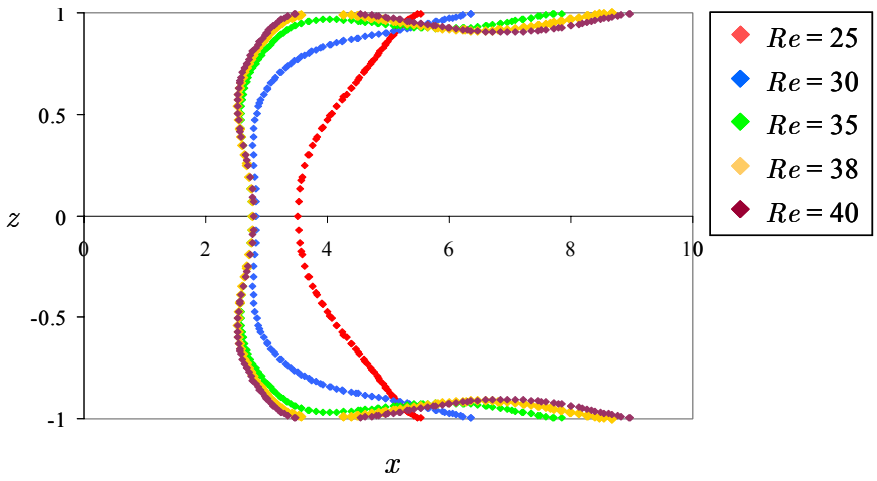

Figure 23: Lines along which the axial component of the velocity vanishes, plotted on the top wall for various Reynolds numbers Re. At $Re = 25$ the flow is still symmetric.

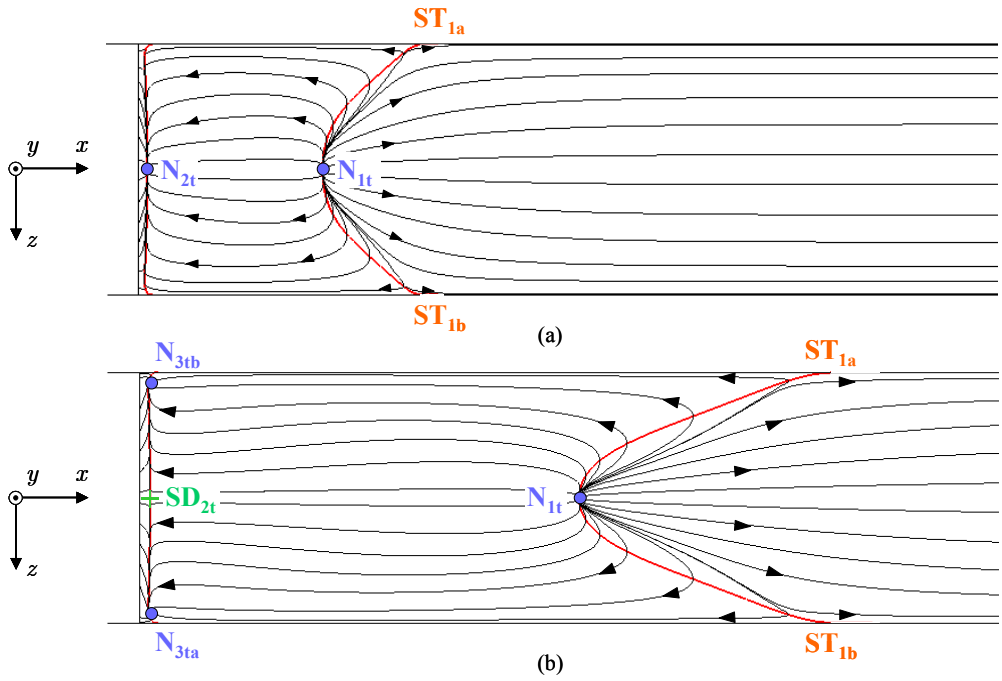

Figure 24: Limiting streamlines on the upper wall of the channel for the symmetric flows at $Re = 10$ (a) and $Re = 25$ (b). The topology close to the reattachment line remains the same while it changes near the expansion along the separation line.

the back flow region is smaller than that on the side wall. After the onset of the asymmetry, by increasing the supercritical Reynolds number, one of the recirculations becomes smaller and smaller (x_1) and finally remains almost constant whereas the other one (x_2) grows progressively with Reynolds number. The bifurcation diagram is analogous to that for the 2D flow.

It is worth also describing the changes of the flow topology on the top of the channel with raising Reynolds number. In Fig.24 the limiting streamlines are depicted on the upper wall of the duct for the symmetric flows at $Re = 10$ and $Re = 25$.

The topology of the flow at $Re = 10$ is characterized by two nodes N_{1t} and N_{2t} that act as a source and as a sink respectively. The node N_{1t} lies on the reattachment line that separates the recirculation region from the downstream flow and the node N_{2t} on a separation line. For higher Reynolds number near the corners, on the separation line two symmetric sinks are observed together with two saddle points that separates the flow entering the central node N_{2t} from that moving into the lateral sinks. By increasing the Reynolds number, the nodes at the corners remain approximately in the same position while the saddle points move towards the middle plane till they join together creating a single saddle point SD_{2t} as shown in Fig.24(b) for $Re = 25$.

Above the symmetry breaking Reynolds number a new topological structure occurs on the top wall as depicted in Fig.25. The node that was present on the reattachment line splits into two nodes of reattachment N_{1ta} and N_{1tb} and a new saddle point SD_{1t} appears in between. With increasing Reynolds number, these two nodes move towards the side walls. Limiting streamlines emerging from the nodes are prevented from crossing the center line $z = 0$ by the presence of a separation line that connects the two saddle points SD_{1t} and SD_{2t}.

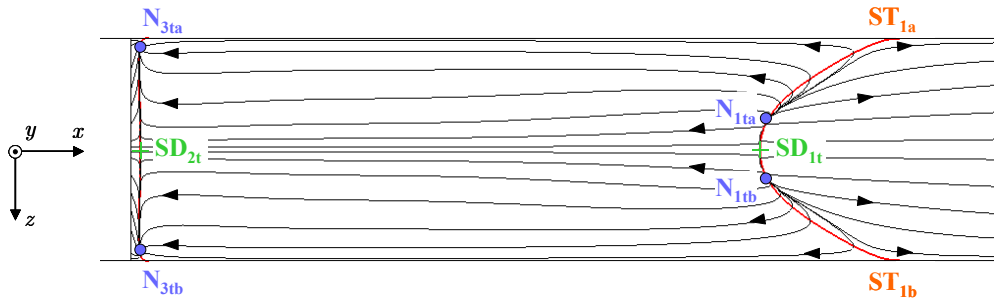

Figure 25: Limiting streamlines on the top of the duct for $Re = 30$. Downstream, along the reattachment line new topological features are present: two reattachment nodes acting as sources and a saddle point.

Concerning the topology of the flow on the bottom of the channel where the long recirculation develops when the asymmetry occurs, the flow structure is characterized by two saddle points separating two families of streamlines that originate from the nodes on the reattachment line similarly to the configuration on the top wall shown in Fig.25 for the flow at $Re = 30$. This topology is preserved while increasing the Reynolds number.

The last part of this section is dedicated to the description of the main characteristics of the flow at $Re = 100$. As mentioned before, this flow is assumed as the reference hydrodynamic case and it will be compared with the magnetohydrodynamic flow at the

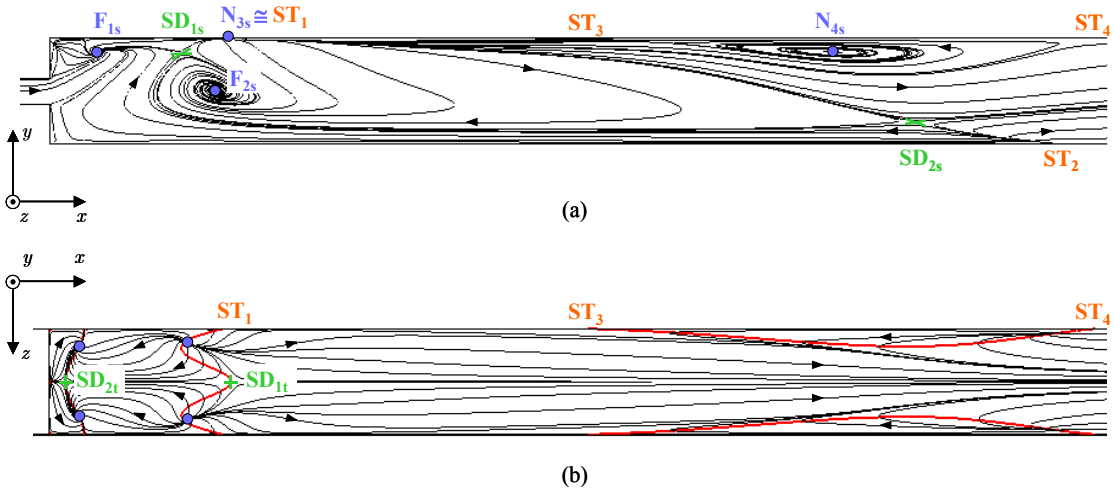

Figure 26: Limiting streamlines on the side wall (a) and on the top (b) of the duct for the flow at $Re = 100$.

same Reynolds number for understanding the effects of the magnetic field on the size and the occurrence of the separation regions behind sudden expansions.

Let us consider the wall streamlines plotted on the side wall of the duct (Fig.26(a)). The complexity of the flow is made visible by the increased number of critical points describing the kinematic aspects of the streamlines. The topological analysis reveals that, after the occurrence of the secondary recirculation, the node N_{3s} behind the small recirculation almost coincide with the half saddle point that identifies the reattachment location of the reverse flow on the top of the duct. Fig. 26(b) shows that the secondary recirculation does not extend throughout the channel width but is restricted to the sides.

Moreover, additional flow patterns develop in front of the primary vortex where the flow moves preferentially towards the side walls and strong transverse velocities are found. The foci F_{1s} and F_{2s} on the lateral wall are the starting points of the centerline of the main vortical structures. The swirling motions are depicted in Fig.27. The red lines are the vortex core lines.

The previous results highlight the importance of the vortex core line to visualize the 3D flow structures. Therefore to summarize the effects of the rise of Reynolds number on the flow configuration, the core line of the long primary recirculation is shown in Fig.28 for various Reynolds numbers. The center line of the small separation zone is not plotted because its behavior is similar to that of the core line characterizing the symmetric flow with the only difference that the line is slightly stretched downstream owing to the higher velocity. With increasing the Reynolds number the core line of the long vortex elongates and the focus F_{2s} on the side wall shifts downstream.

Calculations have been performed also for the 2D flow and the computed value of Reynolds number corresponding to the symmetry-breaking bifurcation point ($Re_c \cong 18$) agrees well with the results in literature (Drikakis (1997), Revuelta (2005)). The comparison between the solutions for two dimensional and three dimensional flows confirms the stabilizing effect of the side wall observed by Cherdron et al. (1978) and Schreck and Schäfer (2000), which results in a higher critical Reynolds number for the three dimensional flow.

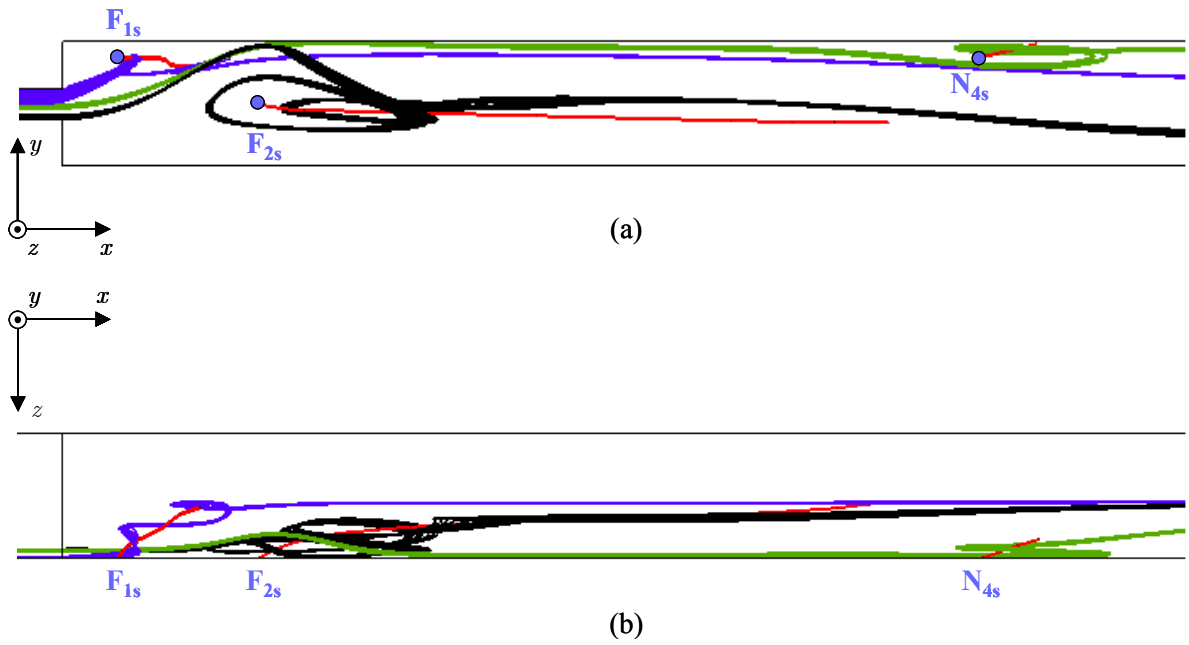

Figure 27: Lateral (a) and top (b) view of the 3D spiralling motion around the vortex core line (red lines) for $Re = 100$. The nodes on the side wall are the origins of the vortex core lines.

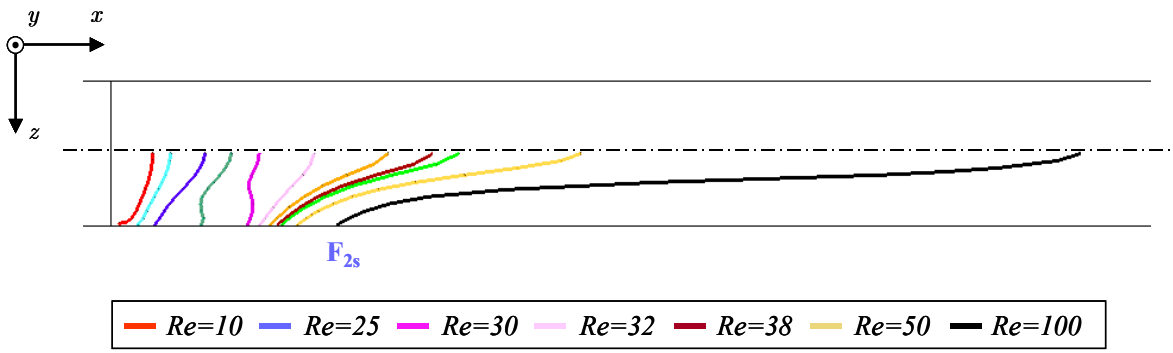

Figure 28: Top view of the duct showing the vortex core lines of the long primary recirculation for various Reynolds numbers. In the legend only some Reynolds numbers are indicated.

4.3 3D MHD flow in sudden expansions

4.3.1 Variation of the applied magnetic field at constant flow rate

The three-dimensional MHD flow in rectangular ducts with sudden expansion is studied to investigate how an applied magnetic field affects an asymmetric hydrodynamic flow at $Re = 100$. The Hartmann number Ha is progressively increased while keeping the Reynolds number constant. Following the same approach used for the analysis of the hydrodynamic flow (Section 4.2) a topological study is carried out. The investigation of critical points and limiting streamlines allows to reconstruct the 3D features of the MHD flow.

Fig.29 shows the limiting streamlines on the side wall of the channel for the flow at various Hartmann numbers starting from the case without magnetic field ($Ha = 0$). The red points indicate the foci, which are the traces on the lateral wall of the vortex core lines. These latter represent the centerlines of the vortical structures that form behind the expansion. The position of these lines will be later compared for different Hartmann numbers and used to explain how the magnetic field affects the size of the recirculations.

The region of reverse flow is limited downstream by a reattachment line made visible by the fact that the streamlines diverge from it. This line is indicated for the flow at $Ha = 30$ by the green curve. The red line, drawn here only for $Ha = 5$, corresponds to the points where the axial velocity component u vanishes. It provides an effective mean to visualize the longitudinal extent of the separation zone. The point where this line touches the wall perpendicular to the magnetic field, marked by the blue dot, is the reattachment point of the recirculation on the side wall.

For the hydrodynamic case ($Ha = 0$) the flow topology is quite complex (refer to Section 4.2). The flow is asymmetric and a secondary recirculation develops downstream of the small primary separation region on the top of the duct. By applying the magnetic field the length of the back flow region starts reducing. For $Ha = 3$ only a small trace of the secondary flow remains and the size of the recirculation is already reduced by 20% compared with the hydrodynamic case. By increasing the Hartmann number the separation area shrinks further. The topology of the MHD flow at $Ha > 4$ resembles that of the symmetric hydrodynamic flow for $Re \leqslant 25$.

The separation zones occur due to the effect of viscous forces and the presence of an adverse pressure gradient that retard the flow near the wall of the duct. As a result the fluid is forced to move in direction opposite to the main flow. In addition, when the interaction parameter N is small inertia forces are strong and oppose to the modifications of velocity profile. Therefore, some distance from the expansion is required before the fluid can "fill" all the large duct, reaching the Hartmann walls.

In Fig.30 the lines where the velocity component u becomes zero on a plane adjacent to the side wall are compared for various Hartmann numbers. They clearly show that the magnetic field tends to reduce the axial size of the recirculations. In the figure x_1 indicates the position of the reattachment point. The dependence on the interaction parameter of the reattachment length is shown in Fig.31. A linear approximation of the numerical results in logarithmic scale shows that for $Ha \geqslant 50$ the length x_1 is proportional to $N^{-0.3}$. This could be an indication that the side layers are dominated by an inertia-electromagnetic balance in this range of parameters.

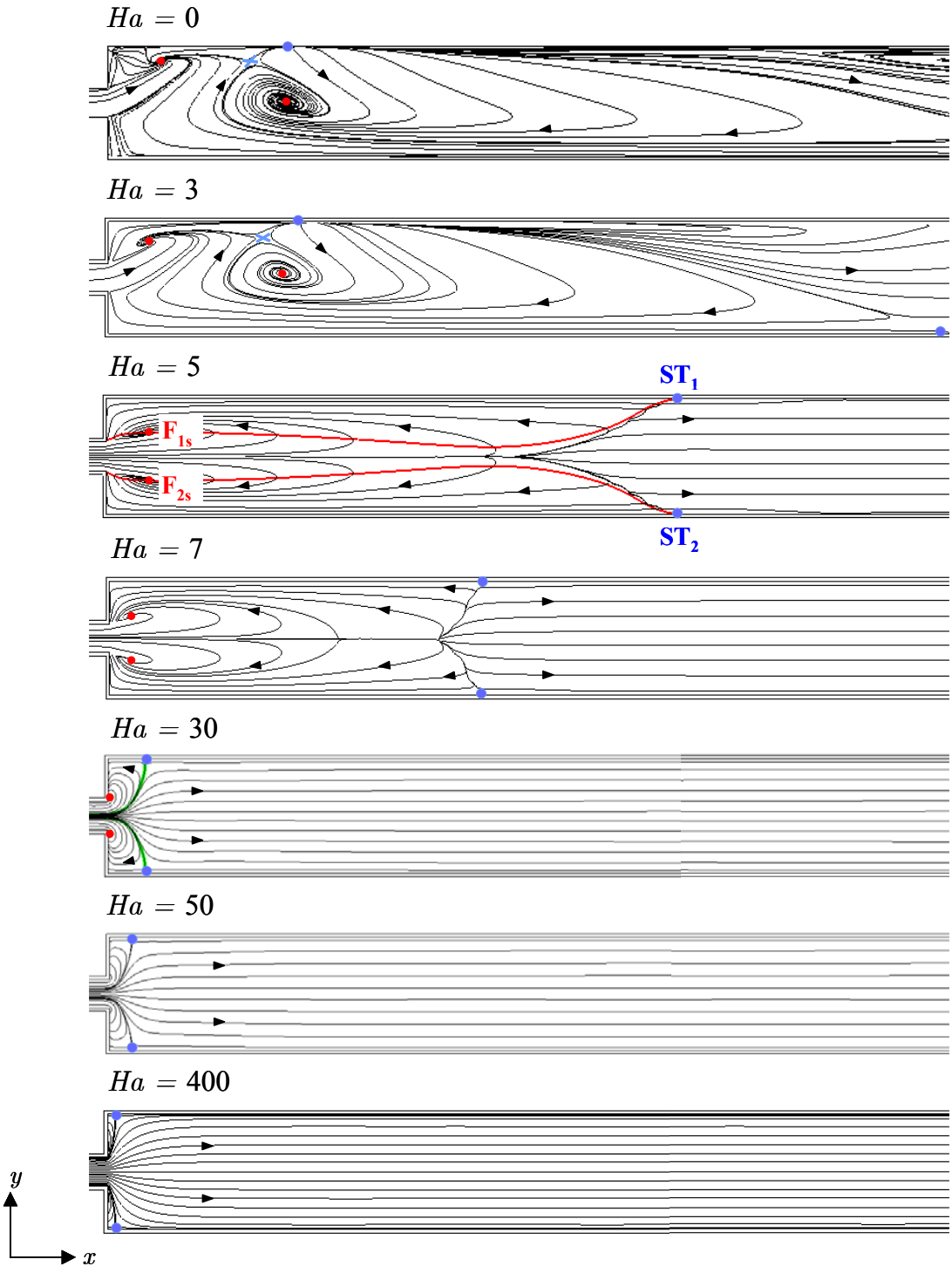

Figure 29: Limiting velocity streamlines on the side wall parallel to **B** for $c = 0.1$, $Re = 100$ and various Hartmann numbers Ha. The red points are the foci, traces on the side wall of vortical structures, and the blue dots on the Hartmann walls are the reattachment points. Along the red line, plotted for $Ha = 5$, the axial velocity is zero. The green line drawn for $Ha = 30$ indicates the reattachment line.

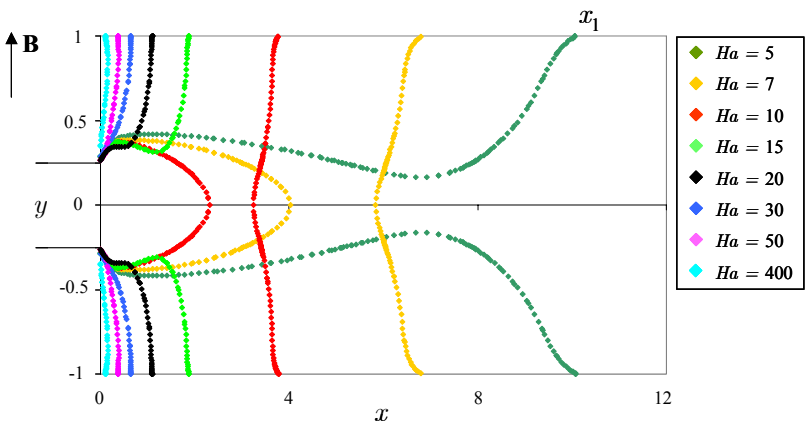

Figure 30: Lines along which the axial velocity component is zero, plotted on the side wall of the duct for several Hartmann numbers Ha and $Re = 100$. x_1 indicates the reattachment point.

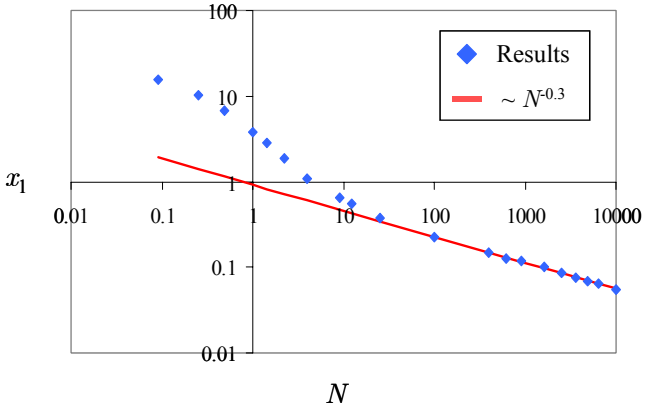

Figure 31: Reattachment length x_1 at the side walls as a function of the interaction parameter N in logarithmic scale for $Re = 100$. The curve that fits well the results is proportional to $N^{-0.3}$.

In Fig.32 limiting streamlines are drawn on the wall perpendicular to the magnetic field for several Hartmann numbers. For the asymmetric flow ($Ha = 3$) the topology on the bottom of the duct is considered. On this wall the long primary recirculation is present. It is worthwhile to remark the presence of additional 3D flow patterns immediately behind the expansion, in front of the primary recirculation, for the flow at $Ha = 0$. For $Ha = 5$ this region is still present and it is very small as indicated by the red line where $u = 0$, but at higher Hartmann numbers it disappears.

The flow topology on the Hartmann wall for moderate Hartmann numbers is characterized by two nodes that act as sources (red dots) and by a node close to the expansion that behaves as a sink. The border of the region of reverse flow is indicated by the reattachment line that passes through these sources and through the saddle point located on the symmetry plane. By rising the Hartmann number the length of the zone of back flow reduces, the two sources move closer to the expansion and to the side walls. The saddle

point approaches the sink till both disappear. Later in this section an interpretation of these changes of the flow topology is given.

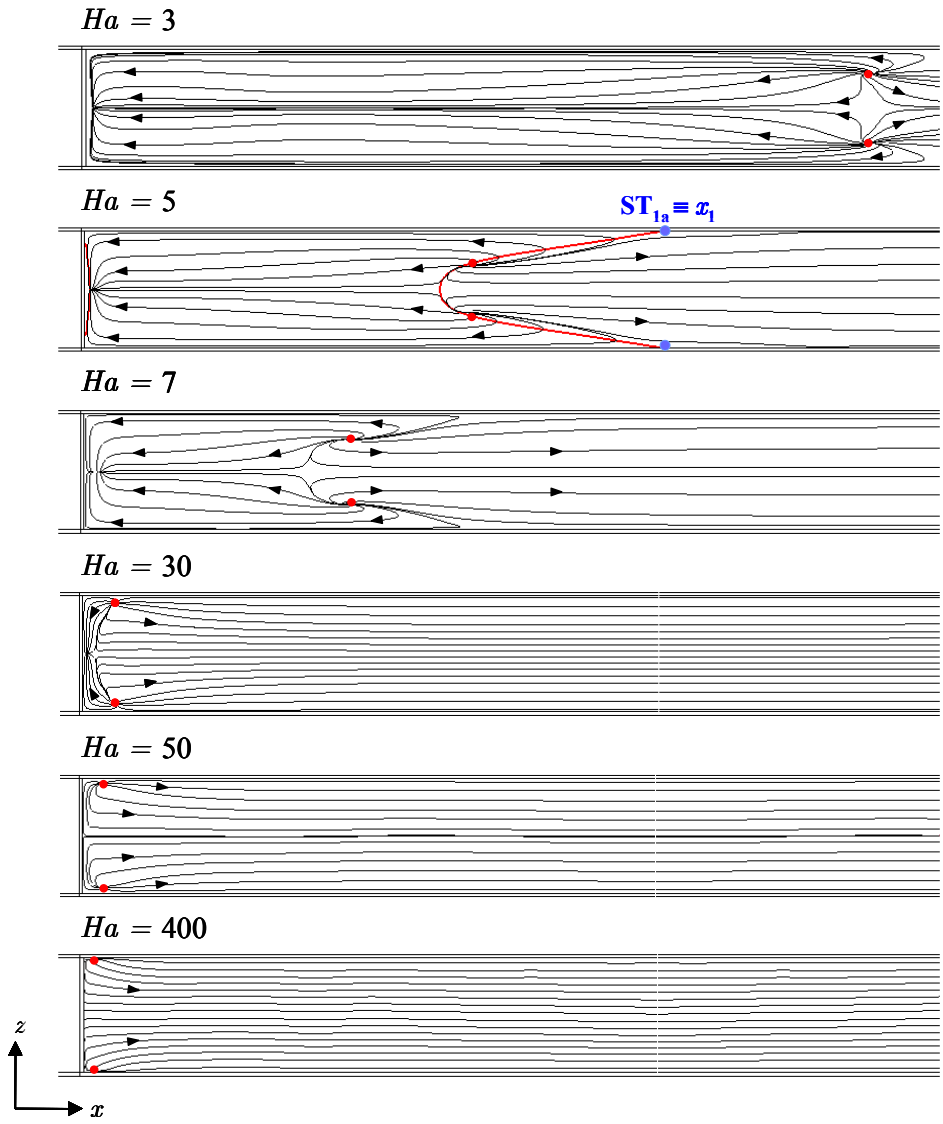

Figure 32: Limiting streamlines on the wall perpendicular to the magnetic field for various Hartmann numbers Ha and $Re = 100$. The red points are the nodes that behave as sources of streamlines.

The lines corresponding to the points where the axial velocity is zero are depicted on the wall perpendicular to the magnetic field for a range of Hartmann numbers (Fig.33). The locations indicated by x_1 and x_0 coincide with the reattachment points along the side wall and on the symmetry plane $z = 0$, respectively. The reattachment point x_0 is plotted as a function of the interaction parameter N in Fig.34. Interpolating the points in the logarithmic graph of Fig.34 the result shows that x_0 scales as N^{-1}. This result indicates that inertial effects in the core are damped out by the application of the magnetic field.

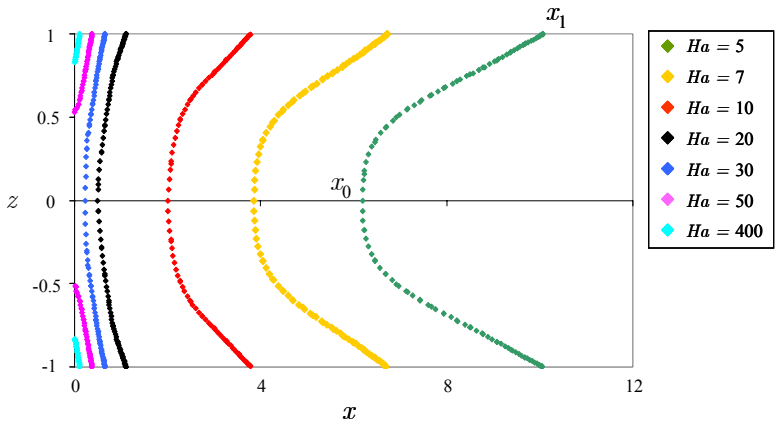

Figure 33: Lines along which the velocity component u vanishes, drawn on the Hartmann wall for various Hartmann numbers Ha and $Re = 100$. x_1 and x_0 are the reattachment points on the side wall and on the symmetry plane, respectively.

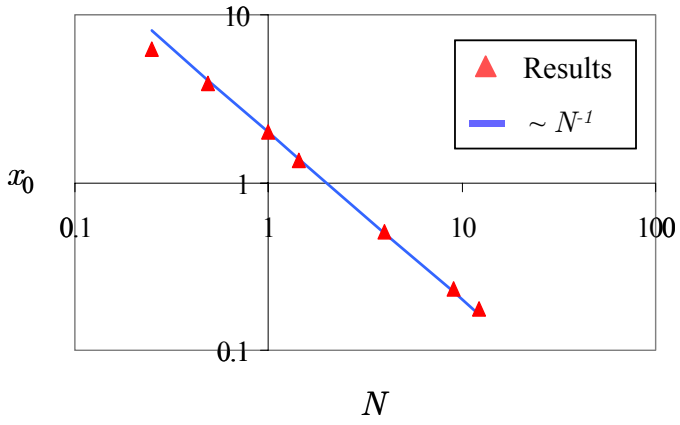

Figure 34: Reattachment point x_0 on the top of the duct along the symmetry plane $z = 0$ as a function of the interaction parameter N for $Re = 100$.

The effects of an applied magnetic field on the flow can be better understood analyzing the 3D velocity streamlines and by comparing the outcomes for the flow at moderate ($Ha = 30$) and large Hartmann number ($Ha = 700$).

In Fig.35 three-dimensional velocity streamlines are drawn for the flow at $Ha = 30$, $N = 9$ and $c = 0.1$. Fluid coming from the upstream core enters the large duct and flows in the downstream core (orange lines). Flow injected in the inlet duct in the side layer far from the Hartmann walls stays in this layer while moving downstream (blue path).

The topological study of the flow showed the existence on the side wall of two foci, which are the starting points on the lateral wall of the lines around which a spiralling motion develops. One vortex core line is indicated by the red curve in Fig.36. As a result of this swirling movement, the fluid is transferred from the upstream side layer towards the Hartmann walls and to the center of the large channel as shown in Fig.37.

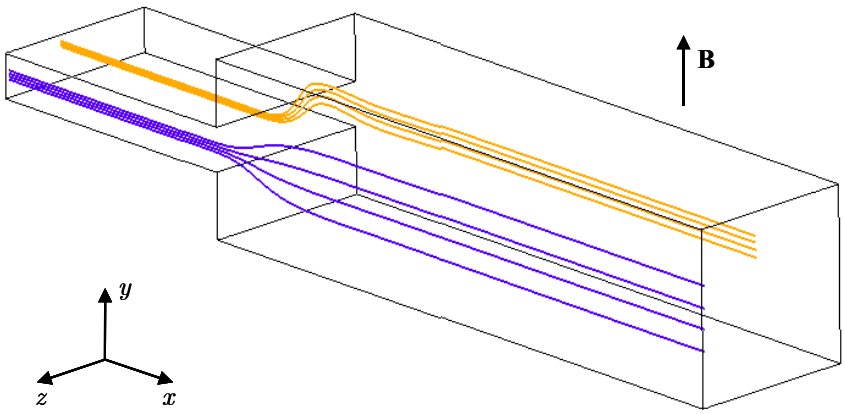

Figure 35: Flow at $Ha = 30$, $N = 9$ ($Re = 100$) and $c = 0.1$. Flow from the upstream core enters the downstream core (orange path) and flow in the side layer, far from Hartmann walls, stays in this layers moving downstream (blu lines).

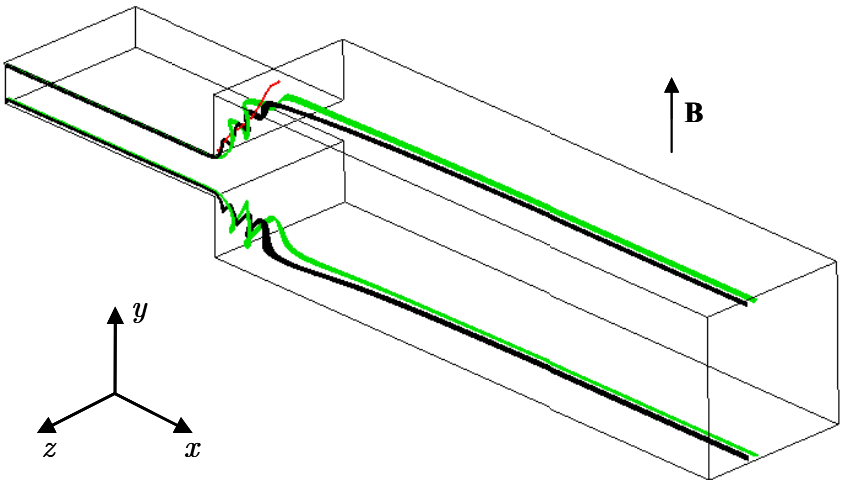

Figure 36: Streamlines for the flow at $Ha = 30$, $N = 9$ ($Re = 100$) and $c = 0.1$. The red line is the vortex core line.

Moving further from the side walls the flow still contribute to the formation of vortices but the diameter of the spiralling path increases.

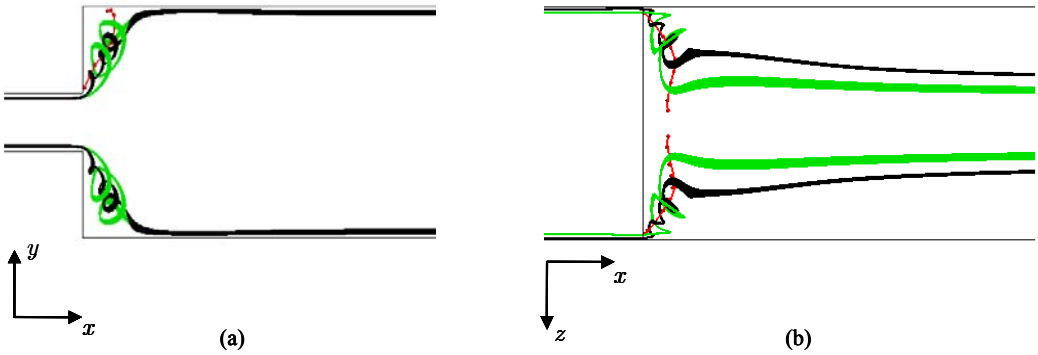

Figure 37: 3D streamlines for the flow at $Ha = 30$, $N = 9$ ($Re = 100$) and $c = 0.1$. The lateral view shows the upward motion (a) and the top view the movement to the middle of the duct (b). The red line is the centre of the vortical structures.

Another typical flow path exists, which is of particular interest since, with few modifications, it appears also for the flow at high Hartmann numbers when the vortical motion disappears, suppressed by the action of the electromagnetic forces. In Fig.38 this new flow pattern is depicted. The flow coming from the side layer goes upward to the Hartmann wall and then backward towards the vertical wall of the expansion. Moving along this wall the fluid approaches the symmetry plane at $z = 0$ by flowing in directions perpendicular to the magnetic field and to the main flow. Here the flow describes a V-shaped trajectory, which defines the region in which the spiralling motion takes place as shown in Fig.38 by the position of the vortex core line.

The knowledge of the main 3D flow paths, which characterize the velocity field of the flow at moderate Hartmann numbers, allows to explain better the meaning of the critical points previously identified on the Hartmann wall. In Fig.39 the red dot is the node that acts as a source. The fluid entering this node can flow in various directions. The green point close to the expansion wall is the sink located on the symmetry plane at $z = 0$. The saddle point that bounds the back flow region is marked by a cross.

The limiting streamlines on the wall perpendicular to the magnetic field showed that for high Hartmann numbers the sink and the saddle point on the symmetry plane disappear. This indicates that the V-shaped path vanishes and the vortical structure does not extent any more throughout the width of the channel. The vortical regions start shrinking also in the transverse direction z. For sufficiently high Hartmann number the swirling motion is suppressed by the electromagnetic forces. As a consequence, the vortex line can be depicted only for the flow at moderate Hartmann number. Fig.40 shows how the position of this line changes by rising the applied magnetic field . The lateral view indicates that the magnetic field tends to damp out the vortices in the axial direction. The focus F_1 on the symmetry plane moves towards the Hartmann walls and closer to the expansion.

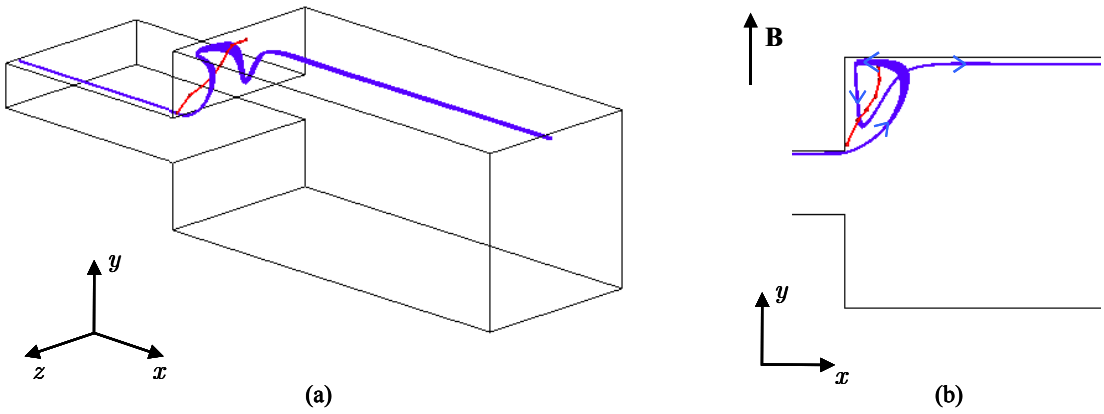

Figure 38: 3D flow path for the flow at $Ha = 30$, $N = 9$ and $c = 0.1$. The red line is the vortex core line.

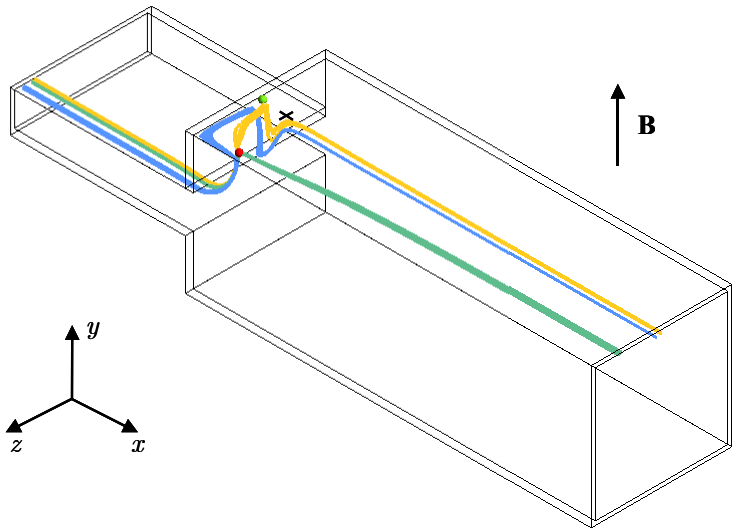

Figure 39: Flow at $Ha = 30$, $N = 9$ and $c = 0.1$. The streamlines show the meaning of the critical points characterizing the flow topology on the Hartmann wall. The red point is the source, the green one is the sink and the cross is the saddle point.

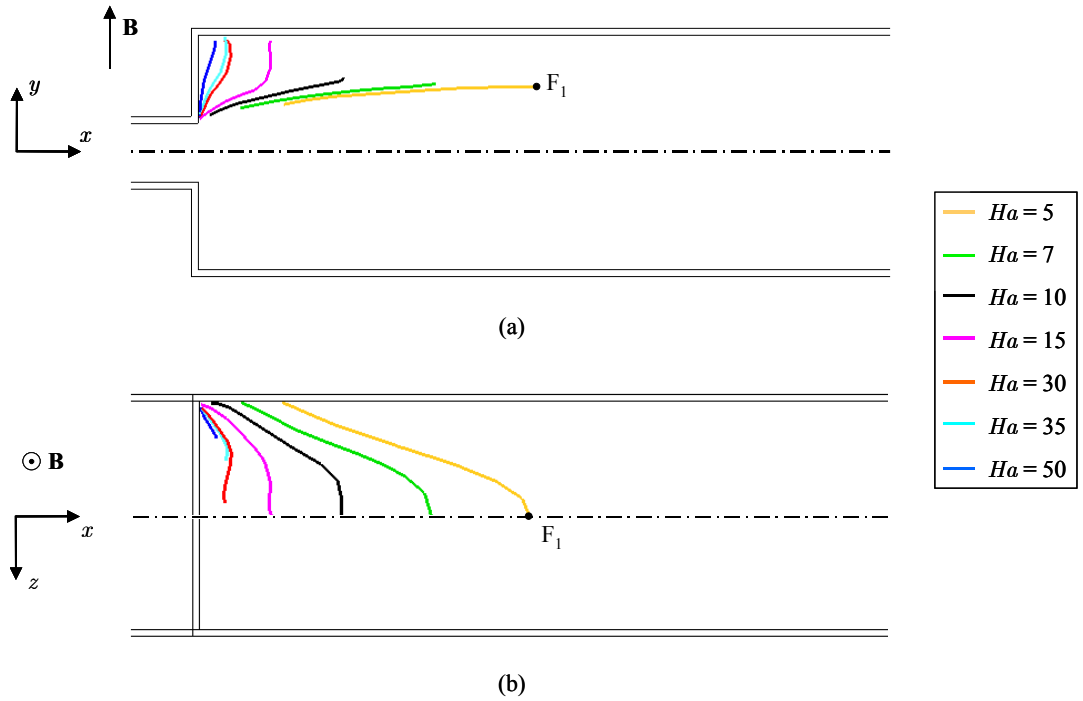

Figure 40: Vortex core lines for several Hartmann numbers and $Re = 100$. F_1 is the trace of the vortex core line on the symmetry plane $z = 0$.

For large enough Hartmann numbers the size of the vortices, indicated by the extent of the core line, reduces also in the transverse direction z until the swirl vanishes (Fig.40(b)). This effect can be also visualized by drawing the velocity streamlines on the symmetry plane $z = 0$ (Fig.41). The dashed line at $x = 1$ is plotted as a reference. By rising the Hartmann number above $Ha = 20$ the focus, trace of the vortex line, is not present any more and the size of the V-shaped path decreases progressively. For high Hartmann numbers the streamlines follow perfectly the contour of the large duct.

This phenomenon can be explained considering that for moderate Hartmann number the interaction parameter N is relatively small. Therefore inertia is stronger than the electromagnetic forces and prevents the fluid from following the shape of the duct. The velocity profile is only slightly affected by the magnetic field and the initially fully developed velocity profile propagates across the expansion without strong modifications. With rising the Hartmann number electromagnetic forces increases and inertia effects become weaker. As a result the velocity profile is strongly affected by the applied magnetic field and flow patterns that deviate greatly from usual hydrodynamic flow are observed.

In order to understand these modifications of the velocity distribution, a description of the fundamental 3D MHD phenomena occurring in sudden expansions is required.

Due to the reduction of the axial component of the velocity from the small to the large duct, the transverse potential difference is strongly reduced and as a consequence an axial potential difference occurs, which drives additional currents inside the fluid

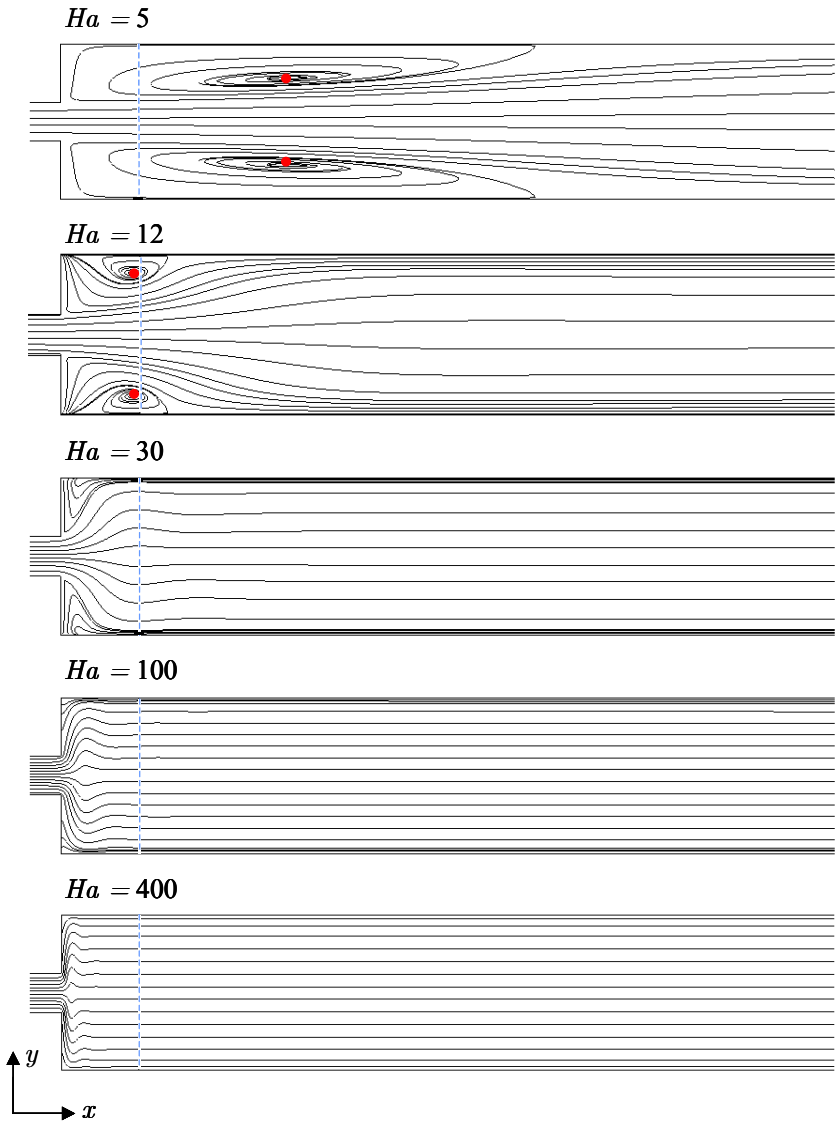

Figure 41: Streamlines on the plane $z = 0$ for various Hartmann numbers and $Re = 100$.

along the walls parallel to the magnetic field. These currents close through the width of the channel. In Fig.42 a schematic representation of the current distribution on the plane $y = 0$ is shown.

Both upstream and downstream at some distance from the expansion where the flow is fully developed, 2D currents flow in the positive transverse direction. In the small duct the induced three-dimensional currents j_{3D} have the same direction as those in the fully developed region and they cause a Lorentz force that opposes the flow. As a consequence part of the mechanical energy is converted into electric energy and this yields an additional contribution to the pressure gradient.

Behind the expansion the 3D currents flow in opposite direction compared to the 2D currents and if they are sufficiently high a net negative transverse current appears, which creates a positive electromagnetic force that accelerates the flow. Part of the electric

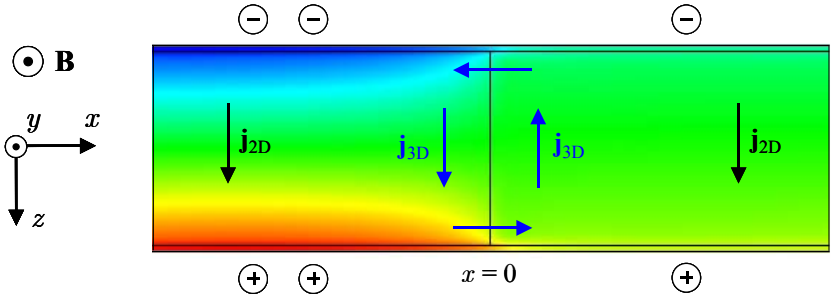

Figure 42: Schematic representation of the distribution of fully developed and induced 3D currents on the plane $y = 0$. The contour plots indicate the potential distribution for $Ha = 700$ and $N = 4900$.

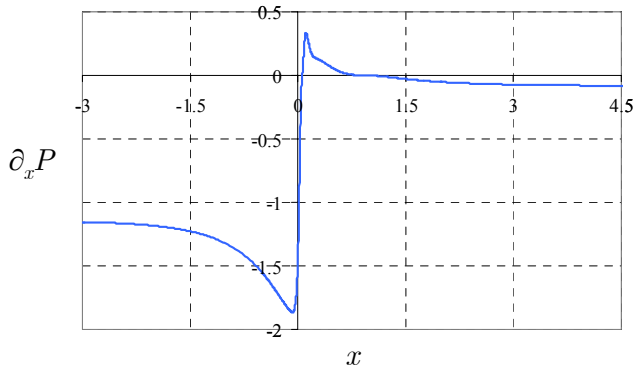

Figure 43: Axial component of pressure gradient along the axis of the duct for $Ha = 700$, $N = 4900$ and $c = 0.1$. The variable P is given by p/N where p is the pressure in the hydrodynamic scale.

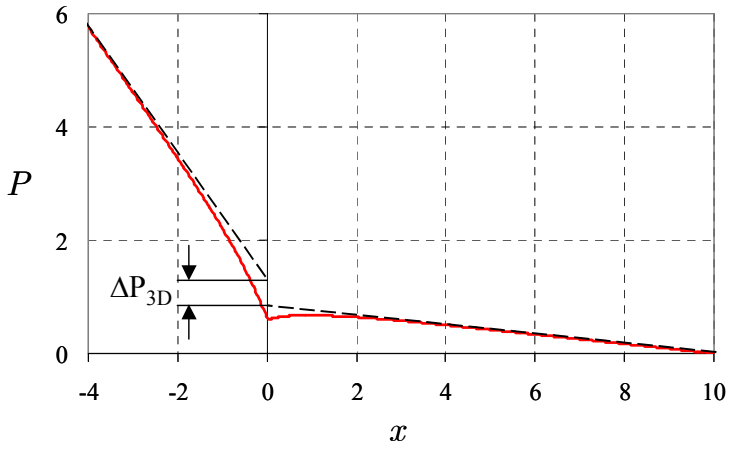

Figure 44: Pressure distribution along the axis of the duct for $Ha = 700$ and $N = 4900$. ΔP_{3D} indicates the additional pressure drop caused by the 3D current density. It is related to the pressure loss in hydrodynamic scale as $\Delta P_{3D} = \Delta p_{3D}/N$.

energy is transformed again into mechanical energy. This leads to some pressure recovery as can be seen from the pressure gradient plotted along the axis of the channel in Fig.43. The variable P indicated in the figure is given by the pressure in the hydrodynamic scale (as defined in Section 2.2) divided by the interaction parameter N. Owing to Joule dissipation an irreversible pressure drop remains.

This latter is indicated by ΔP_{3D} in Fig.44 where the pressure is plotted along the axis of the channel for $Ha = 700$ and $N = 4900$.

In Fig.45 the additional pressure drop Δp_{3D} caused by the 3D current density induced by the axial gradient of the electric potential is plotted as a function of the Hartmann number. For large Hartmann numbers the pressure loss increases as $Ha^{3/2}$.

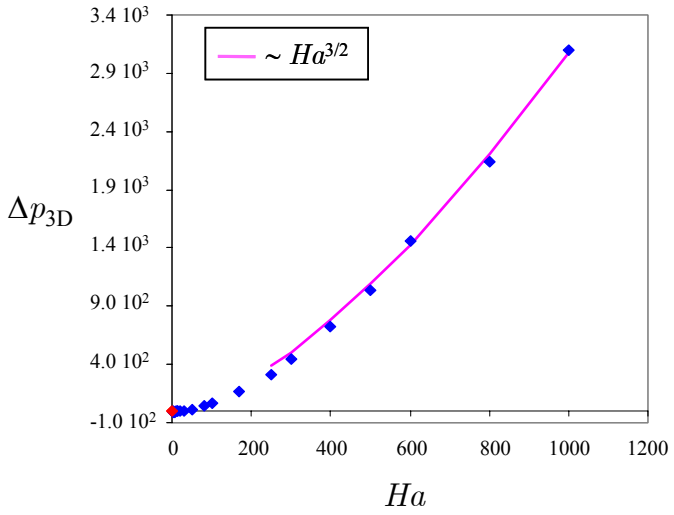

Figure 45: Pressure drop Δp_{3D} as a function of the Hartmann number. The continuos line is the best fit of the numerical results for high Hartmann numbers.

For $Ha < 10$ the pressure loss does not vary considerably and it approaches the hydrodynamic value as shown in Fig.46.

In Fig.47 the current component j_z is plotted along the streamwise direction on the symmetry plane $y = 0$. The closing of the current path and therefore the presence of this transverse component j_z of the current density has a profound influence on the development of the flow. Hence, the distance between the expansion ($x = 0$) and the point x_e in which j_z vanishes on the axis of the duct has been chosen as a measure for the thickness of the internal layer. In Fig.48 the thickness of the expansion layer is plotted as a function of the interaction parameter N. The results indicate that for large N it scales as $N^{-1/3}$. This is in agreement with the asymptotic analysis, which shows that when $N << Ha^{3/2}$ as in the case under study, in the internal layer the main force balance is established between inertial and electromagnetic forces and the thickness of the parallel layer is proportional to $N^{-1/3}$.

Let us consider now the 3D velocity paths for the MHD flow at $Ha = 700$, $N = 4900$ and $c = 0.1$. Fig.49 shows that the fluid coming from the upstream core crosses the internal layer and expands in the large duct following the shape of the channel. As shown before, neither back flow nor V-shaped path are present on the symmetry plane.

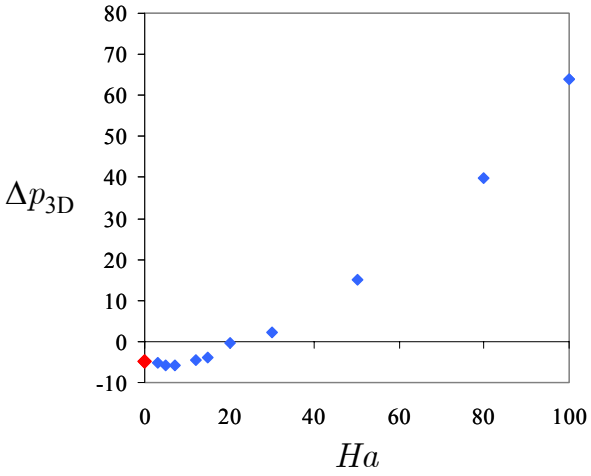

Figure 46: Pressure drop Δp_{3D} as a function of the Hartmann number. The red point indicates the result for the hydrodynamic flow ($Ha = 0$).

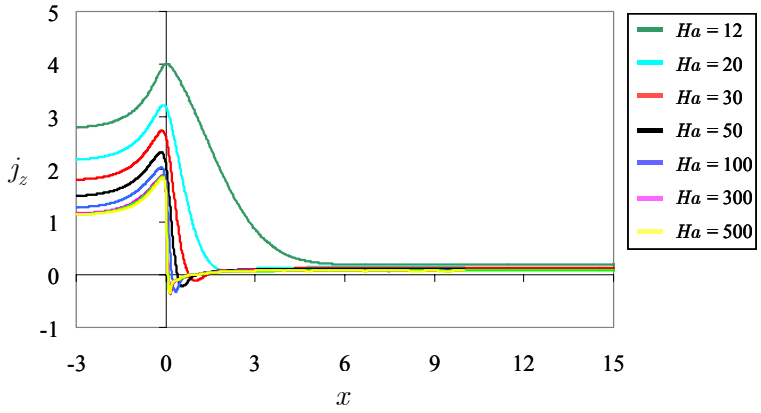

Figure 47: Transverse component of the current density plotted along the axis of the duct for various Hartmann numbers.

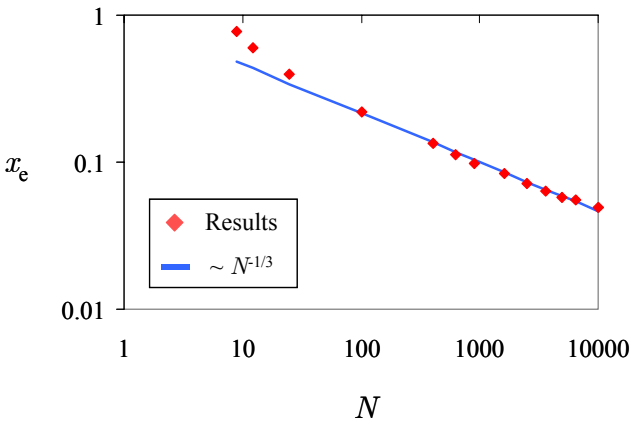

Figure 48: Logarithmic graph of the thickness of the internal layer as a function of the interaction parameter N.

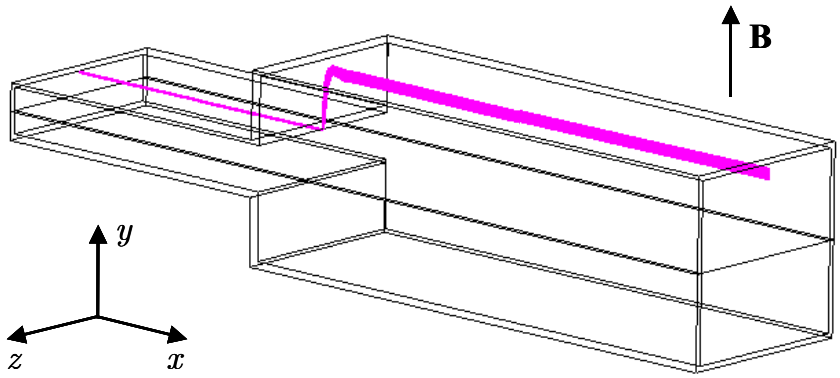

Figure 49: Velocity streamlines for the flow at $Ha = 700$, $N = 4900$ and $c = 0.1$. They describe the transfer of flow from the upstream to the downstream core.

It is interesting to observe how the flow redistributes across the expansion due to the effect of Lorentz forces created by the axial 3D currents. The electromagnetic force is directed towards the lateral walls and as a result the flow is pushed into the side layers. Due to this distribution of the electromagnetic forces, a transverse pressure gradient arises. The pressure is not uniform in a cross-section as can be seen from Fig.50 where the pressure is plotted along the axis at $z = 0$ and close to the side wall ($z \simeq 1$). A non-zero value of the transverse pressure difference indicates three-dimensional MHD effects.

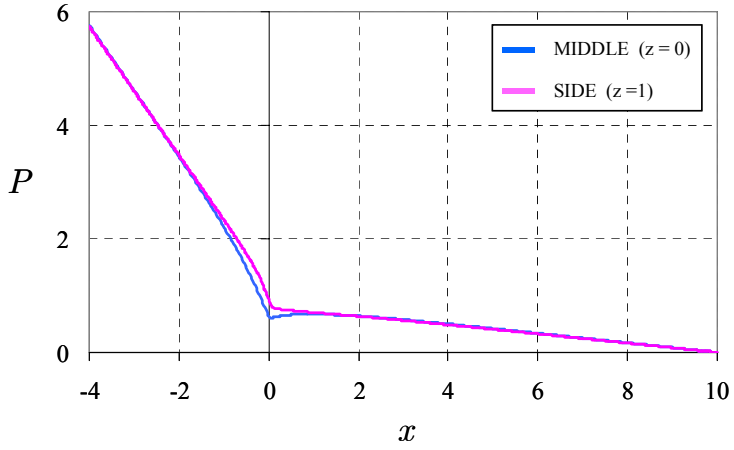

Figure 50: Pressure variation along the centerline of the duct ($z = 0$) and at the side wall ($z = 1$) for $Ha = 700$ and $N = 4900$. In the figure $P = p/N$, where p is the pressure in the hydrodynamic scale.

Fig.51 shows the flow path that transfers the fluid from the upstream core into the internal and the side layer. The expansion layer collects the flow from the core and

redistributes it in the layers that develops along walls parallel to the magnetic field. This exchange of flow between core and parallel layers can be clearly seen in Fig.52 where the velocity streamlines are plotted on the plane $y = 0$ together with the distribution of the transverse velocity component w.

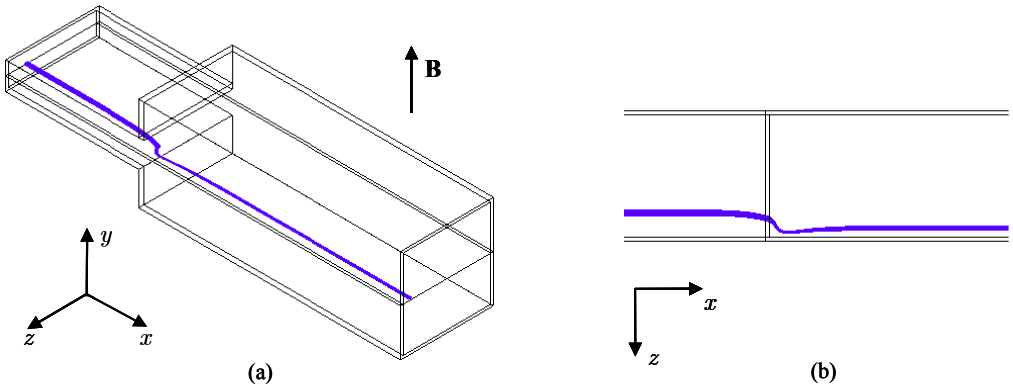

Figure 51: Flow at $Ha = 700$, $N = 4900$ and $c = 0.1$. The streamlines at $y = 0$ show the exchange of flow between the upstream core and the downstream side layer through the internal layer.

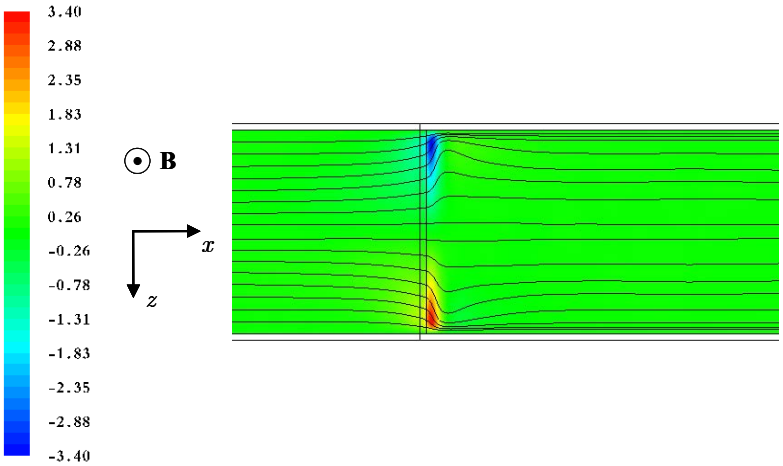

Figure 52: Velocity streamlines on the plane $y = 0$ for $Ha = 700$, $N = 4900$ and $c = 0.1$. The contour plots show the transverse velocity component w.

In Fig.53 the axial velocity u is plotted along the z direction on the symmetry plane $y = 0$ at different axial locations. Upstream the velocity profile is fully developed with a flat uniform core and velocity jets close to the side walls. Approaching the expansion the velocity reduces in the core, increases along the side walls and the profile at the core-side layer interface is deformed. The maximum velocity in the side layer is reached at the expansion. Moving downstream the velocity in the parallel layer reduces and the velocity distribution evolves towards fully established conditions.

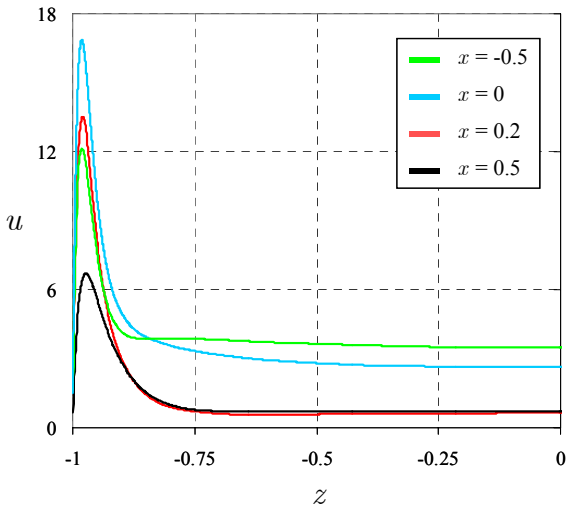

Figure 53: Velocity component u versus the transverse direction z at various axial positions for $Ha = 700$ and $N = 4900$.

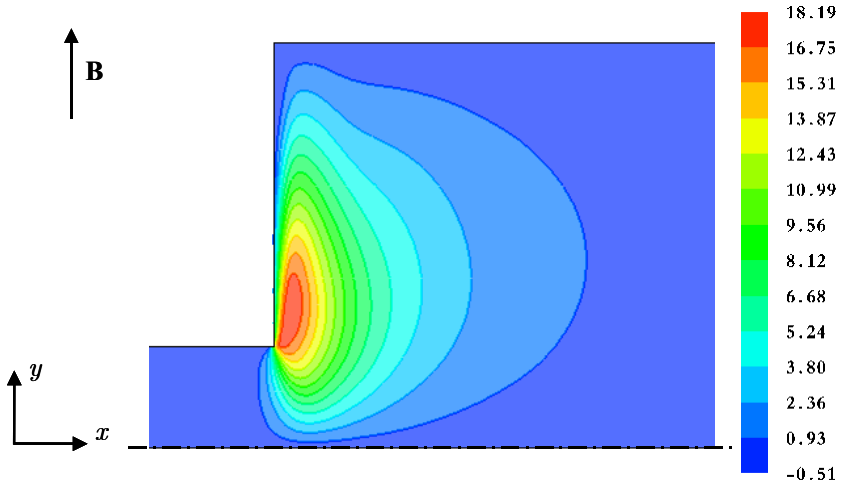

Figure 54: Contour plots of vertical velocity v close to the side wall ($z = 0.98$) for $Ha = 700$, $N = 4900$ and $c = 0.1$.

The rapid redistribution of the flow in the large duct is due to the fact that close to the expansion in the internal layer, a strong vertical component of the velocity occurs, whose magnitude increases approaching the side walls. This can be explained considering that, as shown by the 3D velocity streamlines, at the expansion the flow is redistributed both in the internal layer and in the downstream core.

Fig.54 shows the contour plots of the vertical velocity v in a plane near the parallel wall ($z = 0.98$). The maximum value is reached immediately behind the expansion, close to the internal corner.

In order to complete the description of the flow at large Hartmann numbers, it is still necessary to describe the path that creates the back flow region. For high Hartmann numbers the spiralling motion, present for moderate magnetic fields, is suppressed by the strong electromagnetic forces. A reverse flow is still present near the outer corner of the duct as shown in Fig.55. Here the flow path that involves the side and the internal layer and transfers the fluid towards Hartmann walls and to the core is depicted. Compared to the flow at moderate Hartmann number, the main difference lies in the fact that the zone of back flow does not extend throughout the width of the channel but is confined to the side layer. As a consequence the downward flow near the vertical symmetry plane disappears. The fluid is transferred from the side layer to the center of the channel moving parallel to the vertical wall of the expansion namely in the internal layer. This path is formed by flow coming from the upstream side layer, near Hartmann walls. This

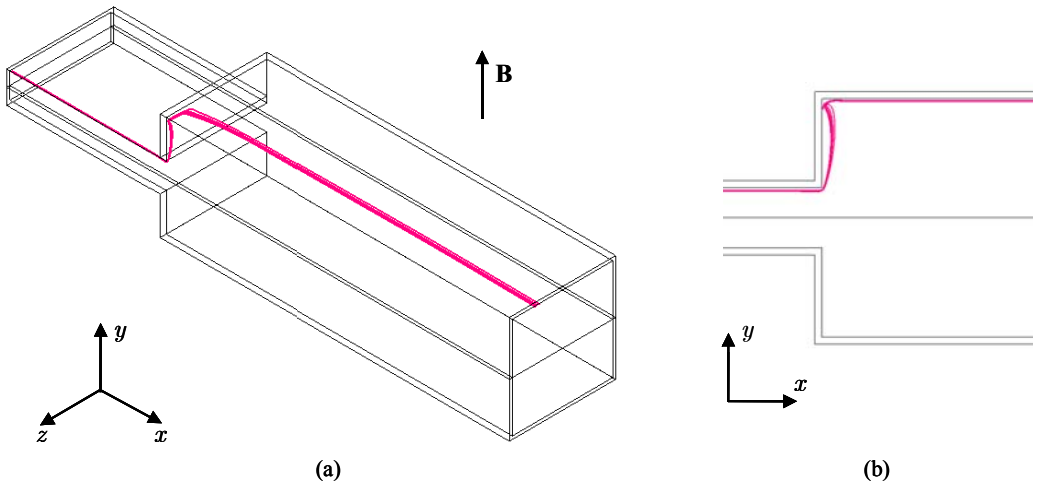

Figure 55: Streamlines for the flow at $Ha = 700$, $N = 4900$ and $c = 0.1$. The reverse flow is confined in the side layer, close to the outer corner of the duct.

motion can be also seen by observing the contour plots of the transverse velocity w close to the parallel walls ($z = 0.95$). In Fig.56 the blue zone indicates a region of negative transverse velocity, where the flow is directed towards the middle of the duct.

In Fig.57 the velocity component w is plotted along the dashed line indicated in the previous figure, located at $x = 0.01$ and close to the parallel wall ($z = 0.95$). The maximum transverse velocity in the expansion layer occurs approximately in correspondence to the internal corners at $y = \pm 0.25$. In the middle of the channel near $y = 0$ the transverse velocity is reduced, while for $|y| > 0.5$ the fluid moves towards the center of

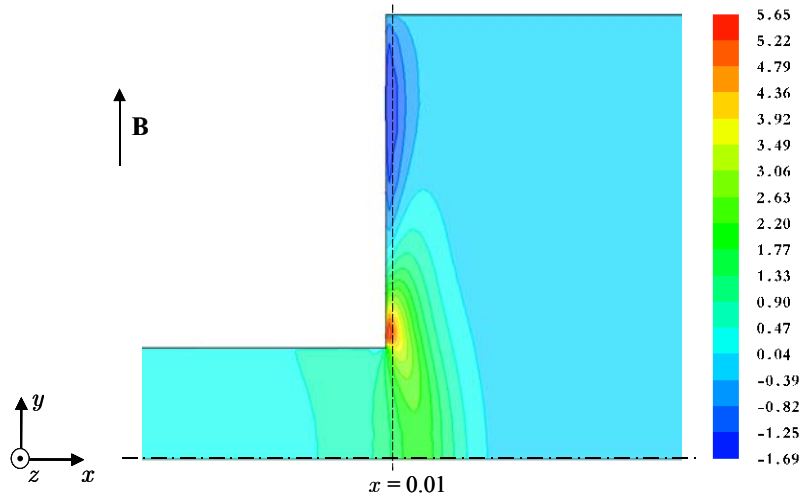

Figure 56: Contour plots of the transverse velocity component w on a plane close to the side wall ($z = 0.95$) for $Ha = 700$, $N = 4900$ and $c = 0.1$.

the duct.

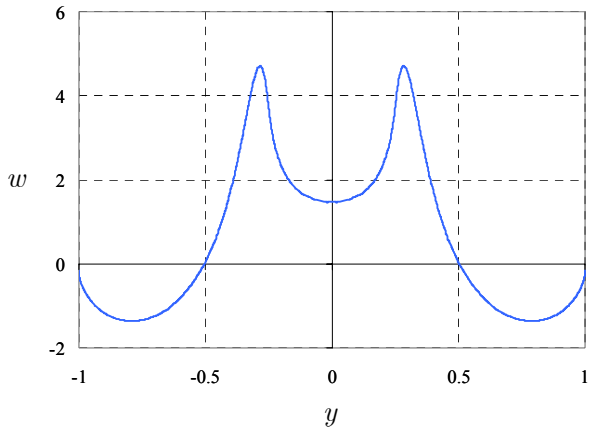

Figure 57: Transverse velocity w along magnetic field direction at $x = 0.01$, close to the side wall ($z = 0.95$) for $Ha = 700$, $N = 4900$ and $c = 0.1$.

Fig.58 summarizes some of the previous results for $x = 0$ showing the changes of the profile of the axial velocity at the expansion with rising the Hartmann number.

For small Hartmann numbers the electromagnetic forces are weak and the magnetic field has only a slight effect on the flow, in addition inertia is strong and as a consequence the velocity profile at the expansion resembles the fully developed distribution. By increasing the Hartmann number the electromagnetic forces become stronger than inertia forces. As a result the velocity reduces in the core and increases in the side layers. This redistribution of the flow leads to the formation of the typical M-shaped velocity profile. Along magnetic field lines the increase of the Hartmann number yields a higher velocity close to the Hartmann walls than in the core (Fig.59).

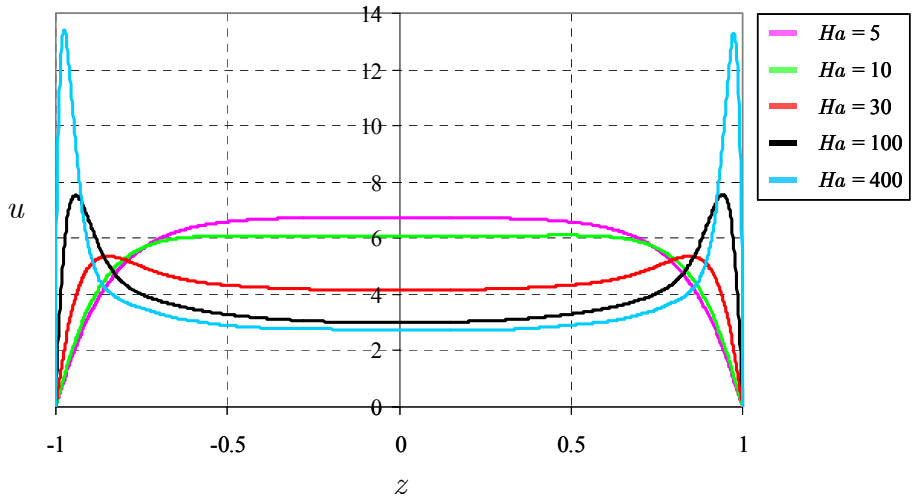

Figure 58: Axial velocity profile along the transverse direction z at $x = 0$ and $y = 0$ for various Hartmann numbers Ha.

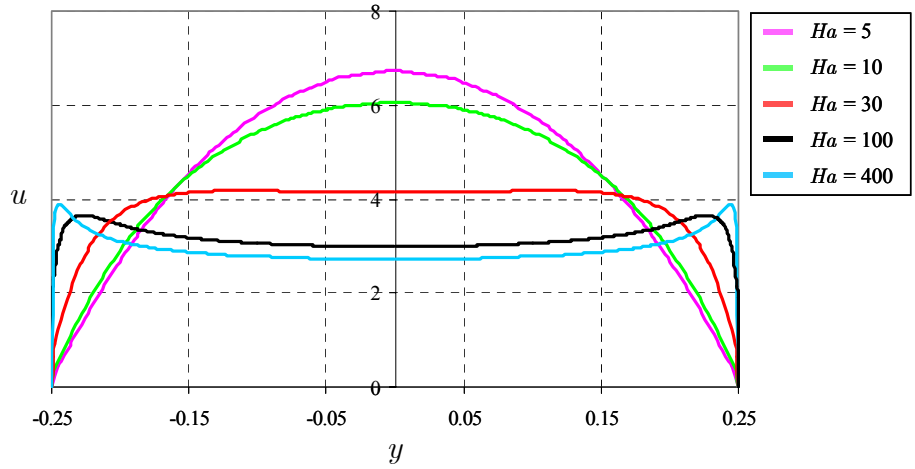

Figure 59: Axial velocity component u plotted along magnetic field lines at $x = 0$ and $z = 0$ for various Hartmann numbers Ha.

After describing the effects of the magnetic field on the velocity distribution, it is interesting to show the modifications that the current field undergoes by increasing the Hartmann number.

In the following the paths of 3D currents are described for the flow at $Ha = 50$ and $Ha = 400$. Due to the symmetry of the solution with respect to the plane $y = 0$, the current loops are shown only for $y > 0$.

In Fig.60 the current paths are depicted for the flow at $Ha = 50$, $N = 25$ and $c = 0.1$. Upstream and downstream at some distance from the expansion the current distribution corresponds to fully developed conditions, the current loops are 2D and they close in cross-sectional planes (path 1). Approaching the expansion the current loops start inclining in the direction of the motion due to the presence of induced axial currents (path 2). It can be seen clearly in Fig.61.

As the walls of the channel are conducting ($c = 0.1$), currents induced in the core can return not only in the boundary layers but also in the walls. Near the expansion currents can flow both through the Hartmann walls of the small duct and in the vertical wall of the expansion as shown by the path 2a in Fig.61.

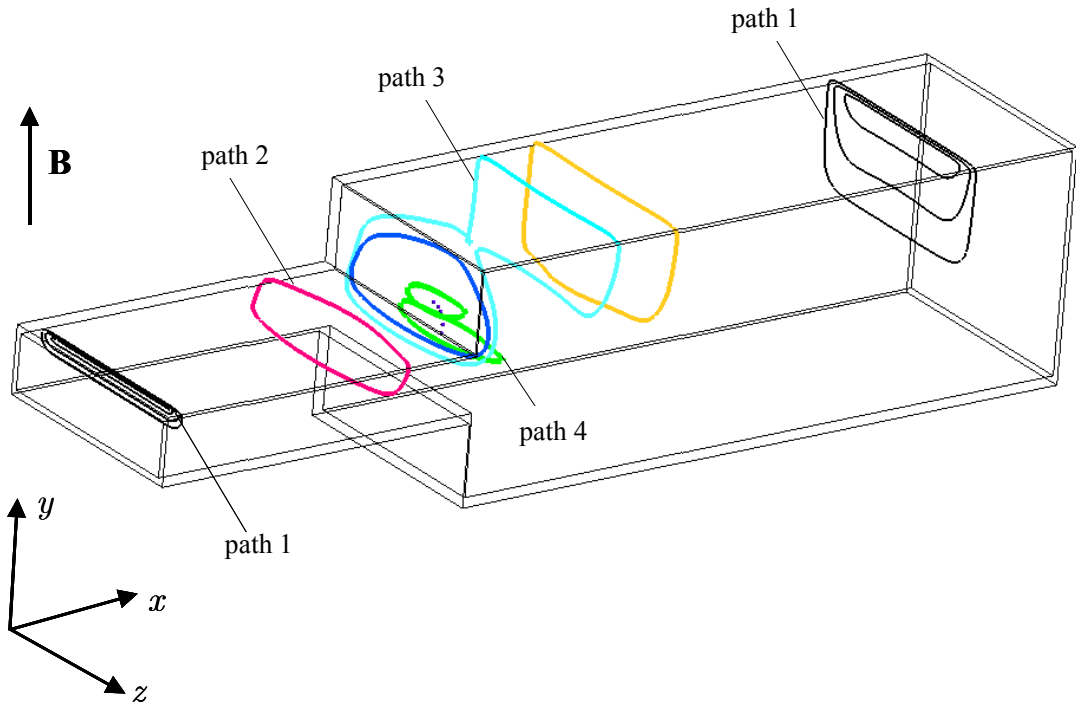

Figure 60: Current paths for the flow at $Ha = 50$, $N = 25$ and $c = 0.1$. The blue points indicate the line around which the core loops develop.

Behind the expansion current loops that close exclusively in the core without involving the boundary layers and the walls are observed (path 4). They create a sort of current tube whose diameter reduces moving upward as indicated by the two green loops in Figs.60 and 61. The centerline of these core loops is marked by the blue points. The tube that develops around this line bends towards the wall of expansion.

The position of the points that form the core line corresponds to the location where

both the axial and the transverse component of current density become zero on a xz plane. When the current tube bends towards the expansion wall, the centre of the loop is defined as the point where the vertical and the z-components of current density vanish on a yz plane.

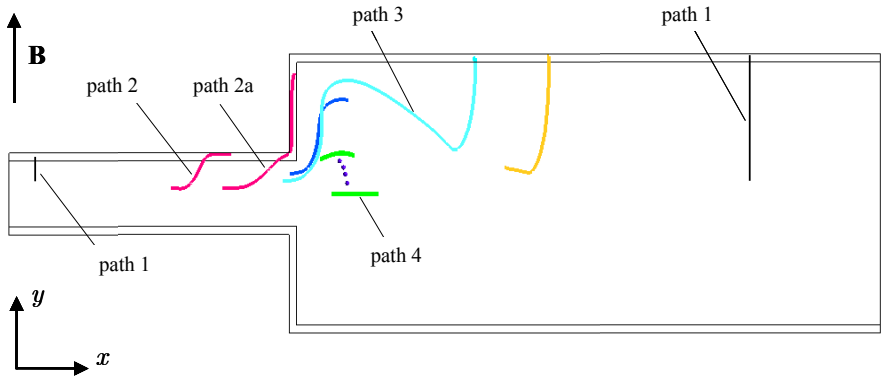

Figure 61: Projection of current streamlines on a xy plane for the flow at $Ha = 50$, $N = 25$ and $c = 0.1$. The blue dots mark the center line of the core loops.

The core loops indicated as path 4 are enclosed in larger paths as shown in Fig.62. The red line marked as path 4a is similar to the core loops described above since it closes only in the core without extending into the side layers or the walls but it is deformed and surrounds all the current tube. The blue line is the line around which core loops develop.

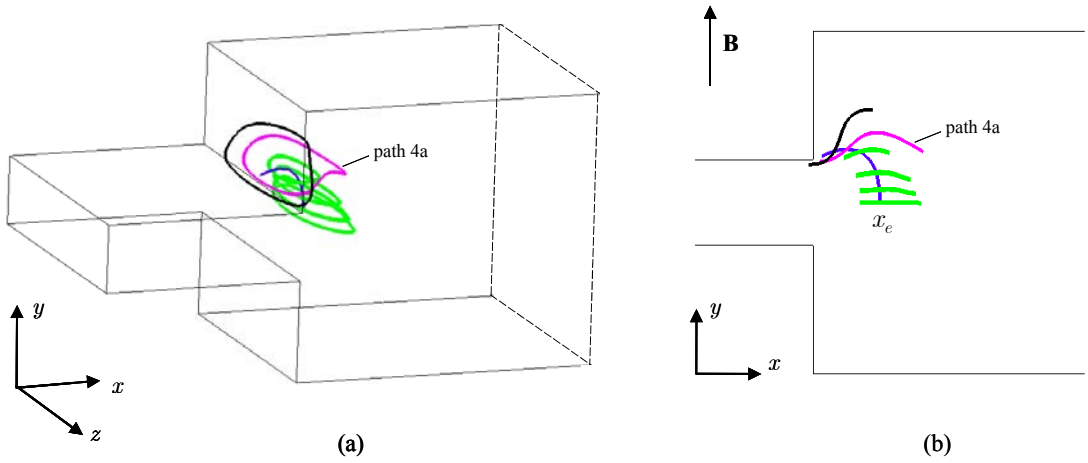

Figure 62: Current streamlines that form the core tube for $Ha = 50$, $N = 25$ and $c = 0.1$. The blue line marks the centerline of the core loops. x_e is the center of the core loop on the plane $y = 0$.

It is interesting to notice the presence of paths that recirculate all around the zone in which a negative transverse component of current density occurs, namely they surround the region where 3D phenomena take place. An example is shown in Figs.60

and 61 (azure path). This loop, named path 3, involves both the side layers and the walls. Behind these paths the current loops start evolving towards the fully developed distribution (yellow path).

Downstream of the zone where the strongest three-dimensional effects occur, the current distribution on a cross-sectional plane can be represented by two small loops near the Hartmann walls, inside large paths that close both in the side layers and in the walls (Fig.63). For higher Hartmann numbers these loops become smaller and move closer to the Hartmann walls. This is due to the fact that these walls are much better conducting than the adjacent layers ($c >> Ha^{-1}$) and therefore almost all the current return through the walls.

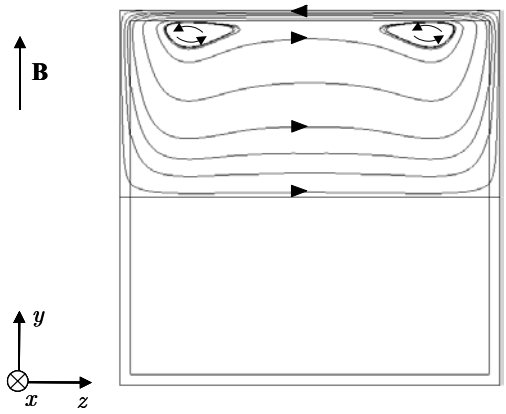

Figure 63: For the flow at $Ha = 50$, $N = 25$ and $c = 0.1$ the current distribution in a cross-sectional plane ($x = 2$), behind the area of strong 3D phenomena, shows two small local loops inside larger paths.

Let us consider now the current distribution for the MHD flow at $Ha = 400$, $N = 1600$ and $c = 0.1$. The same categories of current loops found for the flow at moderate Hartmann numbers can be identified, but the current paths are modified by the action of the increased magnetic field. Figs.64 and 65 show the current path for the flow at $Ha = 400$. The first difference compared with the flow at $Ha = 50$ is the tendency of current loops to develop in the core in planes perpendicular to the magnetic field. Here for high Hartmann numbers the main force balance is established between pressure gradient and Lorentz force and the momentum equation shows that the pressure can be interpreted as a kind of streamfunction for the current. Since in the core the pressure is uniform along magnetic field lines, this supports the observation that the current in the core flows mainly in horizontal planes. The largest values of the y-component of current density are observed inside the parallel walls, close to the internal corners of the cross-section enlargement in the expansion layer.

As shown for the flow at $Ha = 50$, there are current lines that surround the area in which core loops develop (path 3 in Fig.64). Some of these paths, after entering the large duct, move to the middle of the channel before approaching again the side walls as indicated by the blue loop in Fig.64. The point where the current line narrows, close to the centre of the duct, can be interpreted as a saddle point. It indicates the location

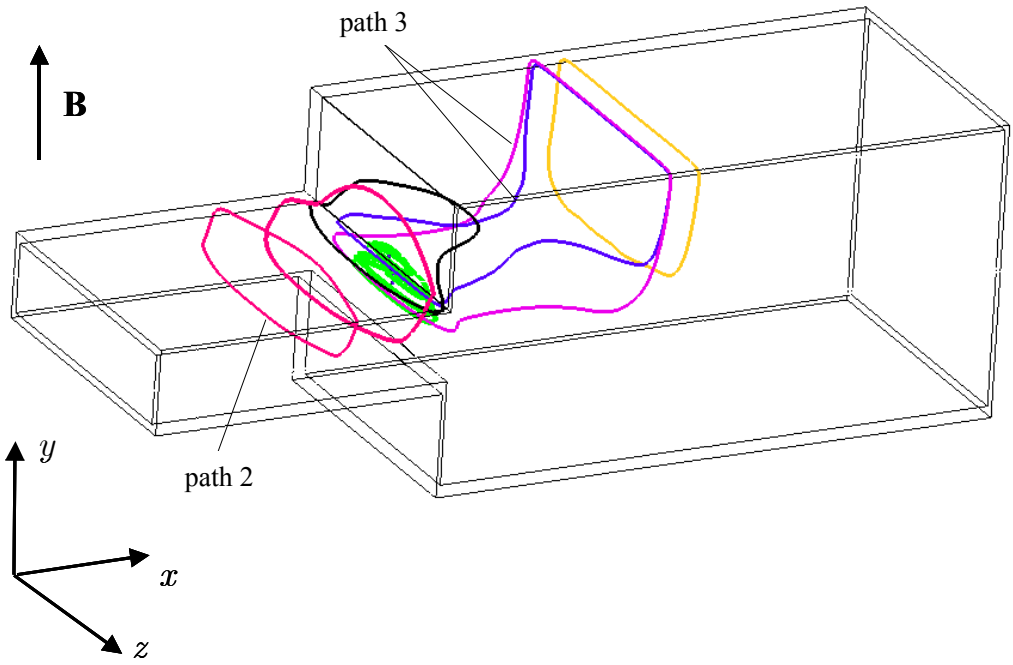

Figure 64: Current streamlines for the flow at $Ha = 400$, $N = 1600$ and $c = 0.1$. The green path is called *path* 4.

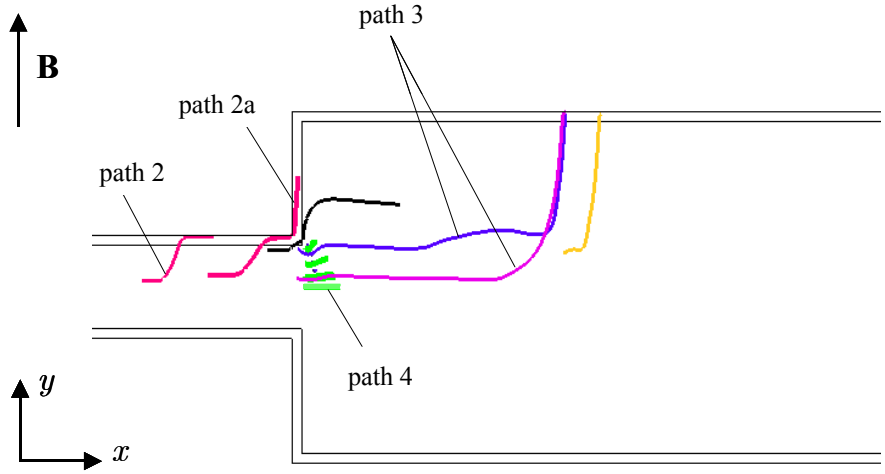

Figure 65: Projection of current streamlines on a xy plane for the flow at $Ha = 400$, $N = 1600$ and $c = 0.1$.

where the transverse component of current density starts flowing again in the direction of the 2D currents. This pattern is schematically represented in Fig.66. Here current streamlines are plotted on the plane $y = 0$. They show the trace of core loops (path 4), whose center is indicate by the red dot, and the path that encloses the zone of strong three-dimensional effects (path 3). The saddle point, marked by the green cross, bounds downstream the region where 3D currents are large enough to give rise to a net negative z-component of current density. In other words the core loops form in front of the saddle point.

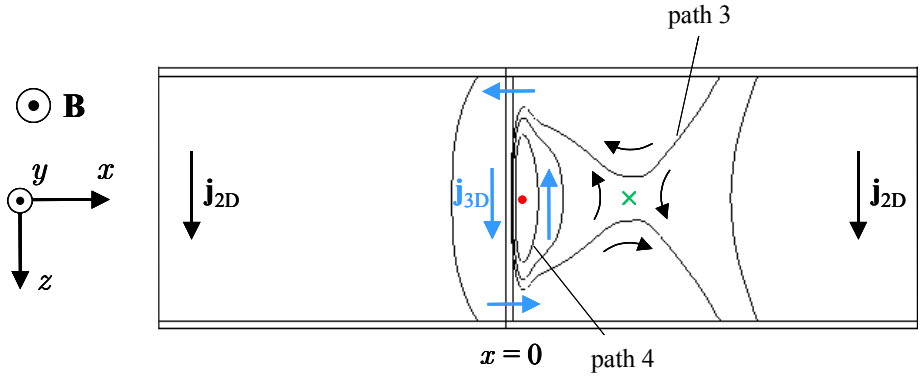

Figure 66: Current paths on the plane $y = 0$ for $Ha = 400$, $N = 1600$ and $c = 0.1$. The center of core loops is marked by the red dot. The green cross indicates the saddle point.

In Fig.67 the transverse component of current density is plotted along the axis of the channel. The point in which j_z becomes negative corresponds to the centre of the core loop on the plane $y = 0$ (red dot) and it has been used as a measure for the thickness of the internal layer. The location where j_z flows again in the same direction as the 2D currents indicates the saddle point (green cross).

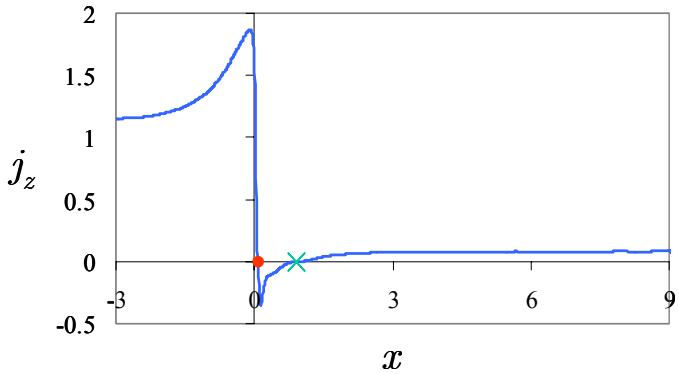

Figure 67: Transverse component of current density plotted along the axis of the duct for $Ha = 400$, $N = 1600$ and $c = 0.1$.

The previous investigation showed that with rising the applied magnetic field the 3D MHD phenomena tend to concentrate close to the expansion, in the internal layer.

This effect can be clearly seen by comparing the position of the centerline of the core loops created by the induced 3D currents for various Hartmann numbers (Fig.68). As shown before by the study of the distribution of the z-component of current density along the axis of the duct, the thickness of the internal layer, measured by x_e, reduces progressively by increasing the Hartmann number.

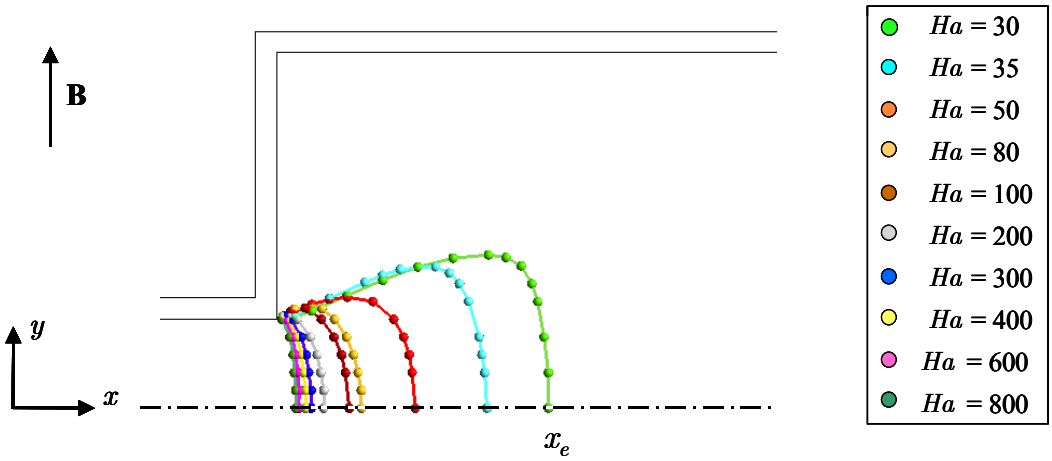

Figure 68: Centerlines of the core loops created by 3D currents for various Hartmann numbers. x_e is the center of the current loop on the plane $y = 0$.

The analysis of limiting current streamlines on yz planes at various axial positions allows to grasp the basic structure of the current field, supporting the foregoing observations. When limiting streamlines are studied, it is important to remember that they are only the trace of three-dimensional current lines on a plane. Therefore in the following discussion they are also named pseudo streamlines.

Fig.69 (a) shows core paths, whose centerline is marked in blue, and loops generated in front of the expansion, which close through the walls and in the core region in the large duct. The vertical line at $x = 0.05$ shows the position of the plane on which limiting current streamlines are drawn. These latter are depicted in Fig.69(b). The center of the pattern of pseudo streamlines coincides with the position where the current tube bends towards the expansion.

Limiting streamlines for the current are also plotted on the plane $x = 0.6$. The results are shown in Figs.70 and 71. In Fig.70(a) the vertical line indicates the position of this plane on which the pseudo current streamlines are represented. In Fig.70(b) the black lines are the limiting current streamlines and those coloured are the 3D paths.

The lines along which they coincide make clear the meaning of pseudo streamlines as projection of 3D loops on a plane. The downward and upward motion in the region close to the side walls is the return path of the current through the side layers and towards the parallel walls. The central part where lines are almost horizontal indicates the uniform core in which current tends to describe 2D paths. The green loops is the line that identifies the saddle point in the center of the duct.

The pattern in Fig.70(b) confirms also the observation that by increasing the magnetic field the Hartmann layer is not a return path for the current since the walls are much better conducting.

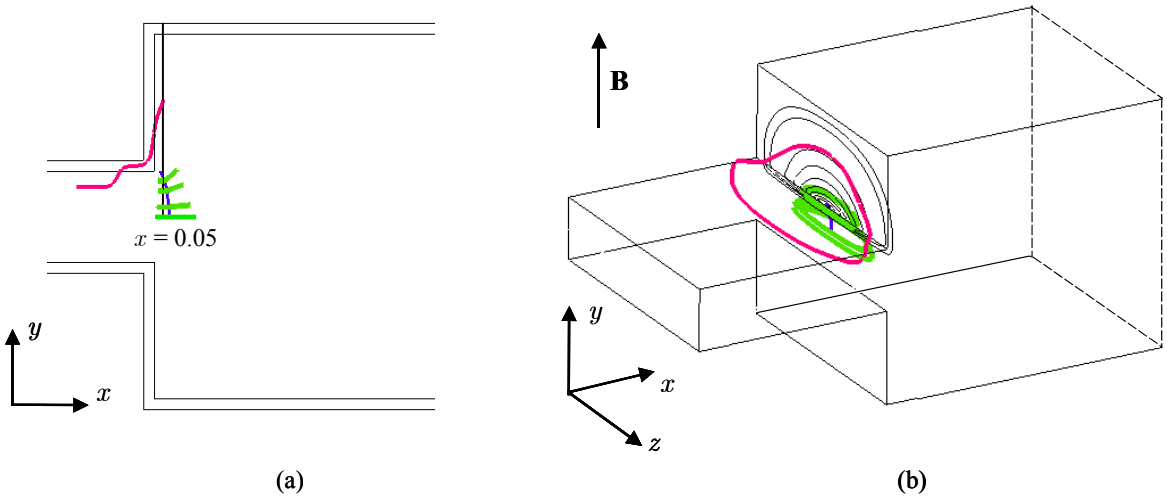

Figure 69: Current paths for $Ha = 400$, $N = 1600$ and $c = 0.1$. (a) The vertical line at $x = 0.05$ indicates the plane on which limiting current streamlines are plotted. (b) Pseudo current streamlines are drawn in black.

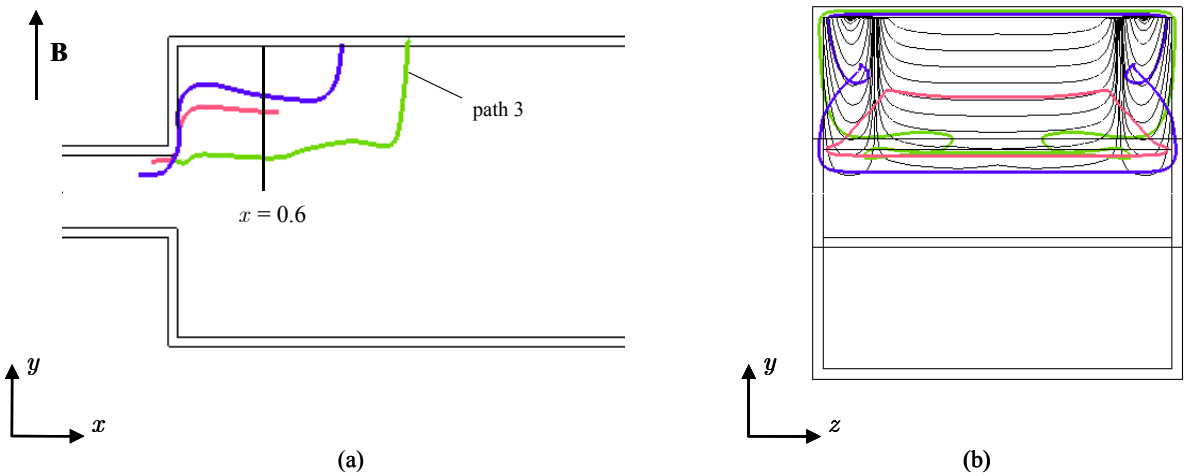

Figure 70: Current lines for $Ha = 400$, $N = 1600$ and $c = 0.1$. (a) The vertical line at $x = 0.6$ indicates the plane on which pseudo streamlines are drawn. (b) Limiting streamlines are plotted in black.

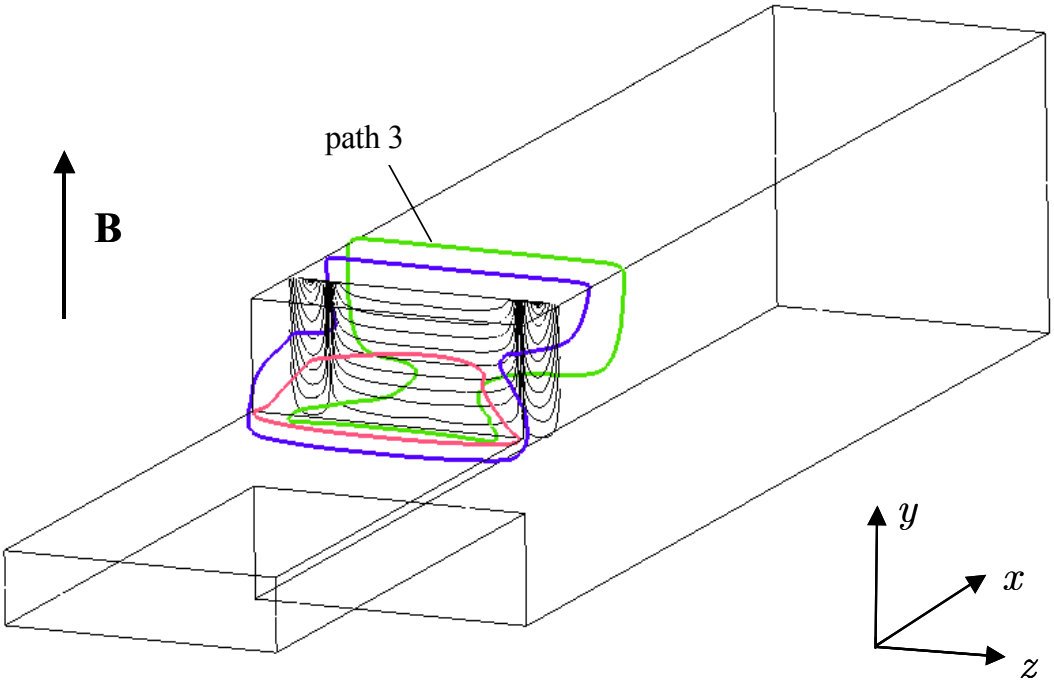

Figure 71: Current loops for $Ha = 400$, $N = 1600$ and $c = 0.1$. The black lines are the pseudo streamlines.

4.3.2 Variation of flow rate at constant magnetic field

In this section the effects of inertia forces on the MHD flow in sudden expansions are investigated by performing a parametric study in which several interaction parameters N are used for a constant Hartmann number of $Ha = 400$.

In order to understand how inertia influences the distribution of the flow in the channel, let us compare first the pattern of velocity streamlines on the symmetry plane $y = 0$ for various interaction parameters (Fig.72).

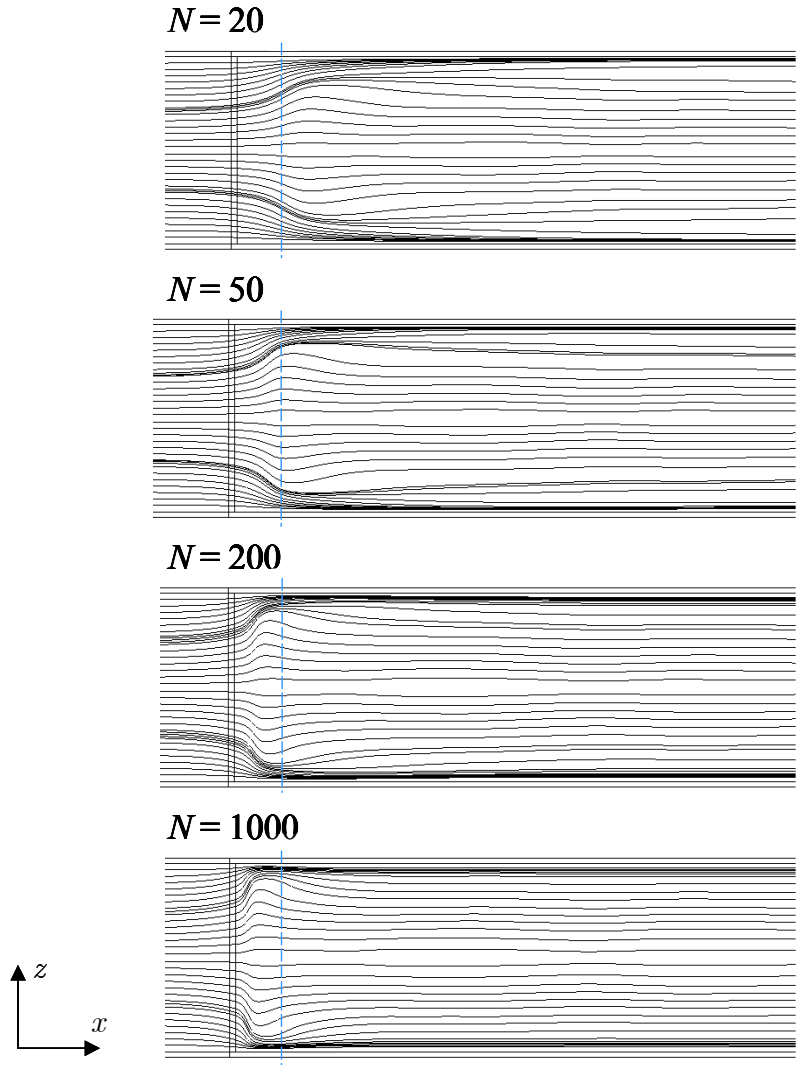

Figure 72: Velocity streamlines on the plane $y = 0$ for the flow at $Ha = 400$, $c = 0.1$ and various interaction parameters N ($Re = Ha^2/N$). The blue lines, located at $x = 0.5$ are used as reference mark.

For small N, the strong inertia forces transport the fluid further downstream and the axial extent of the region where the fluid redistributes towards the side walls increases compared to that for the flow at large interaction parameter. The blue dashed lines

in the figure are located at $x = 0.5$ and they are plotted as a reference. When the importance of electromagnetic forces compared to inertia effects increases, namely for higher interaction parameters, the redistribution of the flow towards the side walls and downstream to the core occurs in a zone closer to the expansion. This behavior is also well described by the rise of the transverse component of the velocity at the expansion that accelerates the fluid towards the parallel walls (Fig.73). As a result, the maximum velocity of the jets that form in the side layers is larger for higher N as displayed in Fig.74.

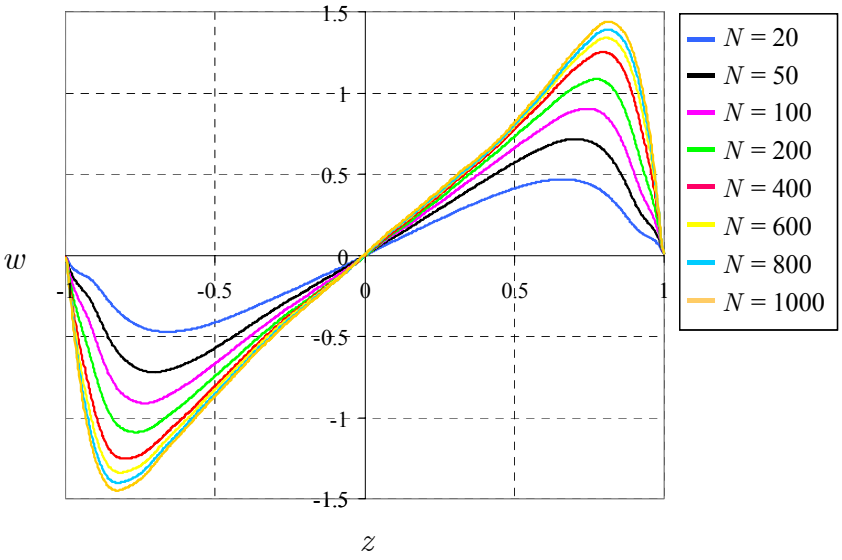

Figure 73: Transverse velocity w plotted along the z direction at the expansion ($x = 0$), on the plane $y = 0$ for $Ha = 400$ and various interaction parameters N.

As described in the previous section and as shown also by the streamlines on the plane $y = 0$ (Fig.72), at the junction between the small and the wide channel a layer, named internal or expansion layer, develops along magnetic field lines, in which the strongest gradients of flow variables are localized. Here, when the values of the interaction parameter and the Hartmann number are such that $N << Ha^{3/2}$, an inertial-electromagnetic balance is established.

In order to find how inertia forces act on the thickness of the internal layer, velocity streamlines are drawn on the middle plane of the duct at $z = 0$ and they are compared for a range of the interaction parameter (Fig.75). The blue dashed lines in figure are located at $x = N^{-1/3}$. This choice is due to the fact that the foregoing investigation confirmed the results of the asymptotic analysis according to which the thickness of the expansion layer in the inertialess limit scales as $N^{-1/3}$. Therefore, at least for large interaction parameters, this is a proper way for displaying the thickness of this parallel layer.

For lower values of N, as shown in the figure for $N = 20$ and 50, the flow coming from the small duct far from the side walls needs some distance from the expansion before approaching the Hartmann walls. As a consequence almost stagnant zones occur near the external edge of the expansion where viscous forces are important and the trace of

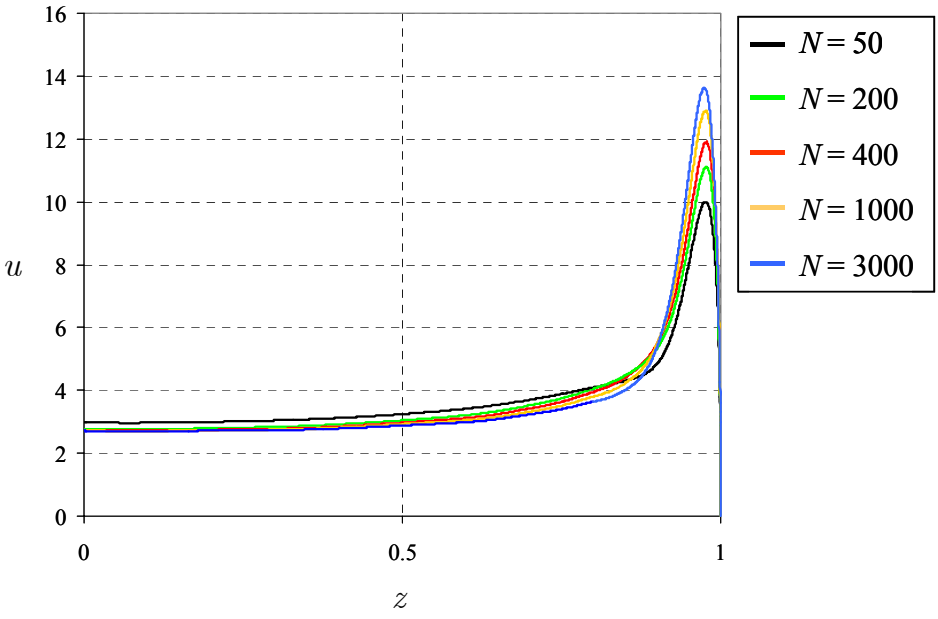

Figure 74: Axial velocity component along the transverse direction z at the expansion ($x = 0$), on the symmetry plane $y = 0$ for $Ha = 400$.

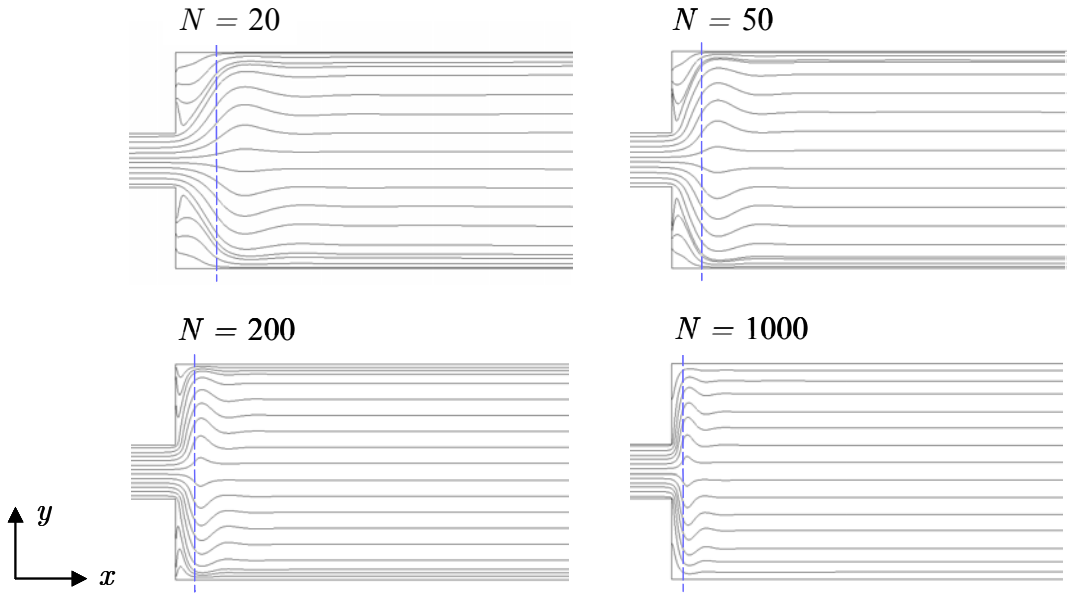

Figure 75: Velocity streamlines on the middle plane of the duct ($z = 0$) for $Ha = 400$. The blue dashed lines are located at $x = N^{-1/3}$.

a V-shaped path is observed on the middle plane of the duct. By rising the interaction parameter, i.e. when inertia forces become weaker and even negligible, at least outside the internal layer where inertia effects might be instead significant, the flow expands into the large channel moving rapidly towards the Hartmann walls. As a result a high vertical velocity v is present near the internal edge of the expansion ($y \simeq 0.25$) within the expansion layer.

In Figs.76 and 77 the vertical velocity v is plotted along the axial direction at $y = 0.25$ on the middle plane of the channel ($z = 0$) and near the side wall ($z = 0.98$), respectively. For large interaction parameters the velocity distribution on the central plane of the duct suggests that first the flow redistributes quickly towards the Hartmann walls as indicated by the strong positive vertical velocity and then the fluid spreads through the core moving slightly downward as indicate by the negative values of v. By decreasing the interaction parameter the maximum vertical velocity reduces and the negative values tend to disappear. This supports the prior observations concerning the fact that at small N the flow distributes slowly over the cross-section of the duct. When inertia forces are weaker the location of the maximum vertical velocity moves closer to the exit of the small channel.

By comparing the velocity profiles at $z = 0$ and $z = 0.98$ it can be seen that the vertical velocity reaches the highest values near the parallel side walls.

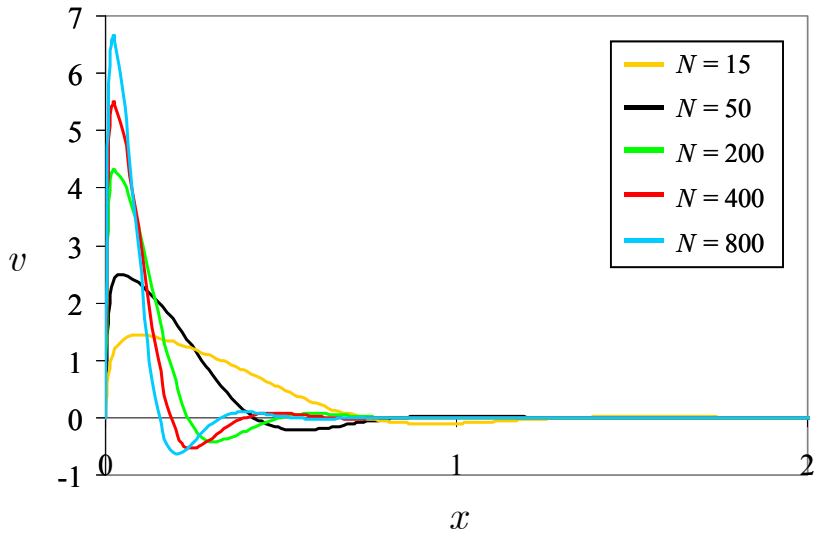

Figure 76: Vertical velocity plotted along the axial direction near the internal edge of the expansion at $y = 0.25$, on the middle plane at $z = 0$ for $Ha = 400$ and a range of the interaction parameter N.

In the following the modifications of the 3D flow structures due to the action of inertia forces are analyzed. Fig.78 shows the flow paths that transfer the fluid from the upstream side layer, close to the Hartmann layers, towards the Hartmann walls of the large duct and backward to the expansion wall. The fluid is then transported close to the middle plane of the channel. These paths create the V-shaped trajectory observed while analyzing the velocity streamlines on the plane $z = 0$.

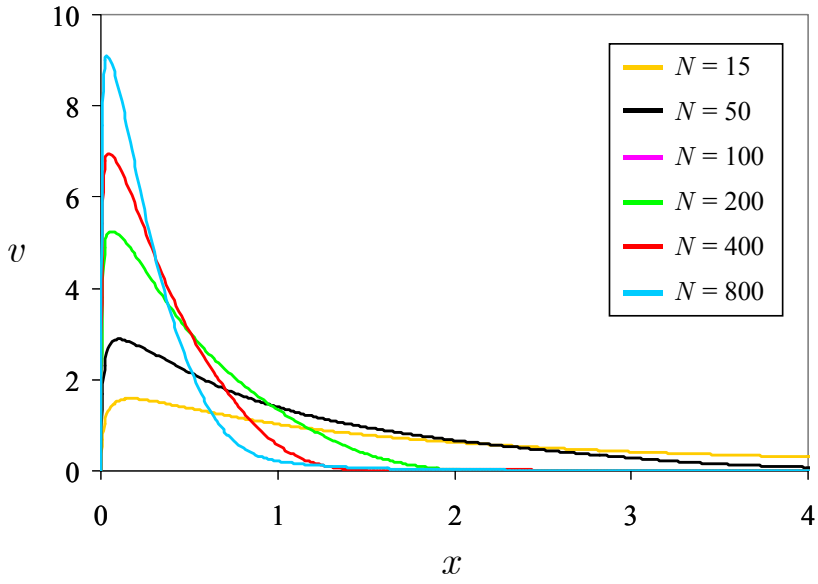

Figure 77: Vertical velocity plotted along the x direction near the internal edge of the expansion at $y = 0.25$, close to the side wall at $z = 0.98$ for $Ha = 400$ and various interaction parameters N.

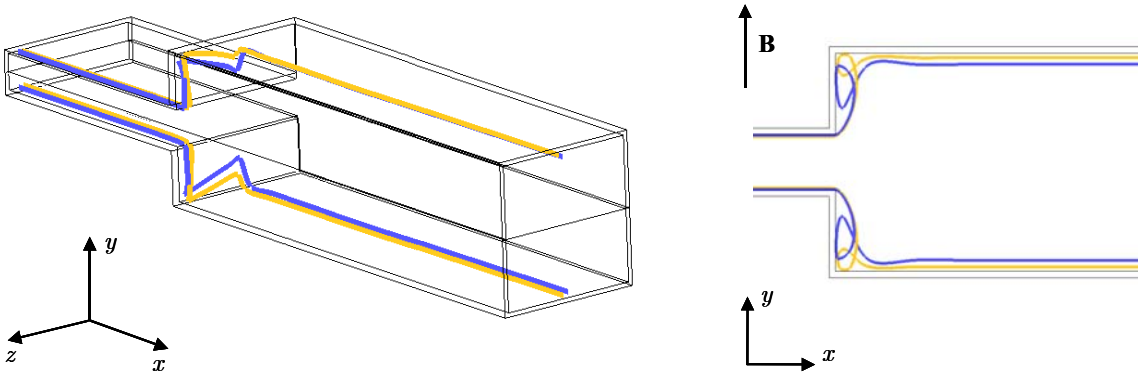

Figure 78: Flow paths for $Ha = 400$ and $N = 50$ that transport the fluid from the upstream side layer, close to the horizontal walls, towards the Hartmann walls and to the center of the duct forming, near the middle plane, a V-shaped trajectory.

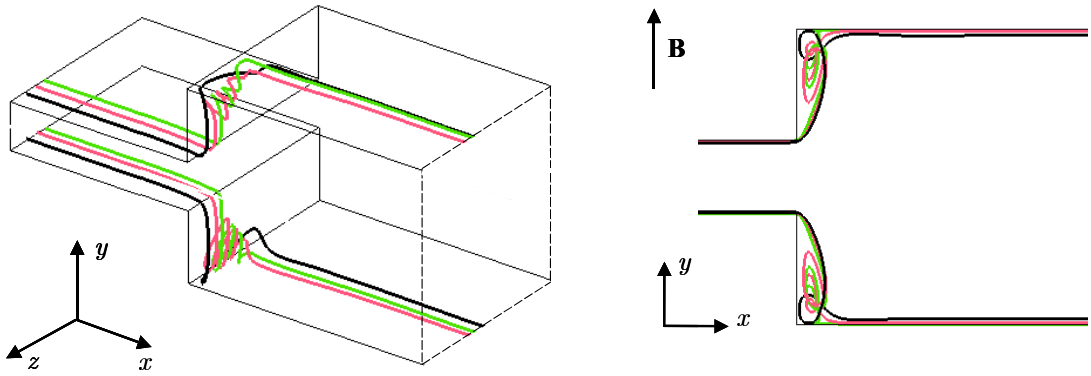

(a) (b)

Figure 79: The red and the green paths represent the swirling motion that appears for small and moderate interaction parameters. The results are for the flow at $Ha = 400$ and $N = 50$.

When inertia is sufficiently strong ($N \leqslant 100$) vortical structures appear, which transport the fluid from points near the upstream Hartmann layers to the symmetry plane $z = 0$ and towards Hartmann walls (Fig.79). It can be observed that compared with the swirling motion described for the flow at small and moderate Hartmann numbers (Section 4.3.1), which was created by particles inserted very close to the side walls, the vortical path occurring at $Ha = 400$ and moderate N is created by fluid injected at some distance from the parallel walls (red and green paths in Fig.79(a)). The flow coming from the upstream side layer, near the lateral walls contributes instead to the particle track that describes the V-shaped trajectory (black streamline in Fig.79). In the range of N investigated the vortices do not reach the middle plane of the channel.

Considering the vortex core line, which the streamlines spiral around, it ends very close to the Hartmann walls. For $N = 8$ two symmetric foci, centers of the swirling motion, are found on the first plane of nodes in the fluid domain adjacent and parallel to the Hartmann walls. This can be seen in Fig.80 where limiting streamlines are plotted on the walls perpendicular to the magnetic field. The red dots indicate critical points that act as sources of streamlines, the green crosses are saddle points and for $N = 8$ the red circles mark the foci, which are the final points of the vortex core line. Along the blue curves the axial component of the velocity is zero. By reducing the relative strength of inertia with respect to electromagnetic forces, only the two sources close to the side walls remain and they move progressively towards the expansion wall. This supports the results that show how strong electromagnetic forces tend to suppress vortical flow structures.

The top view in Fig.81 shows the vortical paths for $Ha = 400$ and $N = 50$ together with the line along which the axial component of the velocity vanishes (blue curve). It confirms the observations resulting from the previous analysis stating that this curve provides useful information about the size of the regions where the vortices occur. When inertia forces are much weaker than the electromagnetic forces so that no swirling motion appears, this line marks the zone in which the flow directed towards the expansion wall takes place.

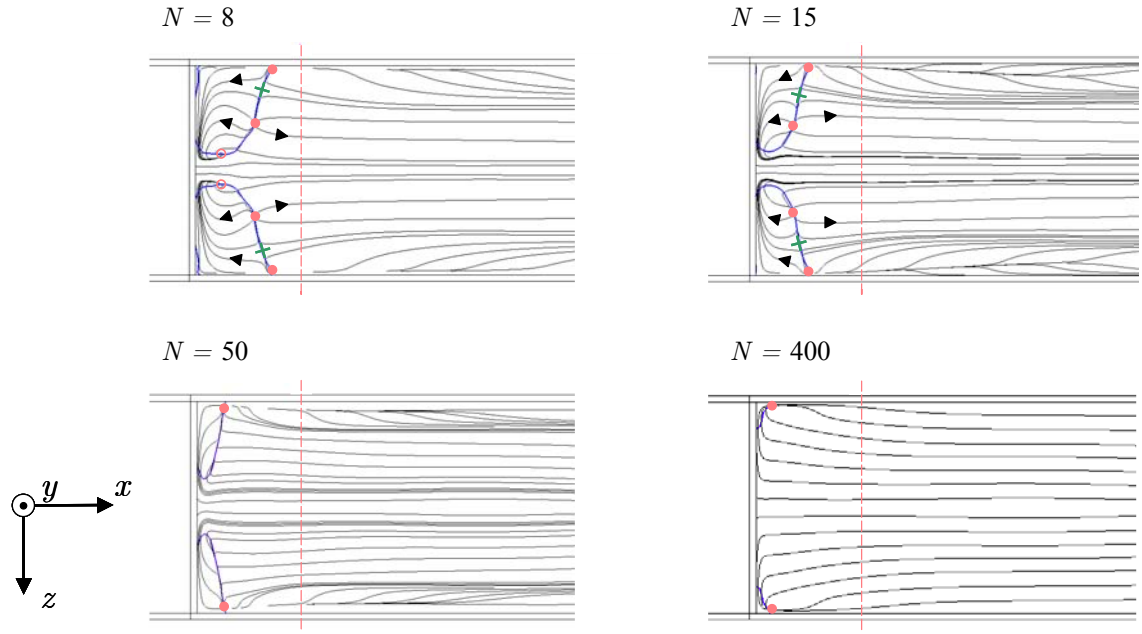

Figure 80: Limiting velocity streamlines plotted on the Hartmann walls for $Ha = 400$ and four different interaction parameters N. The red dots indicate critical points acting as sources, the green crosses are saddle points and the circles present for $N = 8$ are foci. The dashed lines are located at $x = 1$ as reference mark.

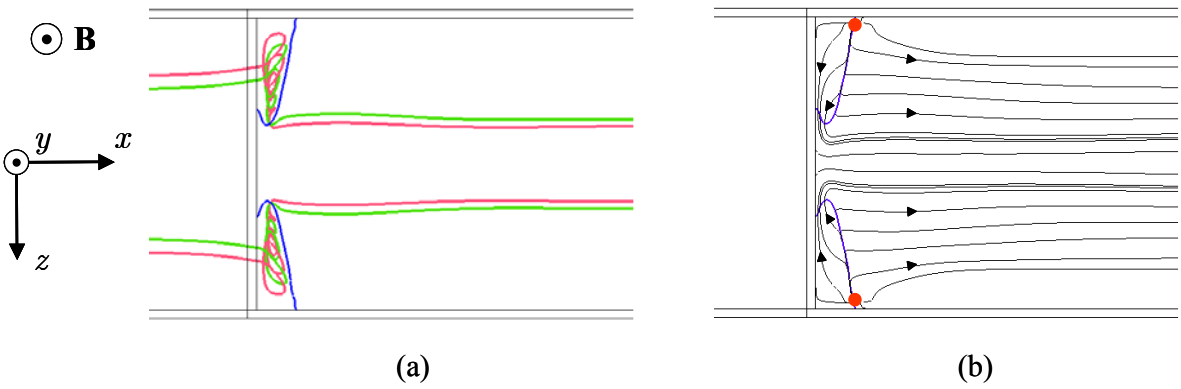

Figure 81: (a) Top view of vortices formed behind the expansion (green and red paths) for the flow at $Ha = 400$ and $N = 50$. The blue curve indicates the points where the axial velocity components u becomes zero. (b) Limiting streamlines are plotted on the Hartmann wall. The red dots are critical points that act as sources of streamlines.

The lines where the x-component of the velocity is zero can be therefore used to get a global view of inertial effects on the MHD flow at $Ha = 400$. In Fig.82 these lines are plotted on the Hartmann wall and compared for various interaction parameters. By reducing N, the back flow region grows both in the axial and in the transverse direction. For $N \leqslant 100$ the vortical flow structures start appearing.

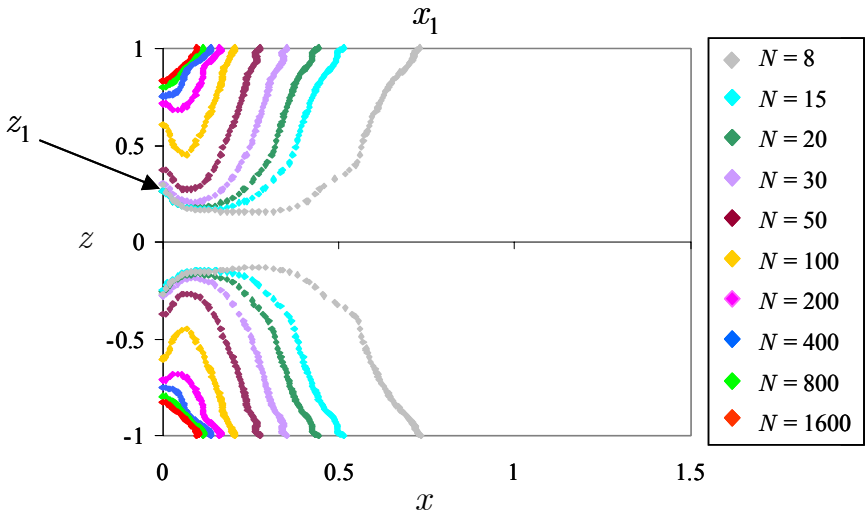

Figure 82: Lines where the x-component of the velocity is zero plotted on the Hartmann wall for $Ha = 400$ and several interaction parameters N. x_1 marks the end of the back flow region on the side wall, z_1 indicates the extent of the zone of reverse flow on the expansion wall.

In Fig.83(a) the axial position of the point x_1 that identifies on the side wall the end of the zone of back flow is plotted as a function of $N^{-1/3}$. The results suggest that in the inertialess limit, namely for very high interaction parameters ($N \longrightarrow \infty$), the size of the back flow region on the side wall tends to a finite value. This means that even when inertia is negligible a small zone with negative velocities remains in the corners of the expansion. Considering the straight line that fits in the best way the results for high interaction parameters and extrapolating this line towards infinite N the finite value $x_{1,\infty}$ is found. In Fig.83(b) the quantity $x_1 - x_{1,\infty}$, which measures the inertial fraction of the reattachment length, versus the interaction parameter N is shown in logarithmic scale. The results indicate that by increasing N the thickness of the inertial part of the zone of reverse flow reduces as $N^{-1/3}$.

It is also interesting to study the evolution of the transverse size of the area of reverse flow along the expansion wall. This is indicated by the location of the point z_1 marked in Fig.82. The results in Fig.84 show that when inertia effects reduce ($N^{-1/3} \longrightarrow 0$), the dimension of the back flow region on the expansion wall tends to a value different from zero. For small interaction parameters this extent remains almost constant.

Following the same approach used for the study of the effects of an increasing magnetic field at constant flow rate ($Re = const$), the axial position x_e of the center of the

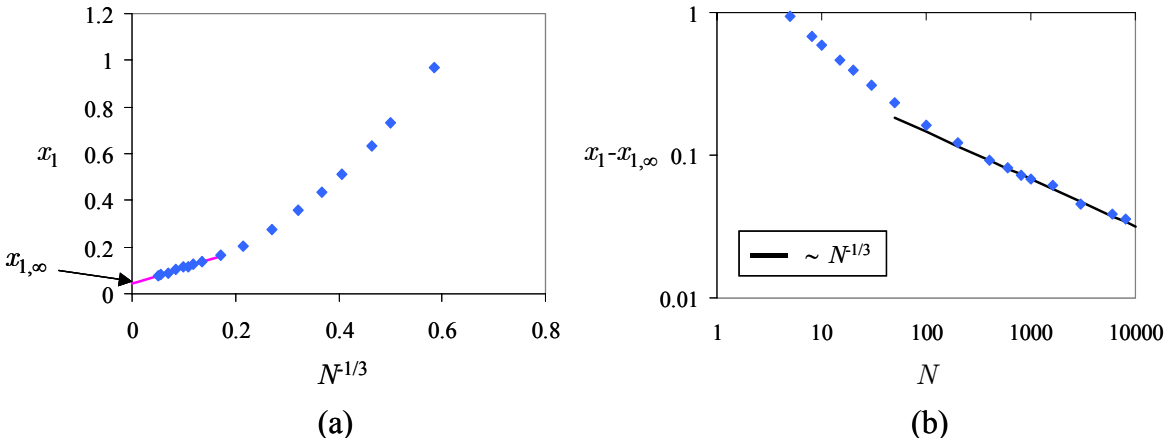

Figure 83: (a) Axial position of the point x_1 on the side wall that bounds the back flow region, plotted as a function of $N^{-1/3}$. $x_{1,\infty}$ is the value of the reattachment length in the inertialess limit ($N \longrightarrow \infty$). (b) Inertial part of the reattachment length versus N.

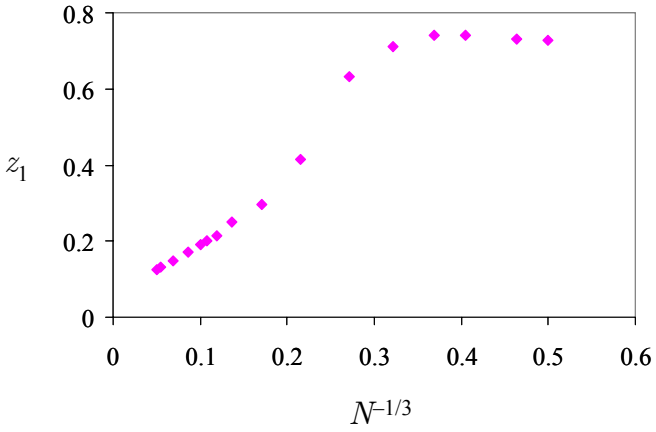

Figure 84: Size of the region of reverse flow along the expansion wall versus $N^{-1/3}$.

current loops formed on the plane $y = 0$ in the core region of the duct is assumed as a measure for the thickness of the internal layer. It is defined as the point on the axis of the channel where the transverse component j_z of the current density changes the sign. The position of the core lines of the current tubes, formed by these current core paths, is compared for various interaction parameters in Fig.85. It is important to notice that the concept of internal layer can be applied only as long as $x_e << L$ where L is the characteristic length of the duct.

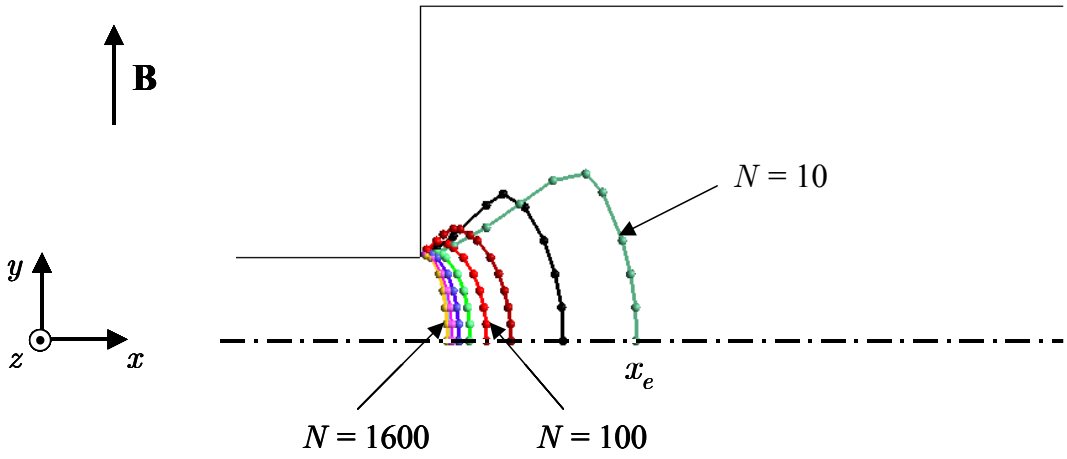

Figure 85: Centerlines of the current tubes that form in the core region of the duct for $Ha = 400$. x_e is the centre of the current loop on the plane $y = 0$ and it is used as a measure for the thickness of the internal layer.

In Fig.86(a) the thickness of the internal layer is plotted as a function of $N^{-1/3}$. As for the reattachment length, the results indicate that in the inertialess limit, as $N^{-1/3} \longrightarrow 0$, the size of the expansion layer tends to a finite value $x_{e,\infty}$. This latter is found by extrapolating the linear trend towards infinite N. In Fig.86(b) the inertial fraction $x_e - x_{e,\infty}$ of the internal layer is plotted as a function of the interaction parameter N in logarithmic scale. Approaching the inertialess limit the inertial part of the thickness of the expansion layer varies as $N^{-1/3}$.

The evolution of the thickness of the expansion layer resembles closely that of the point x_1 that bounds the reverse flow zone on the side wall. It can be observed that for large interaction parameters the inertial part of the internal layer and of the reattachment length have the same asymptotic behavior, but $x_1 - x_{1,\infty}$ is larger than $x_e - x_{e,\infty}$ as shown in Fig.87.

The application of MHD effects to technical devices and industrial processes requires not only the knowledge of the flow distribution but also of the additional pressure drop Δp_{3D} caused by the 3D MHD phenomena that occur across the expansion.

The variation of the pressure along the axis of the channel is depicted in Fig.88 for the flow at $Ha = 400$ and three interaction parameters. Here the variable P is again given by the pressure in the hydrodynamic scale, as defined in Section 2.2, divided by the interaction parameter N.

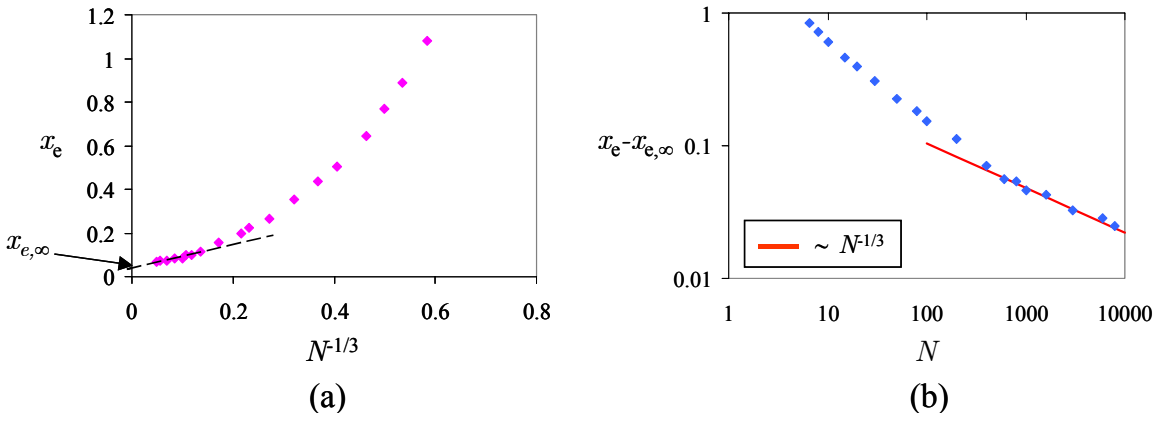

Figure 86: (a) Thickness of the internal layer as a function of $N^{-1/3}$ for $Ha = 400$. (b) Thickness of the inertial part of the internal layer $x_e - x_{e,\infty}$ plotted versus the interaction parameter N in logarithmic scale.

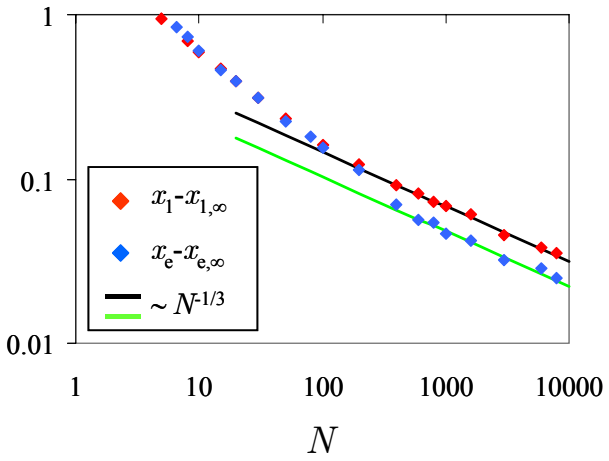

Figure 87: Inertial part of the thickness of the internal layer $(x_e - x_{e,\infty})$ and of the reattachment length on the side wall $(x_1 - x_{1,\infty})$ as a function of N.

Fig.88 shows that both at the inlet and at the outlet of the duct at some distance from the expansion fully developed conditions are established, characterized by a constant pressure gradient. This latter is indicated by the straight lines both in the small and in the large channels. With increasing inertia, i.e. with decreasing N, the total pressure drop increases.

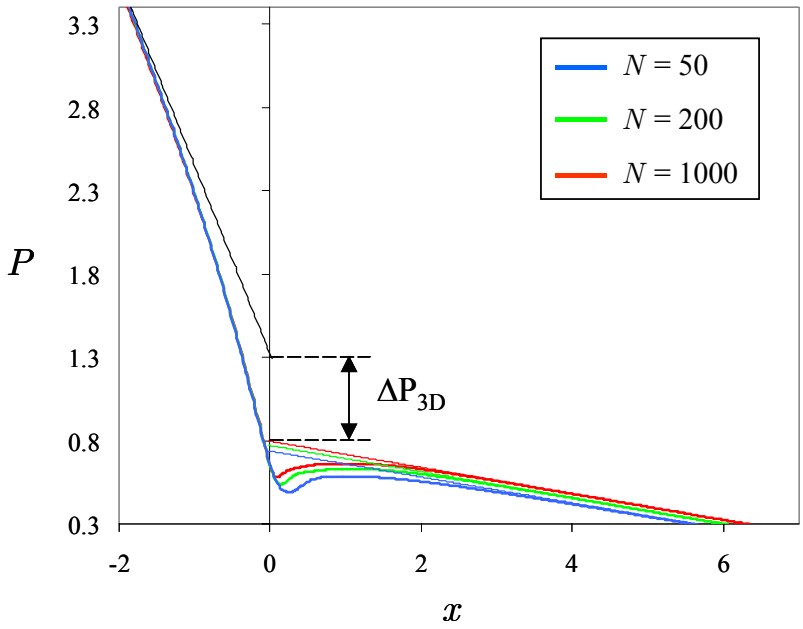

Figure 88: Pressure distribution along the axis of the duct for $Ha = 400$ and three interaction parameters N. The straight lines indicate the fully developed pressure gradients in the small and in the large channel. The additional pressure drop due to 3D MHD effects is indicated by ΔP_{3D} for $N = 1000$. The quantity P is given by p/N where p is the pressure in the hydrodynamic scale.

In Fig.89 the additional MHD pressure drop is plotted as a function of $N^{-1/3}$. For moderate interaction parameters ($N \simeq 40$) a maximum value for the pressure drop is found. For large interaction parameters ($N^{-1/3} \to 0$) the pressure drop seems to reduce as $N^{-1/3}$.

The results of this parametric study show that even for high interaction parameters (e.g. $N = 3000$) there is an effect of inertia on the flow distribution. The changes that the velocity field undergoes for large N are localized mainly in the side layers as shown by the increase of the axial velocity in the parallel layers at the expansion. Inertial effects are also important in the internal layer. By raising the relative importance of inertia forces compared to Lorentz forces, i.e. by reducing the interaction parameter, first the internal layer becomes thicker and as a consequence the redistribution of the flow towards the side layers occurs over a longer axial distance. Then a further decrease

of the interaction parameter leads to the formation of vortical structures that involve both the parallel layers and the core of the duct.

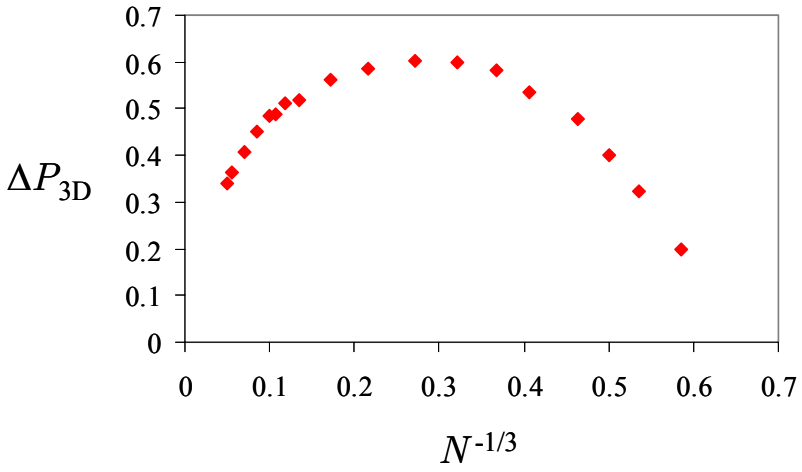

Figure 89: Pressure drop due to 3D MHD phenomena plotted as a function of $N^{-1/3}$ for $Ha = 400$.

4.4 Comparison with experimental data

In the following section, the numerical results are compared with the available experimental data. Experiments on MHD flows in conducting rectangular channels with a sudden expansion have been performed in the MEKKA laboratory of the Forschungszentrum Karlsruhe (Horanyi et al. (2005)).

Fig.90 shows a sketch of the test section. It is positioned in such a way that the main flow direction is perpendicular to the magnetic field that is generated by a dipole magnet. Its strength can reach 2.1 T. The cross-section of the channel enlarges along the field direction and the expansion ratio is four. The stainless steel wall has a thickness of 3 mm and the resultant conductance parameter is around 0.03.

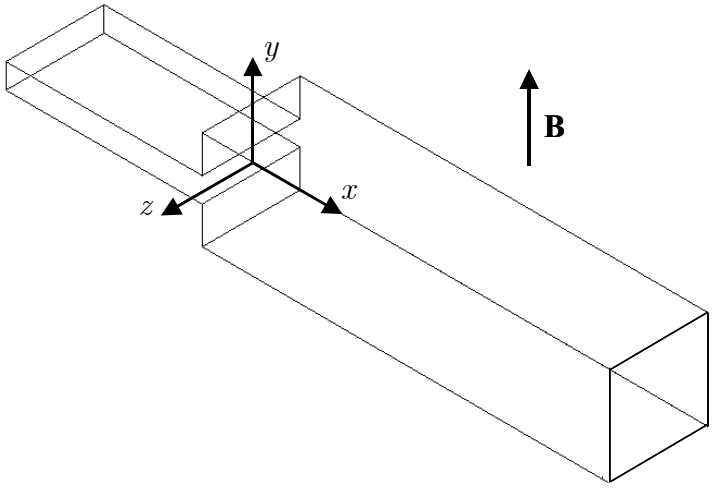

Figure 90: Geometry used in the experiments. The expansion ratio of the duct is 4 and the conductance parameter c is 0.03.

The operating fluid is the eutectic sodium-potassium alloy $Na^{22}K^{78}$. This operating medium has been chosen because its physical properties, the high specific electric conductivity and the low density, allow to get the characteristic numbers, namely the Hartmann number Ha and the interaction parameter N, typical in a fusion reactor blanket. A proper choice of the working fluid is also related to its chemical behavior and to operational and safety aspects. The choice of sodium-potassium alloy ensures for instance a good electrical wetting of the fluid-wall interface and the possibility of working at room temperature. Problems associated with the use of this operating fluid concerns its reactivity with moist air and the consequent fire and explosion hazard.

The measured quantities that are compared with the calculations are the pressure variation along the streamwise direction and the surface potential.

Pressure difference measurements are performed by means of four capacitive pressure transducers of different sensitivity arranged in parallel. Fig.91(a) shows the test section and some of the 16 pipes used for measuring the pressure differences. A valve system switches the pipes connected with the transducers, selecting in this way the discrete points between which pressure difference is measured.

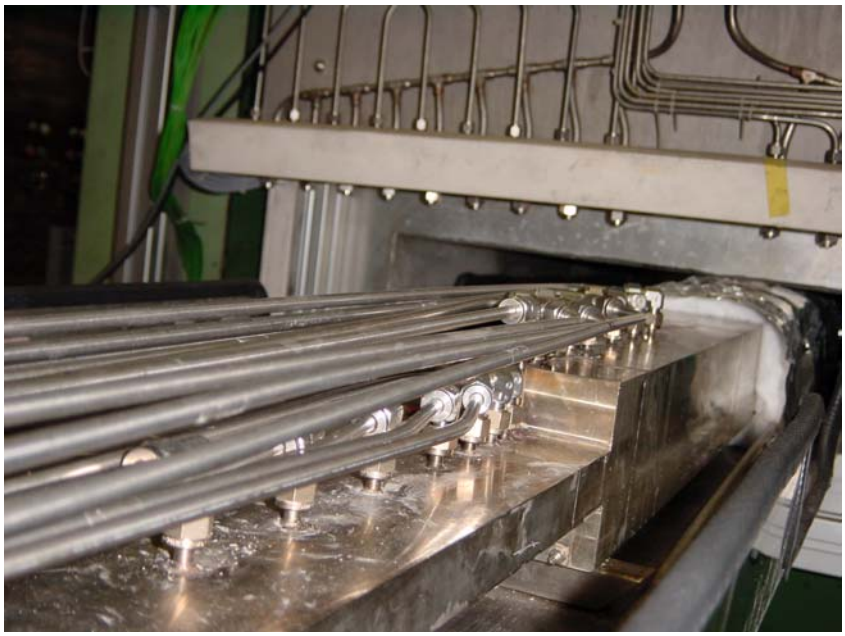

(a)

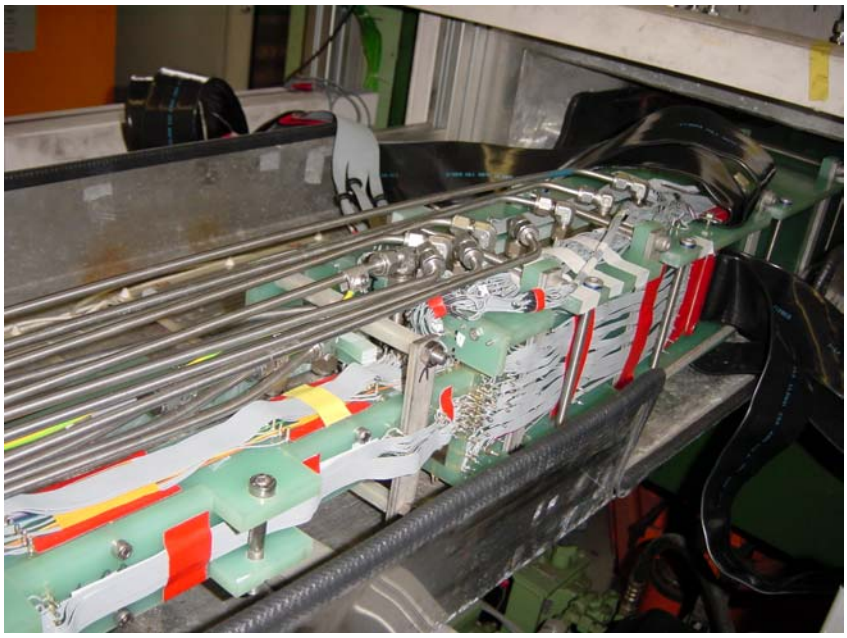

(b)

Figure 91: (a) Test section connected to the 16 pipes used for pressure difference measurements. (b) Insulating plates that cover the test section fitted with electric potential probes.

The values of electric potential on the walls of the duct are measured by more than 300 spring loaded needles positioned on insulating plates that cover the test section. In Fig.91(b) one can see the fiberglass plates under which the test section lies and some of the electric potential probes mounted on them.

The MHD flow at high Hartmann numbers and interaction parameters is determined once the pressure in the duct and the distribution of the electrical potential on the walls of the channel are known. For strong magnetic fields, the potential along field lines is a known function and therefore its surface distribution permits to estimate the potential in the entire flow domain. In planes perpendicular to the magnetic field, according to Ohm's law, if currents are negligible the potential gradient is proportional to the velocity and to the magnetic field. Therefore from measurements of potential gradient on the Hartmann walls it is possible to get information about velocity distribution.

A detailed description of the experimental facility and measurement techniques can be found in Barleon, Mack and Stieglitz (1996).

Calculations are performed using exactly the same geometry and the physical parameters employed in the experiments. It allows a direct comparison with the experimental data and serves as a further validation of the present implementation of MHD equations.

Fig.92 shows the potential distribution on the side wall of the duct for the flow at $Ha = 500$, $N = 50$ and $c = 0.03$.

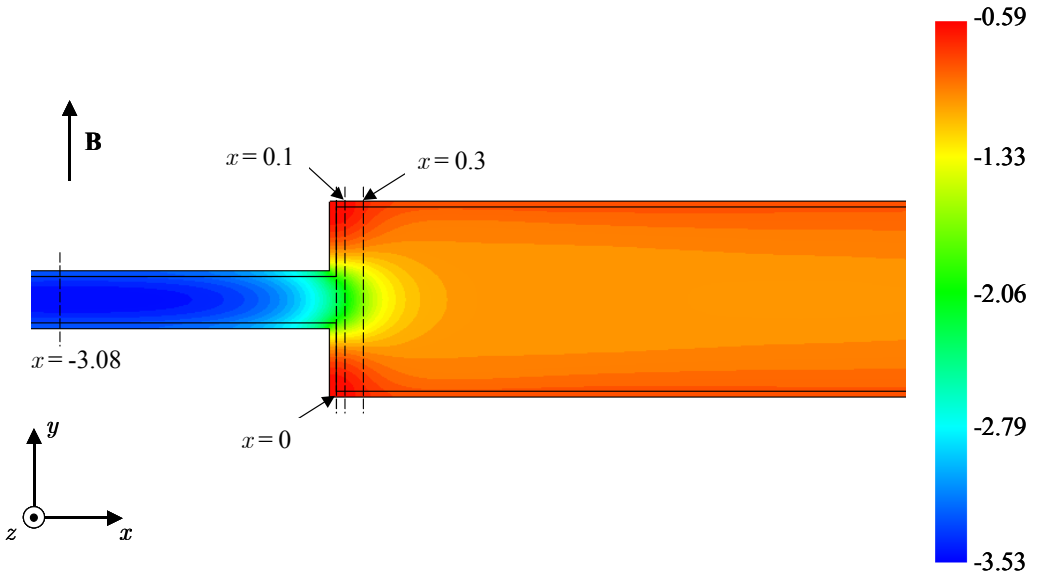

Figure 92: Contour plots of the calculated electric potential on the side wall of the duct for the flow at $Ha = 500$, $N = 50$ and $c = 0.03$. The numerical results are compared with the experiments along the dashed lines (Figs.93 and 94).

In Figs.93 and 94 the electric potential on the side wall is plotted along magnetic field lines at various axial locations. The numerical results are compared with the experiments for the flow at $Ha = 500$ and two different interaction parameters N.

The potential profile along field lines on the parallel walls can be regarded as an image of velocity distribution in the side layer. The difference between the potential at the wall and in the core gives information on the flux carried by the side layer.

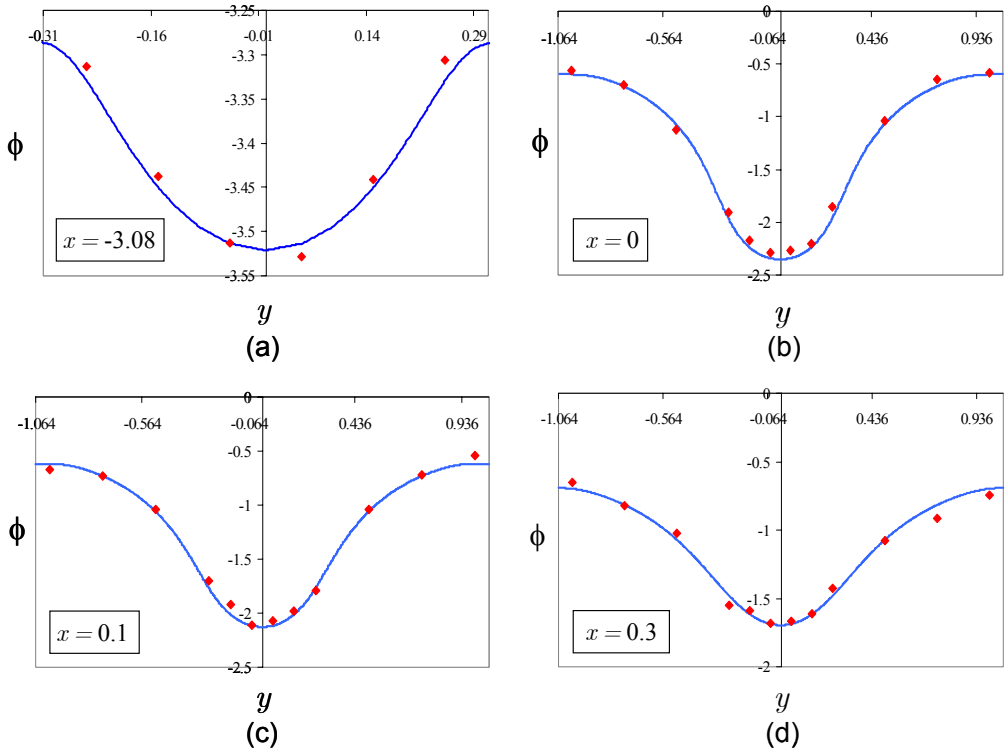

Figure 93: Electric potential on the side wall plotted along field lines at different axial locations. The symbols are the experimental data and the lines the numerical results for the flow at $Ha = 500$, $N = 50$ and $c = 0.03$.

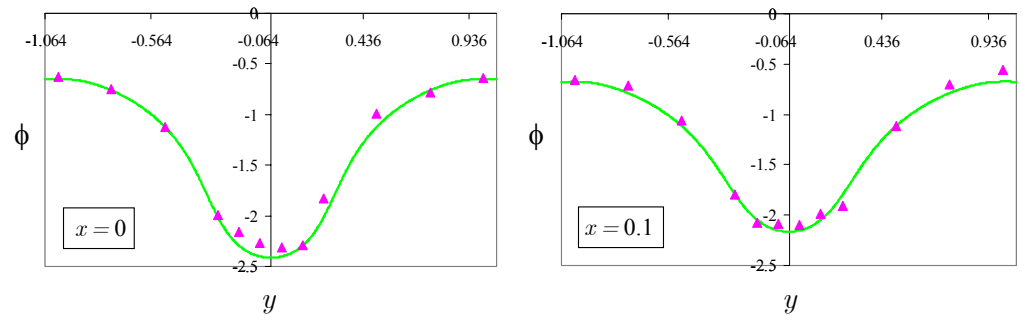

Figure 94: Electric potential distribution on the side wall of the duct along magnetic field lines at different axial positions. The symbols denote the experimental data and the lines the calculated values for the flow at $Ha = 500$, $N = 125$ and $c = 0.03$.

In Fig.95 the calculated pressure on the Hartmann walls is plotted along the x direction and compared with the experimental results for $Ha = 500$ and two different interaction parameters N. The two values in brackets show probably wrong measurements caused by the presence of bubbles in the pressure piping system.

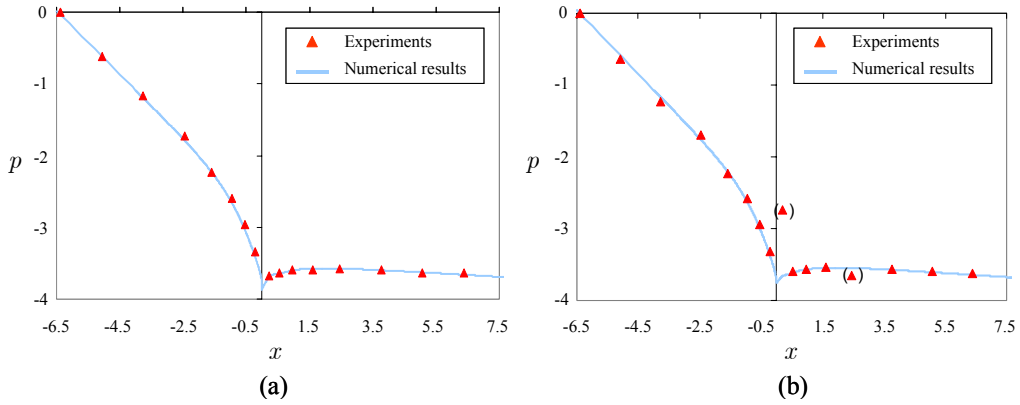

Figure 95: Pressure variation along the axial direction on Hartmann walls for $Ha = 500$ and two interaction parameters, $N = 50$ (a) and $N = 125$ (b).

An excellent agreement between calculations and experimental data is found for the flow at $Ha = 500$ both for the pressure distribution on the Hartmann walls along the streamwise direction and for the surface potential.

5 Final remarks

5.1 Summary

Magnetohydrodynamic phenomena caused by the interaction of electrically conducting fluids with a magnetic field have many engineering applications. The study of MHD effects can be carried out by means of analytical solutions, based on asymptotic techniques, valid for large Hartmann numbers and high interaction parameters as well as by direct numerical simulations. These latter are usually restricted to the study of MHD flows in simple geometries and at moderate applied magnetic field. Additional data can be obtained by performing experiments. Due to their cost and to technical limitations they cover generally only a limited range of parameters.

For these reasons a code has been developed to study MHD flows in arbitrary geometries exposed to a magnetic field of any orientation. The numerical approach is based on a pre-existing implementation of MHD equations in the commercial code CFX. By using this tool it was not possible to solve the MHD equations in solid walls. Therefore modifications and improvements have been done to include this option and a different approach has been considered for calculating the electric potential and the current density.

The code has been validated through the comparison of the calculated results with those available in the literature for the MHD flow in rectangular ducts exposed to a spatially varying magnetic field and with the analytical solution for the fully developed MHD flow in rectangular channels. A further validation of this numerical approach is given by the very good agreement between numerical and experimental data for wall potential and pressure distribution.

The code has been used to investigate the MHD flow in sudden expansions of rectangular ducts with walls of finite conductivity, focusing on the effects of the magnetic field and inertia forces on the size and the occurrence of separation regions. Starting from the analysis of an asymmetric hydrodynamic flow for a reference Reynolds number, the imposed magnetic field, namely the Hartmann number Ha, has been progressively increased.

When the magnetic field is weak ($Ha = 3$) the flow is still asymmetric but the length of the separation regions is strongly reduced. By raising the Hartmann number the flow becomes symmetric and a continuous reduction of the axial extent of the recirculation zones is observed. The dependence on the interaction parameter N of the reattachment length on the side wall of the channel shows that it scales as $N^{-0.3}$. This result can indicate that in the side layers a balance between inertia and electromagnetic forces is established. A different behavior is observed on the middle plane of the duct. Here the length of the recirculation varies as N^{-1}. The back flow region on this symmetry plane is present only in a limited range of the Hartmann number. For $Ha > 20$ the vortical structures start shrinking also in the transverse direction. When the magnetic field is strong enough ($Ha > 60$) the swirling motion is suppressed but in the side layers, close to the outer corners of the expansion, a reverse flow is still present. At this stage the flow redistributes rather rapidly in the large channel towards Hartmann walls and the strongest gradients of the flow variables are localized in a thin internal layer, which

spreads into the fluid from the corners of the expansion developing along magnetic field lines.

The analysis of the current distribution in the channel shows the presence of a number of characteristic current paths observed in all the range of parameters investigated. Upstream and downstream at some distance from the expansion the current closes its path in a cross-sectional plane showing the two dimensionality characteristic of fully developed conditions. Approaching the expansion the current loops start inclining in the direction of the motion due to the presence of 3D currents induced in the streamwise direction by an axial potential difference. When the magnetic field is sufficiently strong the 3D currents superimposed on the 2D current distribution lead to the formation of current loops that close exclusively in the core without involving the boundary layers and the walls. The center of these current paths is located in the large duct and moves closer to the expansion by increasing the Hartmann number. The distance between the center of the current core loop on the symmetry plane and the cross-section enlargement has been chosen as a measure for the thickness of the internal layer. This latter, for high interaction parameters, varies as $N^{-1/3}$ in accordance with the results of the asymptotic theory valid for $N << Ha^{3/2}$. In addition, there are current streamlines that surround all the region where the strongest 3D phenomena take place.

By raising the applied magnetic field the current in the core of the channel tends to flow in planes perpendicular to the field. This tendency towards two dimensionality can be explained by the formation at large Hartmann numbers of a inviscid core with uniform velocity where the main balance of forces is established between the pressure gradient and the Lorentz force. Here the pressure, which can be regarded as a sort of streamfunction for the current density, does not vary along field lines.

The study of the influence of the imposed magnetic field on the flow in sudden expansions has been performed by keeping the Reynolds number constant. As a consequence, an increase of the Hartmann number implies a rise of the interaction parameter that corresponds to a smaller ratio of inertia to electromagnetic forces.

It is therefore also interesting, in order to understand how inertia forces act on the structures of MHD flows at relatively high Hartmann number, to perform a parametric study by combining several interaction parameters with a constant Hartmann number ($Ha = 400$). An increase of inertia forces leads to a reduction of the velocity of the jets in the side layers and to a decrease of the transverse velocity. This implies that the flow redistributes towards the parallel walls, through the internal layer, over a longer axial distance from the expansion. As a result, the thickness of the internal layer raises. For $N > 800$ the thickness of the inertial part of the internal layer is proportional to $N^{-1/3}$. When inertia forces are sufficiently large vortical structures form behind the cross-section enlargement.

The additional pressure drop related to the 3D MHD phenomena has been calculated. For large interaction parameters the pressure loss seems to vary linearly with $N^{-1/3}$. By increasing the relative strength of inertia compared to electromagnetic forces a maximum value for the pressure drop has been found. A further decrease of the interaction parameter ($N < 30$) leads to a reduction of the additional pressure drop.

5.2 Conclusions

The results of the study of the effects of an increasing magnetic field on the flow at constant Reynolds number show that for moderate Hartmann number vortices form behind the expansion. Moreover, regions with very small velocities appear close to the external edge and the outer corners of the cross-section enlargement. The presence of almost stagnant zones might represent a problem for technical applications since they can affect for example the heat transfer, leading to the appearance of hot spots.

However it is important to notice that, even if the velocities are very small, there is always a circulation of the fluid. This is important for instance in fusion reactor blankets where a continuous exchange of flow is required to avoid accumulation of tritium.

Another issue that has to be carefully considered is the effect of inertial forces on flow distribution. The results of the parametric study, performed for a constant Hartmann number and by reducing the relative importance of inertia forces, show that inertial effects are important even when the interaction parameter is high ($N = 3000$). This study extend the present knowledge ($N = \infty$), gained through asymptotic techniques, into the range of moderate and small interaction parameter.

The numerical approach described in this work can be considered as an effective tool for accurate calculations of 3D MHD flows in arbitrary geometries with walls of various electric conductivity, under the action of a magnetic field of any orientation.

However it is necessary to observe that there are limitations regarding the maximum Hartmann number that can be employed if a very accurate solution is expected. It can be explained considering the results for the fully developed flow at $Ha = 1000$. They show that, in order to calculate the maximum velocity of the jets in the side layers within an accuracy of 4% of the analytical solution, a very fine grid is required in these layers. This leads to a large increase of the total number of nodes needed to discretize the cross-section of the channel. Since these results are used as inlet boundary conditions for 3D calculations, the utilized number of nodes should not exceed a maximum value, which has to be compatible with the number of grid points employed for resolving the 3D computational domain. Therefore the maximum Hartmann number that can be used, while preserving the accuracy of the solution, is limited practically by computational resources, namely by limitations in the memory storage and CPU time. If a lower accuracy of the solution is acceptable and therefore a smaller number of nodes can be used to discretize the computational domain, the MHD flow at larger Hartmann number ($Ha > 1000$) could be simulated approximately.

5.3 Recommendations for further studies

In order to study the MHD flow in the range of Hartmann numbers relevant for application in fusion technology ($Ha \sim 10^4$) a further modelling and development of the code is required. An idea is to implement analytic wall functions, which are of special concern for the current density, avoiding in this way to resolve the Hartmann layers. The effects of these thin viscous layers could be included by defining appropriate boundary conditions.

This code has been applied also to the study of electrical flow coupling across common

dividing walls of adjacent ducts for fully developed MHD flow. The results show that even in the 2D case peculiar velocity profiles are present. Therefore the problem of electrical coupling in three dimensional geometries is also an interesting subject for future investigations. This is a problem that arises for example in the so called Helium Cooled Lithium Lead (HCLL) concept for the blanket in fusion reactors. Here the flows in channels are electrically coupled through the common walls represented by cooling and stiffening plates.

In order to improve further our knowledge about MHD flows in sudden expansions it could be interesting to perform also transient calculations in order to investigate the effect of instabilities that can occur at high Reynolds numbers in the side layers (Ting, Walker, Moon, Reed and Picologlou (1991), Burr, Barleon, Müller and Tsinober (2000)).

Another challenging task is represented by the analysis of MHD flow in channels exposed to a time-varying magnetic field.

References

Abbot, D. E. and Kline, S.: 1962, Experimental investigation of subsonic turbulent flow over single and double backward facing steps, *Journal of Basic Engineering* **84**, 317–325.

Aitov, T. N., Kalyutik, A. I. and Tananaev, A. V.: 1983, Numerical analysis of three-dimensional MHD flow in channel with abrupt change of cross section, *Magnetohydrodynamics* **19**(2), 223–229.

Aleksandrova, S., Molokov, S. and Bühler, L.: 2003, *Unpublished Report*, Forschungszentrum Karlsruhe.

Alleborn, N., Nandakumar, K., Raszillier, H. and Durst, F.: 1997, Further contribution on the two-dimensional flow in a sudden expansion, *Journal of Fluid Mechanics* **330**, 169–188.

Alty, C. J. N.: 1971, Magnetohydrodynamic duct flow in a uniform transverse magnetic field of arbitrary orientation, *Journal of Fluid Mechanics* **48**, 429–461.

Armaly, B. F., Durst, F., Pereira, J. C. and Schönung, B.: 1983, Experimental and theoretical investigation of backward-facing step flow, *Journal of Fluid Mechanics* **127**, 473–496.

Baloch, A., Townsend, P. and Webster, M. F.: 1995, On two- and three-dimensional expansion flows, *Computers Fluids* **24**(8), 863–882.

Barleon, L., Mack, K.-J. and Stieglitz, R.: 1996, The MEKKA-facility - a flexible tool to investigate MHD-flow phenomena, *Report FZKA 5821*, Forschungszentrum Karlsruhe.

Battaglia, F., Tavener, S. J., Kulkarni, A. K. and Merkle, C. L.: 1997, Bifurcation of low Reynolds number flows in symmetric channels, *AIAA Journal* **35**(1), 99–105.

Branover, G. G., Vasil'ev, A. S. and Gel'fgat, Y. M.: 1967, Effect of a transverse magnetic field on the flow in a duct at a sudden cross section enlargement, *Magnitnaya Gidrodynamica* **3**(3), 61–65.

Bühler, L.: 1995, Magnetohydrodynamic flows in arbitrary geometries in strong, nonuniform magnetic fields, *Fusion Technology* **27**, 3–24.

Bühler, L.: 2003, Magnetohydrodynamic flows in sudden expansions in strong magnetic fields, *4th International Conference on Electromagnetic Processing of Materials*, Paris: Forum Editions, Lyon, 14-17 October, 34–44. Proceedings.

Burr, U., Barleon, L., Müller, U. and Tsinober, A. B.: 2000, Turbulent transport of momentum and heat in magnetohydrodynamic rectangular duct flow with strong side wall jets, *Journal of Fluid Mechanics* **406**, 247–279.

Chang, C. and Lundgren, S.: 1961, Duct flow in magnetohydrodynamics, *Zeitschrift für angewandte Mathematik und Physik* **XII**, 100–114.

Cherdron, W., Durst, F. and Whitelaw, J. H.: 1978, Asymmetric flows and instabilities in symmetric ducts with sudden expansions, *Journal of Fluid Mechanics* **84**(1), 13–31.

Chiang, T. P. and Sheu, T. W.: 1998, A numerical revisit of backward-facing step flow problem, *Physics of Fluids* **11**(4), 862–874.

Chiang, T. P., Sheu, T. W. and Wang, S. K.: 2000, Side wall effects on the structure of laminar flow over a plane-symmetric sudden expansion, *Computers Fluids* **29**(5), 467–492.

Davidson, P. A.: 1999, Magnetohydrodynamics in materilals processing, *Annual Reviews of Fluid Mechanics* **31**, 273–300.

Délery, J. M.: 2001, Robert legendre and henri werlé: Toward the elucidation of three-dimensional separation, *Annual Review of Fluid Mechanics* **33**, 129–154.

Drikakis, D.: 1997, Bifurcation phenomena in incompressible sudden expansion flows, *Physics of Fluids* **9**(1), 76–87.

Durst, F., Mellin, A. and H.Whitelaw, J.: 1974, Low Reynolds number flow over a plane symmetric sudden expansion, *Journal of Fluid Mechanics* **64**(1), 111–128.

Durst, F., Pereira, J. C. and Tropea, C.: 1993, The plane symmetric-sudden expansion flow at low Reynolds number, *Journal of Fluid Mechanics* **248**, 567–581.

Evtushenko, I. A., Sidorenkov, S. I. and Shishko, A. Y.: 1992, Experimental studies of magnetohydrodynamic processes in slotted channels within a strong magnetic field, *Magnetohydrodynamics* (2), 182–192.

Fearn, R. M., Mullin, T. and Cliffe, K. A.: 1990, Non linear flow phenomena in a symmetric sudden expansion, *Journal of Fluid Mechanics* **211**, 595–608.

Gel'fgat, Y. M. and Kit, L. G.: 1971, Investigation of the conditions of occurrence of M-shaped velocity profiles at sudden expansion or contraction of a magnetohydrodynamic flow, *Magnetohydrodynamics* **7**(1), 21–25.

Hartmann, J.: 1937, Hg-Dynamics I Theory of the laminar flow of an electrically conductive liquid in a homogeneous magnetic field, *Det Kgl. Danske Videnskabernes Selskab. Mathematisk-fysiske Meddelelser.* **XV**(6), 1–27.

Hawa, T. and Rusak, Z.: 2001, The dynamics of a laminar flow in a symmetric channel with a sudden expansion, *Journal of Fluid Mechanics* **436**, 283–320.

Horanyi, S., Bühler, L. and Arbogast, E.: 2005, Experiments on magnetohydrodynamic flows in a sudden expansion of rectangular ducts at high hartmann numbers, *Joint 15th Riga and 6th PAMIR International Conference on Fundamental and Applied MHD*, Vol. 1, 243–246. Riga Jurmala, 27 June - 1 July. Proceedings.

Hunt, J. C. R.: 1965, Magnetohydrodynamic flow in rectangular ducts, *Journal of Fluid Mechanics* **21**, 577–590.

Hunt, J. C. R. and Holroyd, R. J.: 1977, Applications of laboratory and theoretical MHD duct flow studies in fusion reactor technology, *Technical Report CLM-R169*, Culham Laboratory.

Hunt, J. C. R. and Leibovich, S.: 1967, Magnetohydrodynamic flow in channels of variable cross-section with strong transverse magnetic fields, *Journal of Fluid Mechanics* **28**(Part 2), 241–260.

Hunt, J. C. R. and Stewartson, K.: 1965, Magnetohydrodynamic flow in rectangular ducts, *Journal of Fluid Mechanics* **23**, 563–581.

Kulikovskii, A. G.: 1968, Slow steady flows of a conducting fluid at large Hartmann numbers, *Fluid Dynamics* **3**(1), 1–5.

Kumamaru, H., Kodama, S., Hirano, H. and Itoh, K.: 2004, Three-dimensional numerical calculations on liquid-metal magnetohydrodynamic flow in magnetic-field inlet-region, *Journal of Nuclear Science and Technology* **41**(5), 624–631.

Legendre, R.: 1956, Séparation de l'écoulement laminaire tridimensionnel, *Rech. Aéro.* **54**, 3–8.

Lighthill, M.: 1963, Attachment and separation in three- dimensional flows, *in* L. Rosenhead (ed.), *Laminar Boundary Layers*, Oxford University Press, chapter II, 2.6, pp. 72–82.

Ludford, G. S. S.: 1960, The effect of a very strong magnetic cross-field on steady motion through a slightly conducting fluid, *Journal of Fluid Mechanics* **10**, 141–155.

Molokov, S.: 1994, Liquid metal flows in manifolds and expansions of insulating rectangular ducts in the plane perpendicular to a strong magnetic field, *Report KfK 5272*, Kernforschungszentrum Karlsruhe.

Molokov, S. and Bühler, L.: 1994, Liquid metal flow in a U-bend in a strong uniform magnetic field, *Journal of Fluid Mechanics* **267**, 325–352.

Moon, T. J., Hua, T. Q. and Walker, J. S.: 1991, Liquid-metal flow in a backward elbow in the plane of a strong magnetic field, *Journal of Fluid Mechanics* **227**, 273–292.

Morley, N. B., Malang, S. and Kirillov, I.: 2005, Thermofluid magnetohydrodynamic issues for liquid breeders, *Fusion Science and Technology* **47**, 488–501.

Müller, U. and Bühler, L.: 2001, *Magnetofluiddynamics in Channels and Containers*, Springer, Wien, New York. ISBN 3-540-41253-0.

Myasnikov, M. V. and Kalyutik, A. I.: 1997, Numerical simulation of incompressible mhd flows in channels with a sudden expansion, *Magnetohydrodynamics* **33**(4), 342–349.

Nie, J. H. and Armaly, B. F.: 2003, Reattachment of three-dimensional flow adjacent to backward-facing step, *Journal of Heat Transfer* **125**(3), 422–428.

Patankar, S.: 1980, *Numerical Heat Transfer and Fluid Flow*, Hemisphere Publ.Co., Washington.

Picologlou, B. F., Reed, C. B., Hua, T. Q., Barleon, L., Kreuzinger, H. and Walker, J. S.: 1989, MHD flow tailoring in first wall coolant channels of self-cooled blankets, *Fusion Engineering and Design* **8**, 297–303.

Restivo, A. and Whitelaw, J. H.: 1978, Turbulence characteristics of the flow downstream of a symmetric plane sudden expansion, *Journal of Fluids Engineering, Trans. ASME* **100**, 308–310.

Revuelta, A.: 2005, On two-dimensional flow in a sudden expansion with large expansion ratios, *Physics of Fluids* **17**.

Rusak, Z. and Hawa, T.: 1999, A weakly nonlinear analysis of the dynamics of a viscous flow in a symmetric channel with a sudden expansion, *Physics of Fluids* **11**(12), 3629–3636.

Schreck, E. and Schäfer, M.: 2000, Numerical study of bifurcation in three-dimensional sudden channel expansions, *Computers and Fluids* **29**(5), 583–593.

Shercliff, J. A.: 1953, Steady motion of conducting fluids in pipes under transverse magnetic fields, *Proc.Camb.Phil.Soc.* **49**, 136–144.

Shercliff, J. A.: 1965, *A Textbook of Magnetohydrodynamics*, Pergamon Press, Oxford.

Shih, C. and Ho, C. M.: 1994, Three-dimensional recirculation flow in a backward facing step, *Journal of Fluids Engineering* **116**, 228–232.

Sobey, I. J. and Drazin, P. G.: 1986, Bifurcations of two-dimensional channel flows, *Journal of Fluid Mechanics* **171**, 263–287.

Spille-Kohoff, A.: 2004, Simulation of gas metal arc welding with CFX-5, *ANSYS CFX ICEM CFD Conference*, Dresden, 10-12 November.

Sterl, A.: 1990, Numerical simulation of liquid-metal MHD flows in rectangular ducts, *Journal of Fluid Mechanics* **216**, 161–191.

Stieglitz, R., Barleon, L., Bühler, L. and Molokov, S.: 1996, Magnetohydrodynamic flow through a right-angle bend in a strong magnetic field, *Journal of Fluid Mechanics* **326**, 91–123.

Talmage, G. and Walker, J. S.: 1987, Three-dimensional laminar MHD flow in ducts with thin metal walls and strong magnetic fields, *Proceedings of the 5th Beer Sheva International Seminar on MHD Flows and Turbulence*, Israel, 2-6 March, American Institute of Aeronautics and Astronautics.

Temperley, D. J. and Todd, L.: 1971, The effect of wall conductivity in magnetohydrodynamic duct flow at high Hartmann number, *Proc. Camb. Phil. Soc.* **69**, 337–351.

Ting, A. L., Walker, J. S., Moon, T. J., Reed, C. B. and Picologlou, B. F.: 1991, Linear stability analysis for high-velocity boundary layers in liquid-metal magnetohydrodynamic flows, *Int. J. Engng. Sci.* **29**(8), 939–948.

Tobak, M. and Peake, D. J.: 1982, Topology of three-dimensional separated flows, *Annual Review of Fluid Mechanics* **14**, 61–85.

Tylli, N., Kaiktsis, L. and Ineichen, B.: 2002, Sidewall effects in flow over a backward-facing step: Experiments and numerical simulations, *Physics of Fluids* **14**(11), 3835–3845.

Uflyand, Y. S.: 1961, Flow stability of a conducting fluid in a rectangular channel in a transverse magnetic field, *Soviet Physics Technical Physics* **5**, 1191–1193.

Walker, J. S.: 1981, Magnetohydrodynamic flows in rectangular ducts with thin conducting walls, *Journal de Mécanique* **20**(1), 79–112.

Walker, J. S.: 1986a, Liquid-metal flow in a thin conducting pipe near the end of a region of uniform magnetic field, *Journal of Fluid Mechanics* **167**, 199–217.

Walker, J. S.: 1986b, Liquid metal flow through a thin walled elbow in a plane perpendicular to a uniform magnetic field, *Int. J. Engng. Sci.* **24**(11), 1741–1754.

Walker, J. S., Ludford, G. S. S. and Hunt, J. C. R.: 1972, Three-dimensional MHD duct flows with strong transverse magnetic fields. part 3. variable-area rectangular ducts with insulating walls, *Journal of Fluid Mechanics* **56**, 121–141.

Williams, P. T. and Baker, A. J.: 1997, Numerical simulations of laminar flow over a 3D backward-facing step, *International Journal for Numerical Methods in Fluids* **24**, 1159–1183.

Appendix

Dimensionless equations

The momentum equation

$$\rho\left[\frac{\partial}{\partial t}\mathbf{v}+(\mathbf{v}\cdot\nabla)\,\mathbf{v}\right]=-\nabla p+\rho\nu\nabla^2\mathbf{v}+\mathbf{j}\times\mathbf{B},$$

can be written in dimensionless form by choosing different scales for the pressure. Two options are considered in the following.

The scales for the velocity, the length, the time and the magnetic field are the same in both the approaches. By indicating the dimensional variables by an asterisk and the scales by the subscript 0, the dimensionless variables can be expressed as follows:

$$\mathbf{v}=\frac{\mathbf{v}^*}{v_0}$$

$$\nabla=\nabla^*\,L$$

$$t=\frac{t^*}{L/v_0}$$

$$\mathbf{B}=\frac{\mathbf{B}^*}{B_0}$$

The two scales chosen for the pressure are indicated as hydrodynamic and MHD scale. The non dimensional pressure in the hydrodynamic scale is given by:

$$p_{hyd}=\frac{p^*}{p_{0hyd}}=\frac{p^*}{\rho v_0^2}$$

The momentum equation then becomes

$$\frac{\partial}{\partial t}\mathbf{v}+(\mathbf{v}\cdot\nabla)\,\mathbf{v}=-\nabla p_{hyd}+\frac{1}{Re}\nabla^2\mathbf{v}+N\,(\mathbf{j}\times\mathbf{B})\,, \tag{13}$$

where Re is the Reynolds number and N is the interaction parameter.

By using the magnetohydrodynamic scale the dimensionless pressure reads as

$$p_{mhd}=\frac{p^*}{p_{0mhd}}=\frac{p^*}{\sigma L v_0 B_0^2}$$

and the equation for the conservation of momentum in non dimensional form can be written as

$$\frac{1}{N}\left[\frac{\partial}{\partial t}\mathbf{v}+(\mathbf{v}\cdot\nabla)\,\mathbf{v}\right]=-\nabla p_{mhd}+\frac{1}{Ha^2}\nabla^2\mathbf{v}+\mathbf{j}\times\mathbf{B}, \tag{14}$$

where Ha is the Hartmann number. This type of equation highlights the fact that for strong magnetic fields, i.e. $Ha >> 1$, $N >> 1$, the MHD flow is governed by a balance between pressure and Lorentz forces.

The relation between the dimensionless pressures in hydrodynamic and MHD scale is the following

$$p_{hyd} = p_{mhd} N \tag{15}$$

In order to simplify the notation, avoiding the use of subscripts, in the thesis the pressure in the hydrodynamic scale has been indicated by p and the pressure in the MHD scale by P. Therefore the relation (15) becomes

$$p = P\ N. \tag{16}$$

The momentum equation in hydrodynamic scale (13) can be used to describe both the hydrodynamic and the magnetohydrodynamic flow. Equation (14) instead is not valid for $Ha = 0$, namely in the absence of an applied magnetic field.